

NUMERICAL SIMULATIONS OF PERMEABLE-WALL TURBULENCE WITH
APPLICATIONS IN HYPORHEIC EXCHANGE

By

Guangchen Shen

A DISSERTATION

Submitted to
Michigan State University
in partial fulfillment of the requirements
for the degree of

Mechanical Engineering – Doctor of Philosophy

2022

ABSTRACT

NUMERICAL SIMULATIONS OF PERMEABLE-WALL TURBULENCE WITH APPLICATIONS IN HYPORHEIC EXCHANGE

By

Guangchen Shen

In aquatic environments such as rivers, the exchange of solutes across the interface between the sediment and the overlying water plays a significant role in controlling biogeochemical processes, which are important for an array of topics from nutrient transport and cycling to release of greenhouse gases such as nitrous oxide. Most previous studies on characterizing this exchange are focused on flows with sediment bedforms much larger than individual sediment grains. The physics at the pore or grain scale were typically not resolved. The effects of grain roughness on the sediment bed surface on the transport across the sediment-water interface (SWI), isolated from those of bed permeability and bedforms, are not well understood. In this work, direct numerical simulations (DNS) of the connected system of turbulent open-channel flow and pore-resolved sediment flow are carried out, with different arrangements of grains at the sediment surface.

First, the statistics and structure of the mean flow and turbulence are characterized in flows with a friction Reynolds number of 395 and a permeability Reynolds number of 2.6 over sediments with either regular or random grain packing on a macroscopically flat bed. It is shown that, even in the absence of any bedform, the subtle details of grain roughness alone can significantly affect the dynamics of turbulence and the time-mean flow. Such effects translate to large differences in penetration depths, apparent permeabilities, vertical mass fluxes and subsurface flow paths. The less organized distribution of mean recirculation regions near the interface with a random packing leads to a more isotropic form-induced stress tensor, which plays a significant role in increasing mixing and wall-normal exchange of mass and momentum.

Next, the mass exchange is characterized in detail for macroscopically flat river beds, focusing on the transit time—the time spent by a fluid particle in the sediment—which determines the role of hyporheic zones in transforming the chemical signature of stream water. Results show that bed

roughness leads to interfacial pressure variations, which induces deep subsurface flow paths that yield a transit time distribution with a heavy tail. Furthermore, the addition of molecular diffusion is accounted for and is shown to increase transit times regardless of roughness texture. The results demonstrate that particle roughness on a macroscopically flat sediment bed can induce significant hyporheic exchange that is fundamentally similar to that induced by bedforms.

Lastly, to identify possible interaction between the effect of grain roughness and that of a bedform, DNSs of open channels with a friction Reynolds number of 1580 on a porous dune with two different roughnesses are conducted. Results show that the roughness modifies the wall friction, shear penetration depth and pressure distribution along the interface. Unlike the case on a macroscopically flat bed where the random roughness induces more intense roughness-scale pressure variation than the regular roughness, over a bedform the random roughness reduces the macroscopic pressure distribution at the interface instead due to its higher hydrodynamic drag. The weaker pressure variation in turn weakens the pumping and shortens transit times. The results highlight the nonlinear interaction between the effects of bed morphological features of different scales. Pore-resolved simulations such as the ones herein can be used in the future in direct characterization of pore-scale dynamics to provide insights for pore-unresolved modeling of biogeochemical processes.

Copyright by
GUANGCHEN SHEN
2022

ACKNOWLEDGEMENTS

I am fortunate to have had support and guidance from many people during the pursuit of my doctorate degree. First and foremost, I would like to thank my advisor, Professor Junlin Yuan, for her support, encouragement and guidance throughout my education at the Michigan State University. Thank you for always believing in me and teaching me how to be an excellent researcher. I am also grateful to Professor Mantha S. Phanikumar. Your expertise and knowledge in hypersonic exchange has helped me shape my current understanding in this field. Thanks also go to my dissertation committee. Professor Farhad Jaber, whose courses on Turbulent Flows made a significant impact on my study of turbulence. I would also like to thank my committee member Professor Ricardo Mejia-Alvarez for your valuable comments and suggestions on my thesis. Working with Professor Mejia-Alvarez as two semesters teaching assistant has been very memorable and enjoyable.

I would like to thank my colleagues at our TSM lab Saurabh Pargal, Sai Chaitanya and Mostafa Aghaei Jouybari for their suggestions and help throughout the years. I will never forget the days we spent in Atlanta, Maryland, Seattle and Phoenix. Special thanks to my friends who help and share happiness with me throughout these years: Amirreza Gandomkar, Sheng Chen, Yuan Yao, and Joy Mojumder.

Finally, I would like to thank my parents for their endless love and support and also my sister who always believes in her brother.

TABLE OF CONTENTS

LIST OF TABLES	viii
LIST OF FIGURES	ix
KEY TO SYMBOLS AND ABBREVIATIONS	xiv
CHAPTER 1 INTRODUCTION	1
1.1 Hyporheic exchange	1
1.2 Literature Review	2
1.2.1 Turbulence across the sediment-water interface	2
1.2.2 Conservative-solute transport in the sediment	5
1.3 Research objectives and outline	9
CHAPTER 2 DIRECT NUMERICAL SIMULATIONS OF TURBULENCE AND HY- PORHEIC MIXING NEAR SEDIMENT-WATER INTERFACES	11
2.1 Introduction	11
2.2 Methodology	12
2.2.1 Governing equations	12
2.2.2 Parameters	13
2.2.3 Synthesis of porous beds	16
2.2.4 Geometrical comparison of the two interface types	17
2.3 Results	20
2.3.1 Validation of sediment synthesis	20
2.3.2 Effects of interface irregularity on flow statistics	23
2.3.2.1 DA velocity and friction	23
2.3.2.2 Turbulent fluctuations	25
2.3.2.3 Form-induced fluctuations	28
2.3.2.4 Reynolds-stress budgets	30
2.3.3 Implications for the mechanism of flat-bed hyporheic exchange	34
2.3.3.1 Variation of apparent permeability	34
2.3.3.2 Momentum transport mechanisms and dependence on rough- ness geometry	36
2.3.3.3 Mechanisms producing vertical mass flux	39
2.4 Conclusions and discussions	42
CHAPTER 3 QUANTIFYING THE EFFECTS OF BED ROUGHNESS ON TRANSIT TIME DISTRIBUTIONS VIA DIRECT NUMERICAL SIMULATIONS OF TURBULENT HYPORHEIC EXCHANGE	45
3.1 Introduction	45
3.2 Methodology	46
3.2.1 Case configuration and parameters	46
3.2.2 Transit time calculation based on particle tracking	49

3.3	Results	53
3.3.1	Effect of bed roughness geometry on transit times	53
3.3.2	Interfacial \bar{v} distribution	59
3.3.3	Effect of molecular diffusion on TTD	62
3.4	Conclusions	64
CHAPTER 4	PORE-RESOLVED DIRECT NUMERICAL SIMULATIONS OF HY- PORHEIC EXCHANGE INDUCED BY BEDFORMS AND BED ROUGH- NESS	67
4.1	Introduction	67
4.2	Methodology	68
4.2.1	Configurations and parameters	68
4.2.2	Transit time calculation based on particle tracking	71
4.3	Results	72
4.3.1	Effects of roughness geometry on velocity	73
4.3.2	Effects of roughness geometry on pressure field	74
4.3.3	Effects of roughness geometry on transit times	77
4.4	Conclusions	80
CHAPTER 5	CONCLUSIONS	81
5.1	Summary	81
5.2	Future work	82
APPENDICES	83
APPENDIX A	DETAILS OF POROUS-BED SYNTHESSES	84
APPENDIX B	SUPPORT INFORMATION FOR CHAPTER 3	86
BIBLIOGRAPHY	91

LIST OF TABLES

Table 2.1: Summary of simulations. θ_{avg} is the average porosity in the bulk of the sediment; D is the sphere diameter; H_s is the sediment depth; L_{x_i} is the domain size in x_i	13
Table 2.2: Flow parameters for Cases 2 and 3. δ_b and δ_p are Brinkman-layer thickness and Reynolds-stress penetration depth, both measured from $y = -d$; δ_b^* and δ_p^* are the same lengths measured from crest; K^* is apparent permeability.	22
Table 3.1: Summary of simulation parameters. D is the grain diameter; L_{x_i} is the simulation domain size in x_i . Δx^+ , Δy^+ , and Δz^+ are DNS grid sizes in x , y and z , respectively, normalized using the viscous length scale ν/u_τ	47
Table 3.2: Various characteristics of transit times calculated based on mean advection only and both mean advection and molecular diffusion, at two elevations of particle entry (y_1) and exit (y_2). Transit times are normalized by δ/u_τ . Note. ‘A’ denotes calculation based on time-mean advection alone; ‘MD’ denotes calculation accounting for both time-mean advection and molecular diffusion (discussed in Section 3.3.3).	54
Table 4.1: Summary of parameters. D is the grain diameter; L_{x_i} is the simulation domain size in x_i ; $Re_K = 2.5$, $Re_\tau = 1580$, $D^+ = 79$. Δx^+ , Δy^+ , and Δz^+ are DNS grid sizes in x , y and z , respectively, normalized using the viscous length scale ν/u_τ	69
Table 4.2: Various characteristics of transit times calculated based on mean advection only. Transit times are normalized by δ/u_τ . Note. τ_{50} and τ_{95} represent 50th (median) and 95th percentiles of the TTD distributions.	77

LIST OF FIGURES

Figure 1.1:	Perspectives in (a) reach scale (Boano et al., 2014), (b) local scale (Stonedahl et al., 2010) and (c) pore scale (Voermans et al., 2018) of surface-subsurface water interactions and hyporheic exchange.	1
Figure 2.1:	(a) Simulation domain and (b) positions of sediment crest, k_c , and zero-plane displacement, d , defined in Section 2.3.2.1.	14
Figure 2.2:	Synthesized sediment beds colored by y/δ with (a) the regular and (b) the random interfaces.	16
Figure 2.3:	Wall-normal profiles of plane-averaged porosity profile for regular (---) and random (—) interfaces.	17
Figure 2.4:	Bed surface height fluctuations for the (a) regular and (b) random interfaces. (c) Autocorrelation of height fluctuations and Taylor micro scales.	18
Figure 2.5:	Histogram of bed height fluctuations for the (a) regular and (b) random interfaces.	19
Figure 2.6:	Comparison of (a) mean velocity and (b-d) streamwise, wall-normal and shear components of the Reynolds stress tensor. \circ Experiment, — DNS.	20
Figure 2.7:	Comparison of (a) streamwise, (b) wall-normal and (c) shear component of the form-induced stress tensor. \circ Experiment, — DNS. Black lines represent the values spatially averaged over the entire horizontal plane; grey lines emulate the sampling used in the experiment.	21
Figure 2.8:	(a) Diagnostic function for fitting the logarithmic profile and (b) DA velocity profiles for regular (---) and random (—) interfaces; --- (red) fitted logarithmic profiles.	22
Figure 2.9:	DA velocity along y in linear scaling for regular (---) and random (—) interfaces. Inset magnifies the distribution at $y \approx -d$	23
Figure 2.10:	Components of (a) the Reynolds-stress tensor and (b) the anisotropy tensor for regular (---) and random (—) interfaces.	25
Figure 2.11:	Contours of instantaneous u'^+ in the (x, z) plane at the respective $\overline{\langle u'^2 \rangle}$ -peak elevations for the (a) regular and (b) random interfaces.	26

Figure 2.12: Integral length scales of u' motions along the streamwise directions for regular (---) and random (—) interfaces.	26
Figure 2.13: Components of the form-induced stress tensor: (a) streamwise, (b) wall-normal and (c) spanwise components, for regular (---) and random (—) interfaces.	28
Figure 2.14: (a) Time-averaged streamlines for the regular interface. (b) Streamlines on Slice A ($x-y$ plane across the crests of the grains). (c) Streamlines distribution on Slice B ($x-y$ plane across the valley between two rows of grains). Dash lines indicate $y = -d$	29
Figure 2.15: (a) Time-averaged streamlines for the random interface. (b) and (c) show streamlines on two $x-y$ planes, Slice C and Slice D. Dash lines indicate $y = -d$. 29	
Figure 2.16: Shear stresses for cases with (a) regular and (b) random interfaces: --- Reynolds shear stress, --- viscous shear stress and — (red) form-induced shear stress.	30
Figure 2.17: Terms in the TKE budget equation. (a) Production and viscous dissipation for regular (symbols and thin lines) and random-interface (thick lines) cases; P_s (—, Δ), $P_m + P_w$ (—, \circ , red) and ϵ (---, \square). Transport terms for (b) regular and (c) random interfaces; T_w (—, red), T_t (---), T_v (—) and T_p (---). All terms are normalized by u_τ^3/δ	31
Figure 2.18: (a) Form-induced production and (b) pressure-strain-rate term in regular (---) and random interface (—) cases for the budgets of $\langle \overline{u'^2} \rangle_s$ (\circ , red), $\langle \overline{v'^2} \rangle_s$ (\square) and $\langle \overline{w'^2} \rangle_s$ (Δ , blue); normalization is done with u_τ and δ	32
Figure 2.19: Time-averaged spanwise vorticity $\overline{\omega}_z$ normalized by u_τ/δ at (a) Slice B of the regular interface and (b) Slice D of the random interface.	33
Figure 2.20: Horizontal variation of the apparent permeability K^* in the Brinkman layer in the random-interface case.	34
Figure 2.21: Terms in the DA u -momentum equation (equation (2.16)), normalized by u_τ^2/δ for (a) regular and (b) random interfaces: Reynolds-stress term(—, red), viscous stress term (---, red), total drag (—), form-induced stress term (---) and pressure-gradient term(---).	36
Figure 2.22: Horizontal variation of local volume-averaged \mathcal{D} (a) and $ \mathcal{I} $ (b), both normalized by u_τ^2/δ . (c) sediment surface height fluctuations h' normalized by δ for the random-interface case. (d) Correlations of \mathcal{D}' (red) and $ \mathcal{I}' $ (black) with h'	37

Figure 2.23: (a) Wall-normal flux at $y = -d$ normalized by $u_\tau \delta^2$ with different averaging window sizes Tu_τ/δ for regular (---) and random (—) interfaces. (b) Pressure-work term of $\langle \bar{v}^2 \rangle_s$ budget normalized by u_τ^3/δ for regular(---, ○) and random(—) interfaces.	39
Figure 2.24: Time-averaged pressure variation and 3D mean streamlines for (a) regular and (b) random interfaces. Blue arrows indicate examples of hyperheic flow paths.	40
Figure 3.1: Simulation domain and synthesized sediment beds colored by y in (a) the regular and (b) the random cases. (c) One-dimensional power spectral densities E_k of the interface height fluctuations for Case 1 (regular case, —) and Case 2 (random case, —, red). --- (red) Slope of power-law decay for Case 2; k_{rms} is the root-mean-square (rms) of interface height fluctuations.	46
Figure 3.2: (a) Sketch of typical tracked flow paths for the random interface (Case 2). The cumulative backward transit time distribution (b) and its pdf (c) are shown for two sets of entry and exit locations: $y_1 = y_2 = 0$ (—) and $y_1 = y_2 = -3D$ (---) for the regular interface (black lines) and the random interface (red lines). (d) Modified pdf showing the probability density in evenly spaced logarithmic increments. In (b), the horizontal dashed lines (---, blue) mark the 50th (median) and 95th percentiles. In (c), the dashed blue lines (---, blue) show the fitted power law with slopes indicated.	52
Figure 3.3: Time-mean subsurface flow paths corresponding to the median (50th-percentile) transit time (a,b,e,f) and the 95th-percentile transit time (c,d,g,h) for entry/exit elevations at $y_1 = y_2 = 0$ (a,b,c,d) and $y_1 = y_2 = -3D$ (e,f,g,h), for the regular (a,c,e,g) and random (b,d,f,h) interfaces.	55
Figure 3.4: Wall-normal variation of \bar{v} magnitude conditionally averaged along downward (red) or upward (black) flow paths tracked at $y_1 = y_2 = 0$, for regular (---) and random (—) cases.	57
Figure 3.5: Median transit time normalized by δ/u_τ with independent variations of y_1 (entry) and y_2 (exit) elevations, for regular (a) and random (b) cases. Similar variations of τ_{95} are shown in the Appendix B Figure B.5.	58
Figure 3.6: Sketch showing how local high-pressure (stagnation point) and low-pressure (recirculation) regions lead to entry and exit of fluid parcels (red spheres and red lines), specifically, in Case 2. --- Roughness geometry. $\bar{P}(x, y, z)$ and $\bar{v}(x, y, z)$ are the time-averaged values of pressure and wall-normal velocity; $\bar{P}(x, y, z) = \bar{P}(x, y, z) - \langle \bar{P} \rangle(y)$ is the form-induced pressure, i.e., deviations from the plane-averaged value.	59

Figure 3.7:	Bed-parallel contours for the random interface (Case 2) at $y = 0$: (a) bed-normal mean velocity, (b) form-induced pressure, (c) bed-normal gradient of mean pressure, and (d) transit time of flow paths entering at each location. Only 1/4 of the domain is shown. All quantities in (a-d) are normalized by δ and u_τ . Joint probability density functions of $\partial\bar{P}/\partial y$ and \bar{v} in the interface region, for Case 1 (e) and Case 2 (f).	60
Figure 3.8:	Cumulative backward transit time distribution (a) and its pdf (b) based on mean advection only (—) and based on both mean advection and molecular diffusion (---), for Case 1 (black) and Case 2 (red) at $y_1 = y_2 = 0$. In (b), --- (blue) shows the fitted power law with slope indicated.	63
Figure 4.1:	Simulation domain and synthesized bedforms with (a) regular and (b) random roughnesses, colored by y	68
Figure 4.2:	Roughness surfaces colored by y (a,b) and local height fluctuations measured from the bedform surface (c,d) in Cases 1 (a,c) and Case 2 (b,d). (e) One-dimensional power spectral densities E_k of the local height fluctuations for Case 1 (regular roughness, —) and Case 2 (random roughness, —, red). k_{rms} is the root-mean-square (rms) of interface height fluctuations.	70
Figure 4.3:	Conceptual sketch to show the enter and exit locations of tracked particles.	71
Figure 4.4:	(a) Time- and spanwise-averaged streamwise velocity $\langle\bar{u}\rangle_z^+$ for cases with regular (—) and random (---, red) roughnesses. $\langle\bar{u}\rangle_z^+$ contours for (b) regular and (c) random roughness.	72
Figure 4.5:	Profiles of (a) viscous shear stresses $-\partial\langle\bar{u}\rangle_z^+/\partial y^+$ and (b) Reynolds shear stresses $-\langle\bar{u}'v'\rangle_z^+$ for cases with regular (—) and random (---, red) roughnesses.	74
Figure 4.6:	Time- and spanwise-averaged pressure field for cases with (a) regular and (b) random roughnesses. Pressure distributions along the SWI normalized using bulk velocity (c) or friction velocity (d) for both cases.	75
Figure 4.7:	Distribution of the Clauser parameter β in the two cases. The black dash line shows the bedform interface geometry.	76
Figure 4.8:	Cumulative backward transit time distributions (a) and their pdf distributions (b) for regular (—) and random (---, red) cases. In (a), the horizontal dashed lines (---, blue) mark the 50th (median) and 95th percentiles. In (b), the dashed blue lines (---, blue) show the fitted power law with slopes indicated. Subsurface flow paths in the (c) regular and (d) random cases.	78

Figure 4.9: Histogram of the number of flow paths reaching a depth of a given y value for the two cases. Values are normalized such that the area integral is one. . . .	79
Figure A.1: Bed synthesis with random interface packing.	84
Figure A.2: Bed synthesis with regular interface packing.	84
Figure B.1: Residence time distributions (RTD) normalized by Q/S for $y_1 = y_2 = 0$ (—) and $-3D$ (---). For $\tau u_\tau/\delta > o(10^6)$ when $y_1 = y_2 = 0$ or $o(10^7)$ when $y_1 = y_2 = -3D$, the RTD rapidly decreases; this is not physical but an artifact associated with the finite domain size in x (limited to $2L_x$) imposed for particle tracking as the tracking procedure cannot be indefinitely long. . . .	86
Figure B.2: Validation of particle tracking against EB97, with various spatial resolution and a sediment domain of $y \in [-\lambda/2, 0]$ (a) or $y \in [-\lambda, 0]$ (b).	88
Figure B.3: Sketch to demonstrate that a particle entry elevation (y_1) lower than the exit elevation (y_2) tracks a larger fraction of subsurface flow paths than in the case with $y_1 > y_2$, considering the same $ y_1 - y_2 $. Here, (y'_1, y'_2) tracks 2 out of the 4 paths (50%) entering from y'_1 , while (y''_1, y'_2) tracks 2 out of the 2 paths (100%) entering from y''_1	89
Figure B.4: Streamwise dispersive velocity intensities in the sediment bed: comparison between results obtained from DNS data taken for simulation times of 10 (—, red) and 20 (---) large-eddy turn-over times, for the regular- (a) and random-interface (b) cases.	90
Figure B.5: Transit time of the 95th percentile (τ_{95}) normalized by δ/u_τ with independent variations of y_1 (entry) and y_2 (exit) elevations, for the regular- (a) and random-interface (b) cases.	90

KEY TO SYMBOLS AND ABBREVIATIONS

- A_f area occupied by fluid
- A_o total area of fluid and solid
- β Clauser paramete
- b_{ij} Reynolds stress anisotropy tensor
- B mean-velocity profile intercept in the logarithmic region
- C_f friction coefficient
- d zero-plane displacement
- D grain diameter
- D_m molecular diffusion coefficient
- D^+ particle Reynolds number
- Δt time differential
- $\Delta x, \Delta y, \Delta z$ grid spacing
- ΔU^+ roughness function
- δ boundary layer thickness
- δ_b Brinkman-layer thickness
- δ_p Reynolds-stress penetration depth
- δ^* displacement thickness
- δ_v viscous length scale
- δ_{ij} Kronecker Delta
- ϵ viscous dissipation
- E_k power spectral density
- F_i immersed-boundary-method body force in i direction
- F_D total drag
- h sediment height
- H_s sediment depth

λ Taylor micro-scale of local roughness-height fluctuations

k^+ roughness Reynolds number

k_c sediment crest elevation

κ von Kármán constant

K permeability

K^* aparent permeability

λ wavelength

L_x, L_y, L_z domain size

L_{ij} integral length scale

ν kinematic viscosity

n_i, n_j, n_k numbers of grid points in x , y , and z

R autocorrelation

p_Q transit time probability density function

P_Q transit time cumulative distribution function

p_S residence time probability density function

P or p modified pressure (pressure over density)

P_s shear production

P_w wake production

Π pressure work

ϕ instantaneous flow variable

Q vertical volumetric flux

ρ density

\mathcal{R} pressure-strain-rate term

Re Reynolds number

Re_τ friction Reynolds number

Re_K permeability Reynolds number

S instantaneous total water storage

σ_h root-mean-square of height fluctuation
 t time
 T total simulation time
 T_p pressure transport
 T_t turbulent transport
 T_v viscous transport
 τ transit time
 θ porosity
 θ_{avg} average porosity in the bulk of the sediment
 u_i instantaneous velocity components
 u_τ friction velocity
 U mean velocity
 U_δ free-surface (or channel-half-height) flow velocity
 U_p constant velocity in the sediment far below the SWI
 ω turbulent vorticity
 x_i spatial direction
APG adverse pressure gradient
CAD computer-aided design
DA double-averaging
DNS direct numerical simulation
FPG favourable pressure gradient
IBM immersed boundary method
K – H Kelvin-Helmholtz
LES large-eddy simulation
LETOT large-eddy turn-over time
MD molecular dynamics
MPI message passing interface

pdf probability distribution function

RANS Reynolds-averaged Navier-Stokes

RMS root-mean-square

RTD residence time distribution

SWI sediment-water interface

TKE turbulent kinetic energy

TTD transit time distribution

CHAPTER 1

INTRODUCTION

In this Chapter, first the hyporheic exchange and its importance are introduced. Then a detailed literature review is conducted and limitations of the current understanding of the exchange processes are discussed. The research objectives are proposed based on present limitations and the studies in this dissertation to address these goals are outlined.

1.1 Hyporheic exchange

Aquatic environments such as rivers form an important part of the water circulation on earth. A typical river flow can be considered as a turbulent water flow bounded by permeable sediment beds at the sides and the bottom, as shown in Fig. 1.1 (a). Vertical and lateral exchanges of water

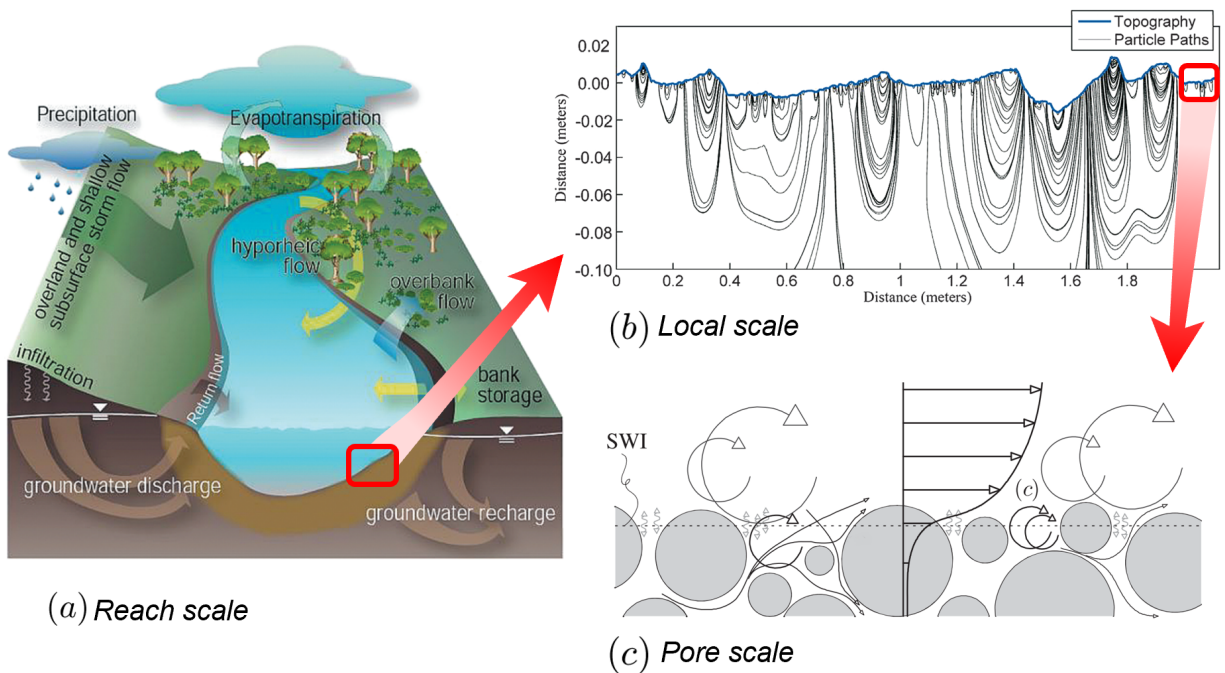


Figure 1.1: Perspectives in (a) reach scale (Boano et al., 2014), (b) local scale (Stonedahl et al., 2010) and (c) pore scale (Voermans et al., 2018) of surface-subsurface water interactions and hyporheic exchange.

and solutes with the more slowly moving flow in the sediments are important. Specifically, the sediments slow down the overall movement of solutes and increase opportunities for biogeochemical processing (Boano et al., 2014). The hyporheic zone is the portion of sediments surrounding the stream that is permeated with stream water. The exchange of water, solutes and momentum between the subsurface and the surface flows is called the hyporheic exchange (Bencala, 2000; Wondzell, 2006). Hyporheic exchange plays a significant role in controlling biogeochemical processes in aquatic environments. As shown in Fig. 1.1, the interfacial exchange phenomena occur over a wide range of spatial and temporal scales. The hyporheic exchange is affected by a number of key processes and parameters including sediment roughness, grain size (Malard et al., 2002), bedform, bed permeability, bed heterogeneity, water flow velocity and unsteadiness (Boano et al., 2014; Cardenas, 2015) and directly influences the fluxes of water and solutes (nutrients, dissolved organic carbon and oxygen, etc.) by transferring momentum and energy across the sediment-water interface.

1.2 Literature Review

1.2.1 Turbulence across the sediment-water interface

At a fundamental level, a river flow can be modeled as a turbulent open channel flow of water overlaying a porous wall. A review of existing studies on turbulence bounded by permeable walls is provided next.

Studies of turbulent flow over permeable beds have addressed the effect of wall permeability on canonical wall turbulence (such as a fully developed turbulent channel flow). These include, for examples, experimental studies of Zagni and Smith (1976), Kong and Schetz (1982), Zippe and Graf (1983), Manes et al. (2011), Kim et al. (2018) and numerical studies of Kuwata and Suga (2016a), Kuwata and Suga (2016b), Fang et al. (2018). Wall permeability is shown to significantly affect the dynamics and statistics of turbulence. Specifically, the effects include a higher friction coefficient, a permeability-dependent von Kármán constant (κ), reduced streamwise velocity fluctuations, and augmented wall-normal and spanwise velocity fluctuations due to a relaxation of wall blocking.

Another focus of study has been on the effects of heterogeneous permeability inside the sediment (for example, see Laube et al. (2018)). A few studies emphasized the importance of the uppermost sediment layer on the transport across the interface (for example, see Kalbus et al. (2009)).

The interfacial flows can be grouped into three regimes (Suga et al., 2011; Voermans et al., 2017) according to the type of dominant flow processes. Such categorization is based on the permeability Reynolds number, $Re_K = u_\tau \sqrt{K} / \nu$ (where u_τ is the friction velocity, K is the permeability, and ν is the kinematic viscosity): (1) an effectively impermeable regime ($Re_K \ll 1$) where attached eddies dominate near-wall dynamics, displaying a broad range of turbulent scales (Cossu and Hwang, 2017); (2) a highly permeable regime ($Re_K \gg 1$) where the interface is characterized by a distinct inflection point of the mean velocity and a predictable frequency of coherent motions due to Kelvin-Helmholtz instability; and (3) a transitional regime ($Re_K \sim o(1)$), where characteristics of both limiting regimes exist. The current work is focused on a scenario similar to river flows over sand beds, i.e., turbulent water flows over sediments with $Re_K \sim o(1)$.

A challenge in understanding the momentum and mass transport across the sediment-water interface is associated with the lack of detailed information on the fluid dynamics at the scale of sediment grains (or particles), especially near the bed surface. This is due to both the difficulty of experimental measurements at the scale of sediment grains as well as the high cost of numerical simulations needed to resolve the full spectrum of scales from individual grains to bedforms—ripples, dunes, pool-riffle structures, etc. The wall-normal protuberances formed by individual grains are characterized as bed roughness (or particle roughness). This is to be differentiated from the protuberances of bed forms, which are formed by clusters of grains and are typically orders-of-magnitude larger compared to the length scale associated with grains.

The bed roughness influences properties of time-average flow and turbulence over permeable walls (Nikora et al., 1998). Many rough, permeable-bed flow studies focused on the role of permeability using similarly structured sediments that vary in particle size; in this case, it is difficult to separate the effect of bed roughness from that of permeability, except for cases with very small particle sizes (Breugem et al., 2006) or cases where the grain packing structure is modified

inside the bed (Fang et al., 2018) only. Manes et al. (2009) compared permeable and impermeable walls with the same roughness and showed that the penetration of turbulent flows into the porous bed leads to higher flow resistance than an impermeable rough bed. Even in the fully rough regime, the friction factor for the permeable bed increases with Reynolds number; this is different from an impermeable-bed turbulent flow which, in the region near the wall, is Reynolds number independent in the fully rough regime (Jiménez, 2004).

The understanding on the effect of roughness isolated from that of permeability is limited. Several existing studies are summarized below. Padhi et al. (2018a,b) experimentally compared two gravel beds with different bed surface roughnesses. They observed that the bed with streamwise oriented gravels which had a higher bed surface roughness generates significantly higher Reynolds stresses, form-induced stresses and turbulent kinetic energy (TKE) flux than the sediment with randomly oriented gravels. Han et al. (2018) conducted large-eddy simulations (LES) of solute transport on synthesized sediments consisting of regularly packed spheres with a layer of small spheres above to simulate roughness in different regimes of rough-walled turbulence. They found that a high roughness Reynolds number (ku_τ/ν , where k is the roughness height) leads to disruption of the diffusive layer and induces turbulent motions that more efficiently transport the solute than does a lower roughness Reynolds number. Kim et al. (2020) experimentally investigated surface and subsurface flows with idealized permeable beds made of cubically packed spheres. Two cases are considered with one exhibiting a smooth interface while the other that embodied a hemispherical surface topography at the SWI. The results show that the presence of bed roughness intensifies the strength and penetration of flow into the permeable bed modulated by large-scale structures in the surface flow, and linked to possible roughness-formed channelling effects and shedding of smaller-scale flow structures from the roughness elements.

While most existing studies focusing on the effects of sediment bed roughness were conducted using regularly packed particles (Manes et al., 2009; Kim et al., 2017; Fang et al., 2018; Kim et al., 2020), natural permeable bed roughnesses are characterized by random shape, orientation, spacing and arrangement of particles. These irregularities potentially affect the pattern and intensity of

turbulence, as well as the transport characteristics across the interface.

1.2.2 Conservative-solute transport in the sediment

In addition to the roughness effects on the water transport mentioned above, the transport of solutes—such as dissolved oxygen and nitrate—across the sediment-water interface may be also important. The role of hyporheic zones in transforming the chemical signature of stream water depends, among other factors, on transport time scales often described using transit time distributions (TTDs) and residence time distributions (RTDs). For a solute mass pulse entering the river bed at time t , the residence time τ is the age of a water parcel in the bed (Elliott and Brooks, 1997b). Transit time, on the other hand, is the residence time (or water age) at the time a parcel of water exits the system, and therefore represents the maximum residence time (or age) that can be attained by a water parcel for a given subsurface flow path. RTDs and TTDs are related and they have both been extensively used in hyporheic zone research. For example, residence times have been used to evaluate the ability of the hyporheic zone to process nutrients (Boano et al., 2014) and to classify hyporheic zones (Harvey et al., 2013). Transit times have been used to understand the kinematics of age mixing processes in advection-dispersion models (Benettin et al., 2013), as well as relations between flow, storage and chloride transport in a small watershed (Benettin et al., 2015; Harman, 2015), to infer changes in water cycle dynamics in managed landscapes (Danesh-Yazdi et al., 2016) and to understand biogeochemical reactions in a dam-regulated river corridor (Song et al., 2020). Median transit times have been used to assess the reaction efficiency of hyporheic flows by defining a Damköhler number representing the ratio of transport and biogeochemical time scales (Song et al., 2020).

Bed geometry and morphology exert a strong influence on exchange fluxes and transit times. Bed geometries are often multiscale, with both large- and small-scale features contributing to the exchange (Persson et al., 2005; Wörman et al., 2006; Aubeneau et al., 2015; Stubbs et al., 2018; Roche et al., 2018; Lee et al., 2020). For example, large-scale features such as bars that scale with bankfull depth and channel width, relatively small-scale features such as bedforms, as well

as even smaller-scale roughness details at the scale of individual grains all influence exchange fluxes. Existing studies on flow and residence/transit times are typically focused on the effects of morphological features such as ripples and dunes that are orders of magnitude larger than individual sediment grains. Elliott and Brooks (1997a,b) conducted analytical studies and lab experiments on the exchange with permeable bedforms. They summarized that bedforms “turnover”. Pumping is the movement of fluid through the bed induced by static pressure variations over bedforms. Turnover occurs as a moving bedform trap and releases interstitial fluid in the bed. The main mechanism driving mass exchange when bedforms are stationary are based on the process of pumping. Elliott and Brooks (1997b) (henceforth referred to as EB97) analytically solved for the velocity field and residence time for an ideal subsurface flow model with a sinusoidal bedform. The solutions were based on a two-dimensional (2D) Darcy equation with prescribed pressure distribution at the bed surface; these solutions described the pumping mechanism of the exchange. The time a fluid particle spends along its subsurface flow path was calculated using a numerical particle tracking approach. For stationary bedforms, it was observed that the sinusoidal head pumping model (Elliott and Brooks, 1997a) can only be used in the initial stage and underpredicts the mass exchange in the later stage. They inferred that additional exchange may be related to bed inhomogeneity or irregular variations in pressure at the bed surface which are not related to bedforms. Such effects are likely to be more pronounced in actual river flows. The model of EB97 considered only advection (by the spatially and temporally averaged Darcy velocity) for flow path tracking, while in Elliott (1991) additional mixing mechanisms (turbulent mixing or molecular diffusion of solutes) were also accounted for by using a random walk method. In all the above methods, a constant solute concentration is assumed in the fluid column; in other words, the flow is assumed well mixed. It is probably different in an actual river flow, as the bed morphology is likely to induced spatial heterogeneity of local solute concentration.

Examples of the application of the Darcy model for subsurface flow calculation and particle tracking to estimate residence time based on advective exchange (EB97) include the following, among many others. Packman et al. (2000) applied a model of pumping exchange to colloid

transport and filtration. They calculated the residence time by superimposing advective transport and particle settling in the bed and included the effect of physicochemical filtration by bed sediment also. Wörman et al. (2002) developed a framework to integrate the residence time estimation based on the method of Packman et al. (2000) into a model of longitudinal solute transport in streams. Many studies, such as Salehin et al. (2004), Sawyer and Cardenas (2009) and Laube et al. (2018), characterized hyporheic exchange within heterogeneous streambeds. It was shown that, in a heterogeneous bed compared to a homogeneous one, more shorter and faster preferential hyporheic flow paths are induced, leading to more rapid net hyporheic exchange and a shallower hyporheic zone. Sawyer and Cardenas (2009) numerically studied the heterogeneity of cross-bedded sediment in which sedimentary structures are roughly horizontal units composed of inclined layers. The results show that the permeability structures do impact the distribution of residence times. Specifically, permeability heterogeneity can increase the proportion of short or long residence times. The shape of the residence time distribution appears to be sensitive to permeability patterns near the sediment-water interface. However, the tails of the residence time distributions follow a power law, regardless of specific permeability structure. Laube et al. (2018) further developed a modeling strategy for an equivalent conductivity tensor for heterogeneous sediments. Recently, several studies analyzed sediment flows using pore-scale simulation data (Sun et al., 2015; Kim and Kang, 2020). For example, Kim and Kang (2020) studied 2D pore-scale transport phenomena across a surface-subsurface interface, based on a Reynolds-averaged Navier-Stokes (RANS) closure.

Most of the studies summarized above quantified residence time using ideal conceptual models of bedform features (such as ripples or dunes). Detailed aspects of solute transport near the bed, including turbulent mixing and pore-scale dynamics, are rarely studied. At the “micro” scale of pore flow, the effects of bed roughness formed by the uppermost-layer of sediment grains and their arrangement on biogeochemical processes are likely to be important, as the benthic biolayer where important nutrient or pollutant processing occurs is limited to a thin layer (of 2-5 cm) beneath the streambed surface (Battin et al., 2008; Harvey et al., 2013; Knapp et al., 2017). In addition, in a warmer climate streambed roughness is expected to increase as a result of enhanced bioturbation—

the effect of small animals, such as chironomid larvae and tubificid worms, within the sediment bed as they rework the sediment (Baranov et al., 2016; Dairain et al., 2020).

The fundamental effects of wall roughness on turbulence were predominantly studied for flows over impermeable walls (see reviews by Jiménez (2004) and Flack and Schultz (2014)). Typically, roughness is categorized as bed height variations in the range between $5\delta_v$ and 0.1δ (where $\delta_v = \nu/u_\tau$ is the viscous length scale and δ is the turbulent boundary layer thickness). Roughness affects turbulence by increasing wall friction and enhancing turbulence production near the wall. It is known to enhance the momentum transfer toward the wall (Jiménez, 2004) and dynamically modify the near-wall flow (Raupach and Shaw, 1982). The effects become more important in non-equilibrium flows (Ghodke and Apte, 2016; Yuan and Piomelli, 2014a, 2015; Mangavelli et al., 2021) where streamwise mean pressure gradients—which can be induced by the presence of bedforms—are significant. In the context of turbulent flow bounded by a permeable wall (such as the region near a sediment-water interface), bed roughness likely affects the flow near the bed and consequently the mass exchange also.

Some insights into how small-scale features of bed topography (e.g., grain-scale irregularities) may affect the exchange were provided by a few studies on multiscale or fractal bed topographies. Aubeneau et al. (2015) performed laboratory measurements of solute transport with sand beds under different flow velocities. They found that fractal properties of the bed topography affect solute residence time distributions. Larger bedforms induced more hyporheic exchange but shorter residence times, as shown by the steeper slope of the washout breakthrough curve. He et al. (2019) applied LES to study the effects of roughness Reynolds number on scalar transport at SWI. They showed that from hydraulically smooth regime ($0 < Re_k \leq 5$, where Re_k is the roughness Reynolds number) to the transitionally rough regime ($5 < Re \leq 70$), the dominant transport mechanism at the interface changes from molecular diffusion to turbulent diffusion. In addition, Lee et al. (2020) analyzed the effect of fractal properties of the bed topography on interfacial flux and residence time, based on sequentially coupled simulations using RANS for the channel flow and a Darcy model for the subsurface flow. Residence times were calculated using the

random walk particle tracking method. They observed that the interfacial flux increases with the fractal dimension of the bed (i.e., prominence of smaller topographical features). In such coupled surface-subsurface model framework (used also by Cardenas and Wilson (2007), Cardenas et al. (2008), and Chen et al. (2015), for examples), the two sets of governing equations are coupled through the pressure distribution along the sediment-water interface. In this case, the accuracy of RANS pressure solution along the interface dictates the accuracy of the coupled simulation. Given the difficulties of RANS simulations in predicting accurately the near-wall flow and flow separation in strongly non-equilibrium wall-bounded turbulence (Yuan et al., 2014; Dutta et al., 2016), pore-resolved simulation or measurement data are needed to characterize near-wall dynamics and provide validation for pore-unresolved modeling.

1.3 Research objectives and outline

The goal of this dissertation is to analyze the effect of morphological details of sediment beds on interfacial turbulence and solute transport in turbulent flows that are representative of river flows on sand beds. To this end, three-dimensional DNS simulations are carried out with synthesized sediments. Both the flow in the water column and the that inside the sediment pores are resolved. Specific questions are:

1. How different are the effects of roughness on a flow over porous wall versus its effects on that over a non-permeable wall? How does sediment bed roughness on a macroscopically flat bed affect the turbulence statistics and structure?
2. How does bed roughness on a macroscopically flat bed influence fluid parcel transit times in the bed? Does small-scale bed roughness lead to significant fluid volumetric flux normal to the interface?
3. To what extent will the grain-scale bed roughness affect the hyporheic exchange with the presence of bedform?

The outline of this dissertation is as follows.

- Chapter 2 describes the methodologies of the sediment synthesis with two different roughnesses, regular and random, and the numerical simulations. Simulation parameters are introduced. The simulations are then validated against existing experimental measurements. Results on how roughness on a flat bed, isolated from the effect of bed permeability, affects the interfacial turbulent flow are discussed.
- Chapter 3 introduces the methodology to calculate the transit time distribution and compares the transit time distribution for the two different roughnesses. The effect of molecular diffusion in the exchange is also quantified.
- Chapter 4 focuses on turbulent flows over a bed with both bedform and roughness. The bedform synthesis and simulation parameters are introduced. The effects of bed roughness geometry on velocities, pressure and transit time are compared. Comparisons are made with flat-bed results discussed in Chapters 3 and 4, to show a different role played by the roughness when a bedform is present.
- Chapter 5 summarizes the major findings and contributions, and describes the plan for future work.

CHAPTER 2

DIRECT NUMERICAL SIMULATIONS OF TURBULENCE AND HYPORHEIC MIXING NEAR SEDIMENT–WATER INTERFACES

2.1 Introduction

The goal of this Chapter is to characterize the detailed effects of different bed roughnesses on aspects of turbulence that are responsible for scalar and momentum transfer, including averaged statistics and flow structural information. Specific questions include the following:

(1) How different are the roughness characteristics corresponding to regular and random arrangements of sediment grains in the top layer?

(2) How does the bed roughness texture influence the dynamics at the individual grain level and the overall interfacial exchange of mass and momentum? Specifically, how important are the additional, form-induced terms in the momentum and stress balances?

To address the above questions, we perform direct numerical simulations (DNS) of fully-developed turbulent open-channel flows over grain-resolved permeable beds with an identical bulk permeability (below the interface region) but different roughnesses produced by either random or regular grain arrangements at the bed surface. The Reynolds numbers based on the open-channel height ($Re_\tau = u_\tau \delta / \nu$, where δ is the open-channel height) and on the permeability (Re_K) are kept constant. This chapter is organized as follows. Section 2.2 introduces the methodology of the simulations and porous-bed synthesis and compares the two different interfaces generated. Section 2.3.1 validates the random sediment synthesis by comparing with the experimental measurements of Vorumans et al. (2017). Section 2.3.2 compares the turbulence statistics and structure as affected by the differences in the interface. Lastly, Section 2.3.3 discusses implications for the hyporheic exchange mechanisms.

2.2 Methodology

2.2.1 Governing equations

The incompressible flow of a Newtonian fluid is governed by the equations of conservation of mass and momentum:

$$\frac{\partial u_i}{\partial x_i} = 0, \quad (2.1)$$

$$\frac{\partial u_j}{\partial t} + \frac{\partial u_i u_j}{\partial x_i} = -\frac{\partial P}{\partial x_j} + \nu \nabla^2 u_j + F_j. \quad (2.2)$$

Here, x_1 , x_2 and x_3 (or x , y and z) are, respectively, the streamwise, wall-normal and spanwise directions, and u_j (or u , v and w) are the velocity components in those directions; $P = p/\rho$ is the modified pressure, where ρ the density. The term F_j in Equation (2.2) is a body force imposed by an immersed boundary method (IBM) to impose no-slip boundary conditions on the fluid-solid interface. The grain geometry is well-resolved by the grid. The IBM is based on the volume-of-fluid approach (Scotti, 2006); its detailed implementation and validation are provided in Yuan and Piomelli (2014b,c). The F_i values are negligible except in the cells that are cut by the immersed solid boundaries. The simulations are performed using a well-validated code that solves the governing equations (2.1) and (2.2) on a staggered grid using second-order, central differences for all terms, semi-implicit time advancement (with second-order Adams-Bashforth scheme for the wall-normal diffusion term) and MPI parallelization (Keating et al., 2004).

Fully developed open-channel flows are simulated with symmetric boundary conditions applied at both top and bottom boundaries of the simulation domain and periodic conditions are applied in x and z . A constant pressure gradient is used to drive the flow.

In the sediment, the presence of grains leads to spatial heterogeneity of the time-averaged variables; these time-averaged fluctuations are separated from turbulent fluctuations using the double-averaging (DA) decomposition introduced by Raupach and Shaw (1982),

$$\phi(x, t) = \langle \bar{\phi} \rangle(y) + \tilde{\phi}(x) + \phi'(x, t), \quad (2.3)$$

	Interface type	θ_{avg}	Re_K	Re_τ	D/δ	D^+	H_s/δ	$(L_x, L_z)/\delta$	$(\Delta x^+, \Delta y_{min}^+, \Delta z^+)$
Case 1	Random	0.41	2.56	178	0.43	76	2.6	(12, 6)	(2.0, 1.5, 2.0)
Case 2	Regular	0.41	2.62	395	0.20	79	0.8	(6, 3)	(1.5, 0.19, 1.5)
Case 3	Random	0.41	2.62	395	0.20	79	0.8	(6, 3)	(1.5, 0.19, 1.5)

Table 2.1: Summary of simulations. θ_{avg} is the average porosity in the bulk of the sediment; D is the sphere diameter; H_s is the sediment depth; L_{x_i} is the domain size in x_i .

where ϕ is an instantaneous flow variable, $\langle \phi \rangle$ is the intrinsic spatial average in the (x, z) -plane, $\langle \phi \rangle = 1/A_f \int_{A_f} \phi dA$ (where A_f is the area occupied by fluid), $\bar{\phi}$ is the temporal average, $\phi' = \phi - \bar{\phi}$ is the instantaneous turbulent fluctuation, and $\tilde{\phi} = \bar{\phi} - \langle \bar{\phi} \rangle$ is the form-induced fluctuation. The area averaging carried out in the total area of fluid and solid, A_o , is termed superficial area averaging, denoted by $\langle \phi \rangle_s = 1/A_o \int_{A_o} \phi dA$; the two averaging approaches satisfy the relation $\langle \rangle_s = \theta(y) \langle \rangle$, where $\theta(y)$ is the plane-averaged porosity at elevation y ,

$$\theta(y) = \frac{A_f(y)}{A_o}. \quad (2.4)$$

The plane-averaged total drag $F_D(y)$, exerted by the grains on the fluid (including both viscous and pressure drag contributions), is calculated using the IBM body force, \bar{F}_1 :

$$F_D(y) = \frac{\rho}{L_x L_z} \int_{A_o} \bar{F}_1(x, y, z) dx dz, \quad (2.5)$$

where L_{x_i} is the domain size in x_i . For a detailed explanation of this method, see Yuan and Piomelli (2014b). The friction velocity, u_τ , is calculated based on the maximum value of the total stress, which are the sum of the the viscous shear stress, turbulent shear stress and the form-induced shear stress.

2.2.2 Parameters

The detailed simulation parameters for all cases are listed in Table 2.1. Two types of SWI – regular and random interfaces – are simulated; their definitions are given in Section 2.2.3. Case 1 is used in Section 2.3.1 to validate the synthesis of the random interface generated with experimental data.

Cases 2 and 3 share a higher friction Reynolds number than that in Case 1; these two cases are used to compare the effects of different interface geometries on the turbulent flow in Section 2.3.2.

In Table 2.1, θ_{avg} is the volume-averaged porosity inside the sediment; its value is kept the same for all cases. The bulk permeability, K , is estimated using the Kozeny-Carman model (Kozeny, 1927; C. Carman, 1937),

$$K = \frac{\theta_{avg}^3}{180(1 - \theta_{avg})^2} D^2, \quad (2.6)$$

where D is the grain diameter. The Kozeny-Carman model has been widely used for multiple types of artificially-generated packed beds, for example, by Voermans et al. (2017) for a random packing of spheres and by Fang et al. (2018) for periodic arrays of spheres. The elevation of $y = 0$ is chosen at the sediment crest, for ease of simulation domain setup. However, $y = 0$ is not used as the virtual origin of the y axis for comparison of flow statistics. Instead, the virtual origin is chosen at the zero-plane displacement, $-d$, which is obtained by fitting the DA velocity to the logarithmic law (shown in Section 2.3.2). H_s is the sediment depth measured from the sediment crest to the bottom boundary of the simulation domain. Figure 2.1(a,b) show the simulation domain and the relation between various lengths and the y axis.

The domain sizes for Case 1 in the x and z directions are 12δ and 6δ , respectively. For Cases 2 and 3 with higher Re_τ values, smaller domain sizes are used. Such domain sizes are considered sufficiently large for the following reasons. (1) The streamwise and spanwise two-point autocorrelations of the streamwise turbulent velocity fluctuations, calculated at $y \leq 0.5\delta$, fall below

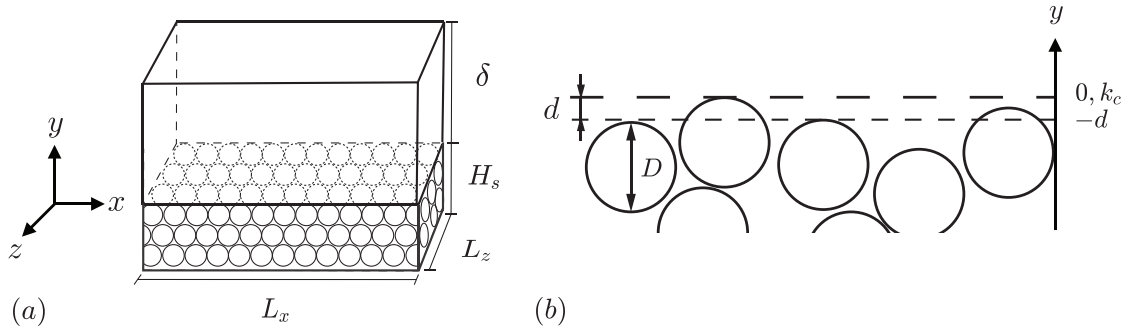


Figure 2.1: (a) Simulation domain and (b) positions of sediment crest, k_c , and zero-plane displacement, d , defined in Section 2.3.2.1.

0.1 at half the domain length or width for all cases. (2) The domain is sufficient for the sediment domains to contain 2000 – 2500 randomly distributed grains to produce statistically converged single-point and two-point turbulent flow statistics. A test is performed for Case 3 with a domain size twice as large in both x and z , which yields similar results. (3) The sediment depth, H_s , is much larger than the penetration depth of turbulence into the sediment, as shown in Section 2.3.2. The total simulation time for each case is at least $T = 25\delta/u_\tau$ after the transient.

The number of grid points are $1024(x) \times 380(y) \times 512(z)$ for Case 1 and $1536(x) \times 478(y) \times 768(z)$ for Cases 2 and 3. For Cases 2 and 3, we have verified that coarsening Δx_i^+ two-fold does not noticeably affect the results shown in this paper. Here, superscript + indicates normalized by viscous length scale, $\delta_v = \nu/u_\tau$. Uniform spacing of grids are used in x and z ; $\Delta x = \Delta z$. The grain geometry is resolved by 36 grid points along each direction in Case 1 and 50 grid points in Cases 2 and 3. In the y direction, 120 grids are used to refine the grid within one diameter distance below the crest; deeper inside the sediment, uniform Δy same as the grid size in x and z is used. Above the crest, the y grid is stretched with finer resolution close to the interface. The minimum vertical grid spaces Δy_{\min}^+ in wall units is 1.5 for Case 1 and 0.19 for Cases 2 and 3. The maximum Δy^+ is 5.3 for Case 1 and 4.2 for Cases 2 and 3.

To provide further evidence that the resolution of 50 grid points per diameter captures well the velocity distribution and forces produced by the spheres, we conducted another simulation of a uniform flow past a single sphere with a set-up similar to Mittal et al. (2008) and compared results to the experimental measurements of Taneda (1956). Two values of the Reynolds number based on grain diameter, DU/ν (where U is the uniform undisturbed velocity), of 75 and 100 are used. These values are similar to or higher than the Reynolds number experienced by the spheres near the interface in this work. Results (not shown) quantify the difference between our DNS and the experimental results as 1-4% for the flow characteristics (separation angle, recirculation bubble size and recirculation center location) and 1 – 1.5% for the drag force. The comparison gives confidence that the results herein, especially the local mean shear layers (important for turbulence production) and the drag force (important for form-induced-stress production (Raupach and Shaw, 1982)) are

well captured by the spatial resolution.

2.2.3 Synthesis of porous beds

Numerical studies of permeable walls usually employ idealized models characterized by regular packing of grains and a constant bed height due to their easy implementation. Examples include a Cartesian grid of cubes used by Breugem and Boersma (2005), a regular packed bed of Breugem et al. (2006), or a simple cubic packing of spheres used in Stoesser et al. (2007) and Fang et al. (2018). Numerical approximations of natural sediments were constructed by, for example, Stubbs et al. (2018), who used a CAD model to design and manufacture an artificial gravel riverbed to approximate a natural bed for both experimental and numerical studies. Here, we implement a different approach based on molecular dynamics (MD) simulations, which are widely applied in flows through porous media with applications in materials science (Khirevich, 2011; Amadio, 2014). The simulations are carried out using the open-source code LAMMPS (Plimpton, 1995) to generate sediments composed of randomly packed, monodisperse hard spheres. The process of pouring hard spheres into a tank is simulated; this process is designed to reproduce the sediment used in the experimental studies of Voermans et al. (2017) (henceforth referred to as VGI17).

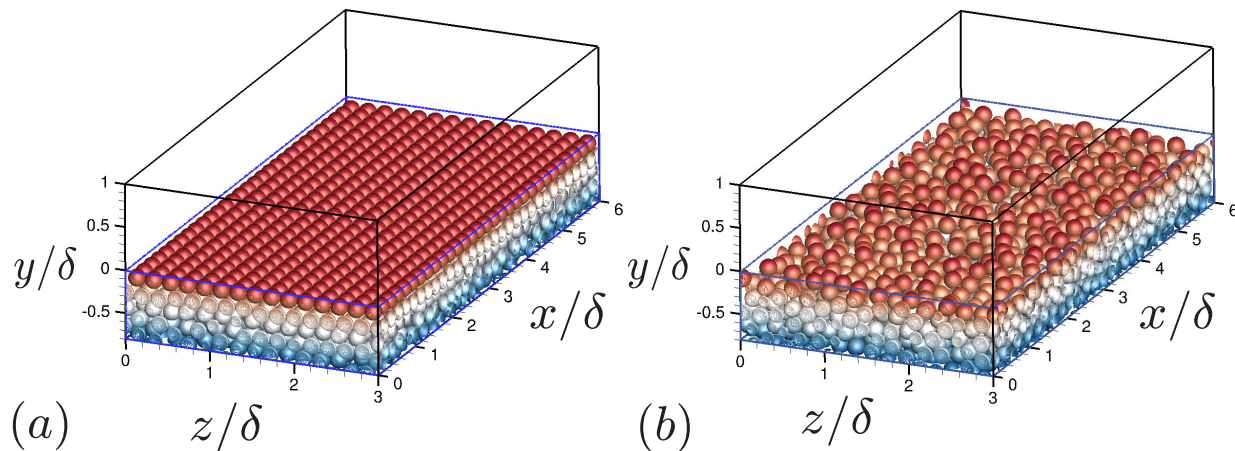


Figure 2.2: Synthesized sediment beds colored by y/δ with (a) the regular and (b) the random interfaces.

Details of the MD simulations are included in Appendix A.

Two types of distribution of the sphere-center locations of the uppermost-layer spheres are generated: (1) regular distribution in (x, z) with constant height, y , called a regular interface, and (2) random values of both (x, z) and y directions, called a random interface. Below the interface, sediments with both types of interface are synthesized using a random sphere distribution that is statistically similar. The total number of spheres are 2633, 2351 and 2116, for Cases 1, 2, and 3, separately. Figure 2.2 compares the sphere distributions in Cases 2 and 3; the difference at the top of the sediments is apparent. These characteristics of the interface can also be expressed in terms of the mean and variance of the permeability in the uppermost sediment layer as well as the correlation length scales in the x and z directions (Section 2.2.4).

2.2.4 Geometrical comparison of the two interface types

The characteristics of the grain distributions in Cases 2 and 3 are compared. First, the plane-averaged porosity profiles along the vertical direction are shown in Figure 2.3. In the interface region ($y \approx 0$), the random interface yields monotonically decreasing porosity with decreasing y , with an inflection point as observed in VGI17. In comparison, the regular sediment yields a

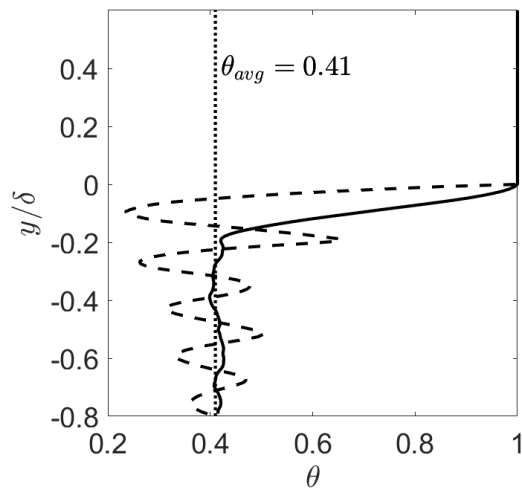


Figure 2.3: Wall-normal profiles of plane-averaged porosity profile for regular (---) and random (—) interfaces.

different pattern, with large-amplitude fluctuations. This is due to the constant sphere height in the uppermost layer. The vertically-averaged porosity inside the sediment is the same between the two cases.

To characterize the positioning of the sediment grains located in the vicinity of the interface, we define the local bed surface height, $h(x, z)$, as the highest sphere-surface elevation at each (x, z) location. Note that this is different from using the sediment-grain center height (which would yield constant height distribution for the regular interface). Since the penetration depths are within one sphere diameter as shown later in Table 2.2, only sphere surfaces within one sphere diameter distance below the crest are considered in calculating $h(x, z)$. The number of top-layer spheres identified in this way are 900 for the regular interface (Case 2) and 632 for the random interface (Case 3). The sediment-height fluctuations, $h'(x, z)$, are defined as the deviations of the local height values $h(x, z)$ from its plane-averaged value. Figure 2.4(a,b) compare $h'(x, z)$ distributions in Cases 2 and 3, normalized by δ . Interpolation is carried out to show a smooth variation for demonstration. The magnitude of $h(x, z)$ fluctuations can be characterized by the root-mean-square value of h' , σ_h . The σ_h^+ values are 17 and 23 for Cases 2 and 3, respectively. The horizontal distribution of $h'(x, z)$

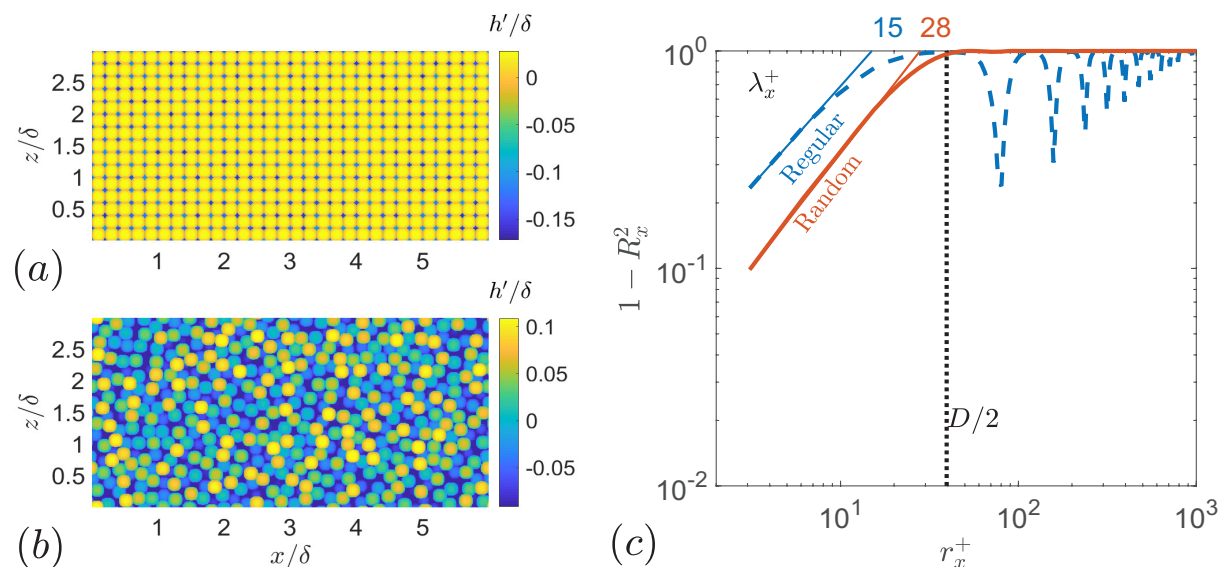


Figure 2.4: Bed surface height fluctuations for the (a) regular and (b) random interfaces. (c) Autocorrelation of height fluctuations and Taylor micro scales.

is characterized here by a Taylor micro scale, λ , determined from a polynomial fit of the two-point autocorrelation R_x of h' , similar to the method used by Padhi et al. (2018a). R_x is calculated as

$$R_x = \frac{1}{A_o} \int_{x,z} h'(x, z)h'(x + r_x, z)dA, \quad (2.7)$$

where r_x is the separation length in x . Figure 2.4(c) shows that λ^+ , estimated using the two-point correlation with streamwise separation, is 15 and 28 for Cases 2 and 3, respectively. The significant difference in roughness length scales affects the apparent permeability in the uppermost sediment layer, as shown in Section 2.3.3.1. The random interface is more heterogeneous with a larger mean and variance of the apparent permeability, although the permeability in the bulk of the sediment is the same.

The probability density functions of $h'(x, z)$ are shown in Figure 2.5. Case 2 (regular) gives a highly skewed probability distribution with a skewness of -2.5 and a kurtosis of 8.7, while Case 3 (random) displays a less skewed but still asymmetric distribution with a skewness of -0.075 and kurtosis of 1.9. The skewness and a kurtosis of Case 3 are well within the ranges for gravel-beds summarized in Nikora et al. (1998), confirming that the interface is random. These observations show that the major differences between the sediment surfaces in Cases 2 and 3 are the larger wall-normal and horizontal length scale for the random case. These lengths are small compared to the grain size ($D^+ \approx 70$); thus, such height fluctuations are considered as roughness, instead

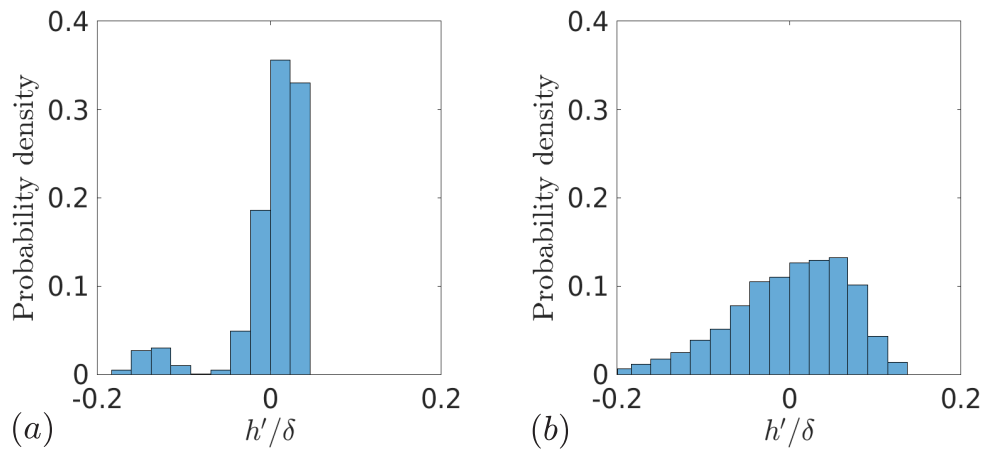


Figure 2.5: Histogram of bed height fluctuations for the (a) regular and (b) random interfaces.

of bedform, whose length scales are much larger than the grain scale. We have also verified that different realizations of the random interface (obtained from separate MD simulations) share similar geometrical characteristics of the sediment surface. For example, another realization of the sediment in Case 1 gives matching values of σ_h/D and λ/D within 1% difference.

2.3 Results

2.3.1 Validation of sediment synthesis

To test how the random interface mimic sediment beds in natural and laboratory settings, we compare Case 1 with the measurements of Case L12 from VGI17. The present values of $\theta = 0.41$ and $Re_K = 2.56$ match those in VGI17 and fall in the range in real aquatic systems. To be consistent with VGI17, in this section we define the location of $y = 0$ to be the location where $\partial^2\theta/\partial y^2 = 0$. Note that for the rest of this paper, $y = 0$ is defined at the sediment crest (while the virtual origin is chosen as $y = -d$ for statistics comparison, as discussed in Section 2.3.2).

The comparison of the mean velocity profile $U = \langle \bar{u} \rangle$ normalized by the DA free-surface (or channel-half-height) flow velocity, U_δ , is shown in Figure 2.6(a). Excellent agreement is obtained.

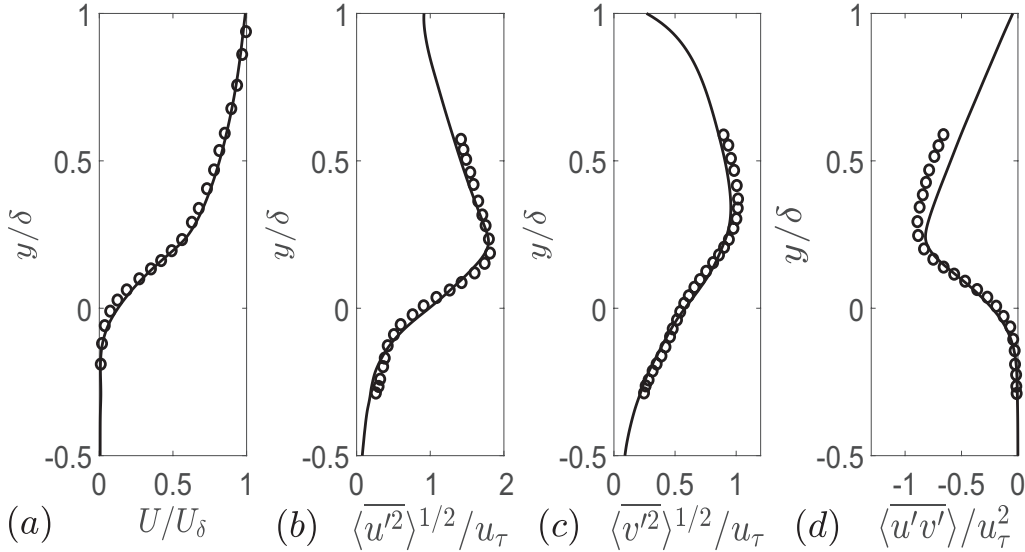


Figure 2.6: Comparison of (a) mean velocity and (b-d) streamwise, wall-normal and shear components of the Reynolds stress tensor. \circ Experiment, — DNS.

Figure 2.6(b-d) show the comparison of the turbulence intensities normalized by u_τ . Very good agreement is obtained and the slight differences in the outer layer ($y/\delta \geq 0.3$) are probably due to the fact that the flow in the experiment at the measurement station is not a fully developed open-channel flow, but resembles a spatially-developing boundary-layer flow.

The intensities of the form-induced fluctuations normalized by u_τ are compared in Figure 2.7. Relatively large discrepancies are found between the present DNS and the experimental measurements. This is at least partially attributed to a difference in the sampling size. The sizes of the sediment domains are similar between the present DNS and the experiment; however, for the DNS, the spatial averaging is carried out throughout the entire (x, z) domain, while the spatial averaging in the experiment was carried out over six lateral measurement frame positions at one streamwise location only. The form-induced stresses have been found highly sensitive to the interface geometry (Nikora et al., 2001; Fang et al., 2018). If we mimic the experimental sampling protocol by applying the spanwise averaging procedure at six uncorrelated spanwise locations and then repeat the procedure for different streamwise locations using the DNS data, we obtain a family of curves

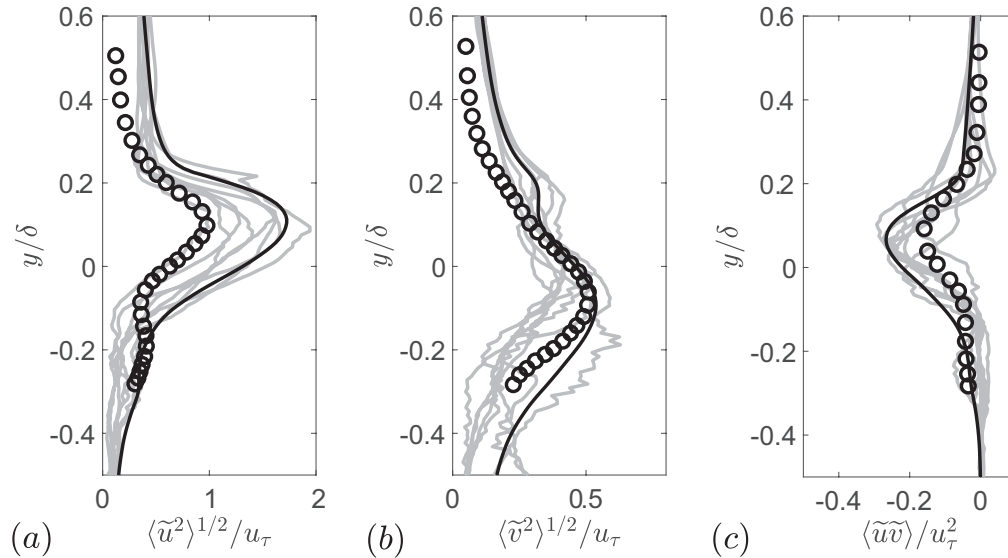


Figure 2.7: Comparison of (a) streamwise, (b) wall-normal and (c) shear component of the form-induced stress tensor. \circ Experiment, — DNS. Black lines represent the values spatially averaged over the entire horizontal plane; grey lines emulate the sampling used in the experiment.

	Interface	κ	d/δ	C_f	δ_b/δ	δ_b^*/δ	δ_p/δ	δ_p^*/δ	$\mu_{\ln(K^*)}$	$\sigma_{\ln(K^*)}^2$
Case 2	Regular	0.32	0.06	0.008	0.078	0.138	0.097	0.157	-6.472	0.005
Case 3	Random	0.33	0.11	0.013	0.055	0.165	0.117	0.227	-5.391	0.055

Table 2.2: Flow parameters for Cases 2 and 3. δ_b and δ_p are Brinkman-layer thickness and Reynolds-stress penetration depth, both measured from $y = -d$; δ_b^* and δ_p^* are the same lengths measured from crest; K^* is apparent permeability.

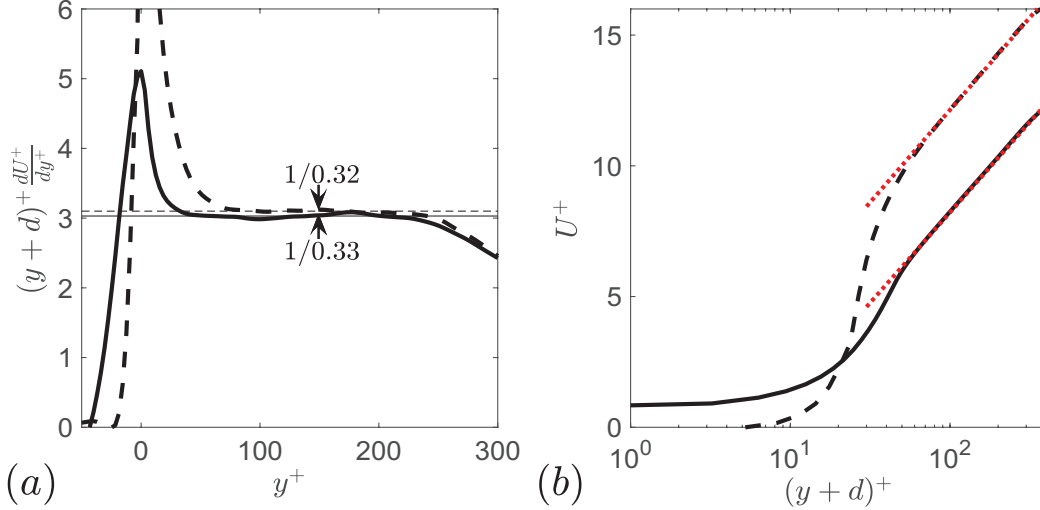


Figure 2.8: (a) Diagnostic function for fitting the logarithmic profile and (b) DA velocity profiles for regular (---) and random (—) interfaces; --- (red) fitted logarithmic profiles.

whose envelope provides an indication of the level of uncertainty in the experimental measurements. Such a family of curves are shown by the gray lines in Figure 2.7 while the black solid lines denotes DNS results using spatial averaging over the entire domain. The VGI17 data points fall within the scatter.

In addition to the uncertainties arising due to sampling size, subtle differences in details of the sphere distribution near the interface may also contribute to discrepancies in form-induced velocity fluctuations. However, since the detailed grain-distribution characteristics are not available from VGI17, we consider the synthesized sediment sufficiently ‘realistic’ as it reproduces quantitatively the turbulence statistics and matches qualitatively the form-induced fluctuations. In comparison, a sediment with a regular interface may yield flow statistics that are drastically different as described in Sec. 2.3.2.

2.3.2 Effects of interface irregularity on flow statistics

In this section, Cases 2 and 3 are compared to understand the effects of interface characteristics on turbulence statistics and structure.

2.3.2.1 DA velocity and friction

The location of the zero-plane displacement, d , and the von Kármán constant, κ , of the wall-bounded flow are determined by fitting the streamwise DA velocity profile to the logarithmic law,

$$U^+ = \frac{1}{\kappa} \log(y + d)^+ + B, \quad (2.8)$$

where B is the intercept of the logarithmic profile. The fitting procedure is similar to the method used by Breugem et al. (2006) and Suga et al. (2010) and is demonstrated in Figure 2.8(a). The fitted velocity profiles are shown in Figure 2.8(b). The fitted values of κ and d are listed in Table 2.2; these values are close to the results ($\kappa = 0.31 - 0.32$ and $d/\delta = 0.06 - 0.1$) reported by Breugem et al. (2006), Suga et al. (2010) and Manes et al. (2011) at similar Re_κ . It is well established that κ for turbulence bounded by a porous wall is smaller than the corresponding value for an impermeable

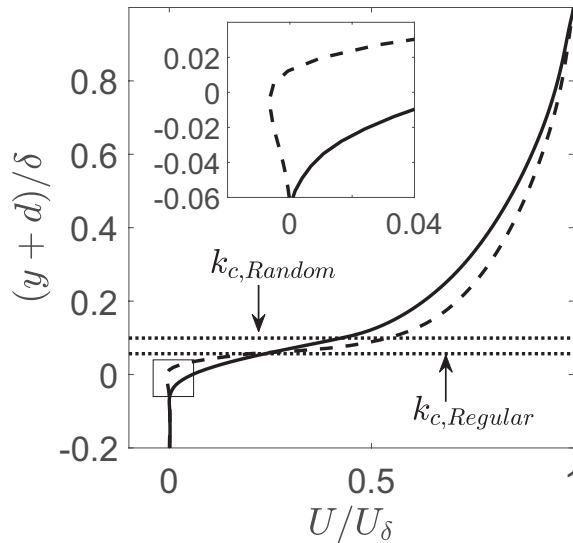


Figure 2.9: DA velocity along y in linear scaling for regular (---) and random (—) interfaces. Inset magnifies the distribution at $y \approx -d$.

wall, which is usually within 5% of 0.41 for both smooth and rough walls. Despite sharing similar κ values, Cases 2 and 3 differ significantly in d . Recalling that d is measured from the sediment crest height, the higher d in Case 3 is probably due to the larger variance in local sediment heights associated with the random interface. In the following plots we offset y by the amount of d to effectively collapse the logarithmic regions between the two cases.

The DA velocity profiles in linear scaling (Figure 2.9) show the differences in the velocities near the interface. The velocity in the vicinity of the regular interface is negative with a small magnitude. This can be related to the organized recirculation regions induced by each sphere at the top layer (discussed in Section 2.3.2.3). This is an important observation with implications for interfacial exchange of solutes. Also, simpler models, especially those that ignore inertial effects, may not be able to capture these features. Such a flow pattern is also described in the conceptual model of Pokrajac and Manes (2009). For lower y , the velocity decreases and eventually reaches a constant, positive value inside the sediment. For the random interface, the velocity variation is monotonic. Both velocity profiles exhibit an inflection point near the sediment crest, consistent with observations of Manes et al. (2011); Voermans et al. (2017).

The depth of shear-layer penetration, δ_b , is defined as the distance from the $y = -d$ to the y location separating the constant-velocity region in the bed and the shear layer above. δ_b is also referred to as the Brinkman-layer thickness. Here, δ_b is calculated in the same way as Voermans et al. (2017), $\langle \bar{u} \rangle_{y+d=-\delta_b} = 0.01(U_i - U_p) + U_p$, where U_i is the DA velocity at $y = -d$ and U_p is the constant velocity deep in the sediment. δ_b is the penetration depth measured from $y = -d$. The value measured from the crest, $\delta_b^* = \delta_b + d$, for the two cases are shown in Table 2.2, equaling 0.138δ (regular case) and 0.165δ (random case). They are of the same order of the grain diameter, as also observed by Goharzadeh et al. (2005).

The friction coefficient is defined as

$$C_f = 2 \left(\frac{u_\tau}{U_\delta} \right)^2. \quad (2.9)$$

Table 2.2 shows that the friction coefficient on the random interface is 70% higher than the regular one. A higher C_f for the random interface is expected as the larger interface length scales (σ_h^+ and

λ^+) lead to higher total drag, similar to the effects of an impermeable wall with a larger roughness length scale.

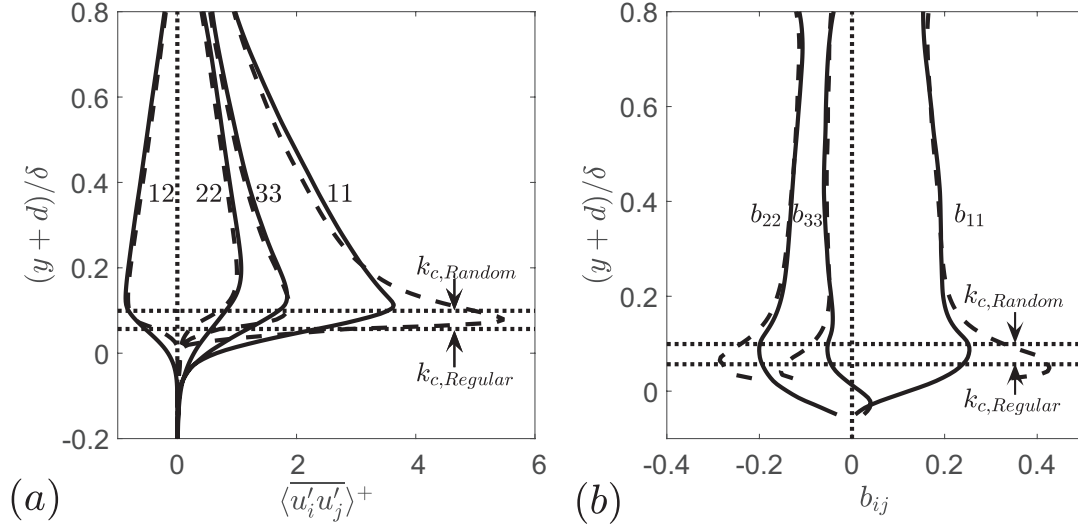


Figure 2.10: Components of (a) the Reynolds-stress tensor and (b) the anisotropy tensor for regular (---) and random (—) interfaces.

2.3.2.2 Turbulent fluctuations

Figures 2.10(a,b) compare the Reynolds stress tensor and its anisotropy between the two cases. The Reynolds-stress anisotropy tensor is defined as

$$b_{ij} = \frac{\langle u'_i u'_j \rangle}{\langle u'_k u'_k \rangle} - \frac{\delta_{ij}}{3}. \quad (2.10)$$

It is shown that Townsend's wall-similarity hypothesis for a wall-bounded flow applies to the outer layer ($y/\delta > 0.2$). As y decreases from the sediment crest, for both cases all components of the Reynolds stress tensor are damped rapidly, together with a decrease of tensor anisotropy. In the interface region, the random interface results in a lower Reynolds stress anisotropy with a higher fraction of TKE residing in v' and w' motions.

The more isotropic turbulence near the random interface is linked to the augmented disturbance from the sediment obstruction to the near-wall turbulent coherent structures. Figure 2.11 compares

the contours of u'^+ at the respective locations of the $\langle \overline{u'^2} \rangle$ peaks in the two cases. The low-speed streaks near the random interface are significantly shorter in wall units than those near the regular interface due to the physical blockage from the spheres serving as roughness elements.

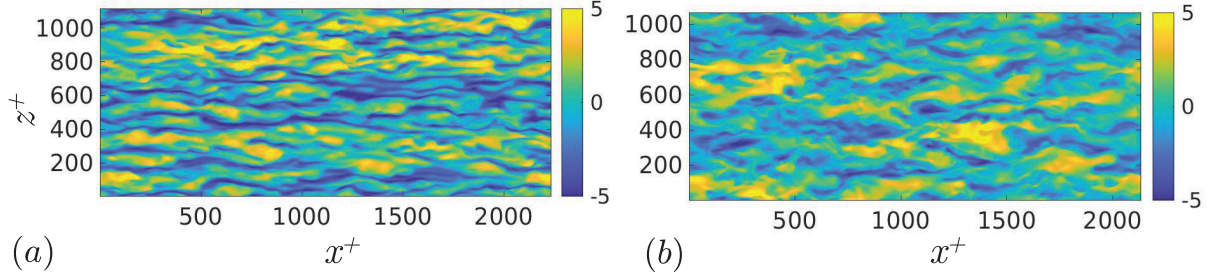


Figure 2.11: Contours of instantaneous u'^+ in the (x, z) plane at the respective $\langle \overline{u'^2} \rangle$ -peak elevations for the (a) regular and (b) random interfaces.

The penetration depth of turbulent shear stress into the bed, δ_p , is obtained from $\langle \overline{u'v'} \rangle_{y=-\delta_p} = 0.01 \langle \overline{u'v'} \rangle_i$, following Voermans et al. (2017), and shown in Table 2.2. $\langle \overline{u'v'} \rangle_i$ is the value of $\langle \overline{u'v'} \rangle$ at $y = -d$. δ_p^* is the same depth measured from the crest. The flow over the random interface gives significantly deeper turbulence penetration, as shown by 47% higher δ_p^* and 20% higher in δ_p compared to the regular interface.

To quantitatively compare turbulent scales, the integral length scales are shown in Figure 2.12.

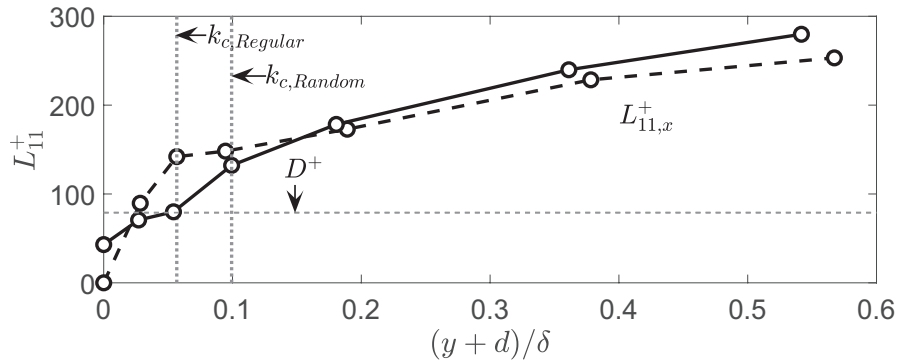


Figure 2.12: Integral length scales of u' motions along the streamwise directions for regular (---) and random (—) interfaces.

It is defined as

$$L_{ij,x_k}(y) = \int_0^\infty R_{ij}(y, \Delta r_k) d(\Delta r_k), \quad (2.11)$$

where

$$R_{ij}(y, \Delta r_k) = \frac{\langle u'_i(y, x_k) u'_j(y, x_k + \Delta r_k) \rangle}{\sigma_{u_i}(y) \sigma_{u_j}(y)}, \quad (2.12)$$

(no summation over repeated indices). Δr_k is the separations along the x_k direction and $\sigma_{u_i}(y)$, $\sigma_{u_j}(y)$ are the root-mean-square of turbulent fluctuations. The integration is carried out to the value of Δr_k at which the correlation coefficient first crosses 0.3. A threshold value between 0.3 and 0.5 is usually used to calculate the integral lengths from two-point correlation coefficients (see, for examples, Krogstad and Antonia (1994), Christensen and Wu (2005) and Volino et al. (2011)). It has been checked that varying this threshold from 0.2 to 0.5 would not noticeably affect the comparison. It is shown that, for the random interface, at $y = -d$ the coherent motions are more extensive in x due to a deeper flow penetration. At the sediment crest, however, the coherent motions are noticeably shorter in x for the random interface, due to the disturbances of the larger roughness height.

Farther away from the interface ($(y + d)/\delta > 0.15$), the difference in the x integral length between the two cases systematically increases with y , indicating a lack of Townsend's wall-similarity hypothesis for this flow quantity. One reason is the relatively high roughness. Jiménez (2004) has proposed that Townsend's hypothesis applies when the roughness height is less than 0.02δ . In the present study, the roughness height (measured from $y = -d$) is at least 0.06δ . Another possible reason is the limited Reynolds number used in the present DNS. The experimental study of Krogstad and Antonia (1994) showed a lack of similarity in the outer-layer L_{11} in x between a smooth-wall and a rough-wall turbulent boundary layer flow. However, a repeated experiment of boundary layer flows by Krogstad and Efros (2012) at a higher Reynolds number indicated reduced discrepancy in the outer-layer L_{11} .

2.3.2.3 Form-induced fluctuations

The form-induced stresses are shown in Figure 2.13. The peak values of all components are much smaller than the corresponding Reynolds stresses, consistent with observations of Manes et al. (2009), Voermans et al. (2017) and Fang et al. (2018). The streamwise form-induced stress near the regular interface region is concentrated in a narrower layer near the crest elevation with a much higher peak value. This is due to the vertical alignment of the wake regions of the grains as shown in Figures 2.14(b,c). Large values of $\langle \tilde{u}^2 \rangle$ are found in the troughs of the top sediment surface and in the wake regions of the surface protuberances. Since these regions are located in a narrow layer near the crest, the distribution of $\langle \tilde{u}^2 \rangle$ is narrower with a larger peak. In contrast, Figure 2.15 shows that, for the random interface the mean recirculation regions can reach much larger sizes and that the penetration of the time-mean flow is much deeper. In addition, $\langle \tilde{v}^2 \rangle$, $\langle \tilde{w}^2 \rangle$ and $\langle \tilde{u} \tilde{v} \rangle$ are higher near the random interface. This may be explained by the higher spatial variation of \tilde{u} associated

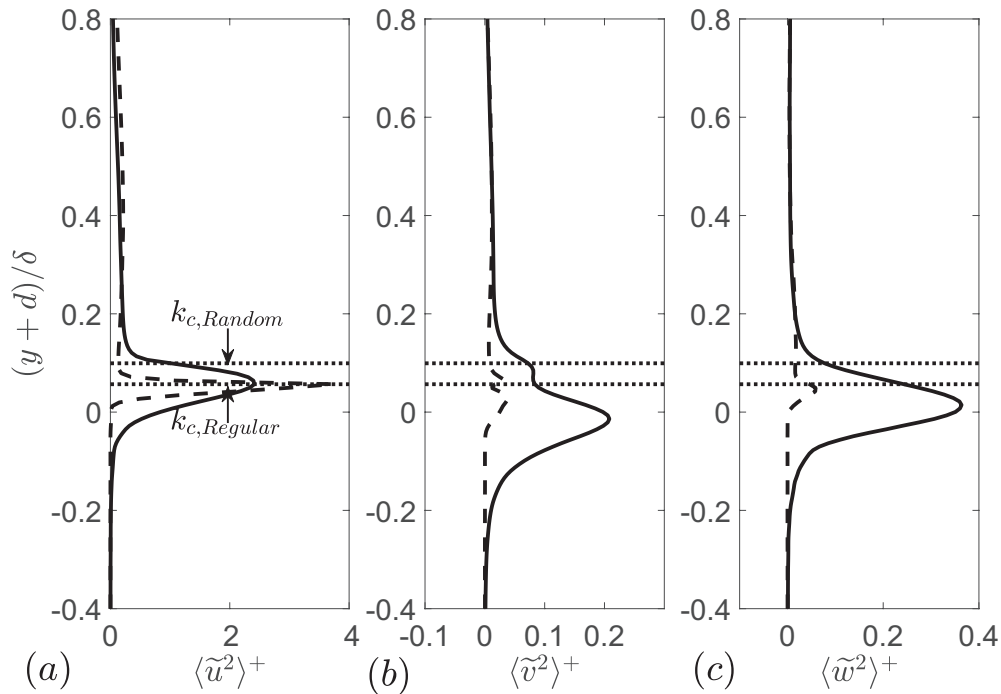


Figure 2.13: Components of the form-induced stress tensor: (a) streamwise, (b) wall-normal and (c) spanwise components, for regular (---) and random (—) interfaces.

with the disordered blockage, which leads to more intense \tilde{v} and \tilde{w} through continuity.

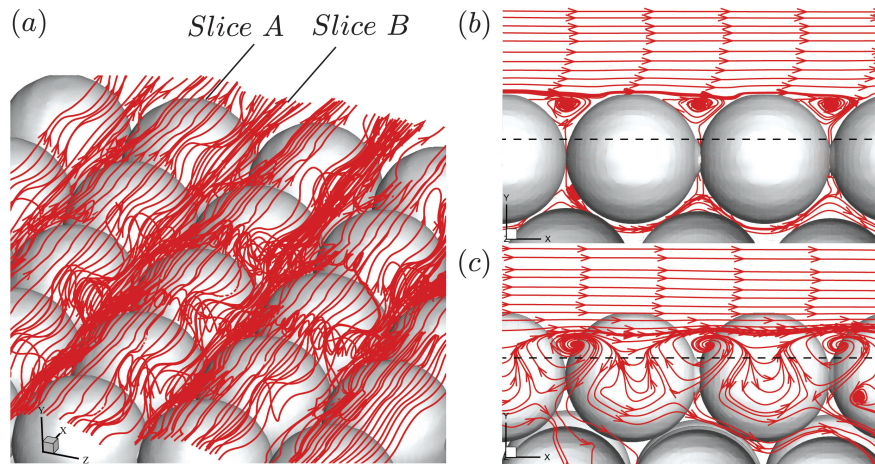


Figure 2.14: (a) Time-averaged streamlines for the regular interface. (b) Streamlines on Slice A ($x - y$ plane across the crests of the grains). (c) Streamlines distribution on Slice B ($x - y$ plane across the valley between two rows of grains). Dash lines indicate $y = -d$.

To analyze the importance of form-induced stresses to the mean momentum balance, we compare the magnitudes of the various shear stresses in Figure 2.16. For the regular interface, the form-induced shear stress is negligible; the viscous shear stress contributes significantly to the total shear stress at the sediment crest. However, for the random interface the viscous shear is weaker due to the milder DA velocity gradient associated with the thicker shear layer; a much stronger

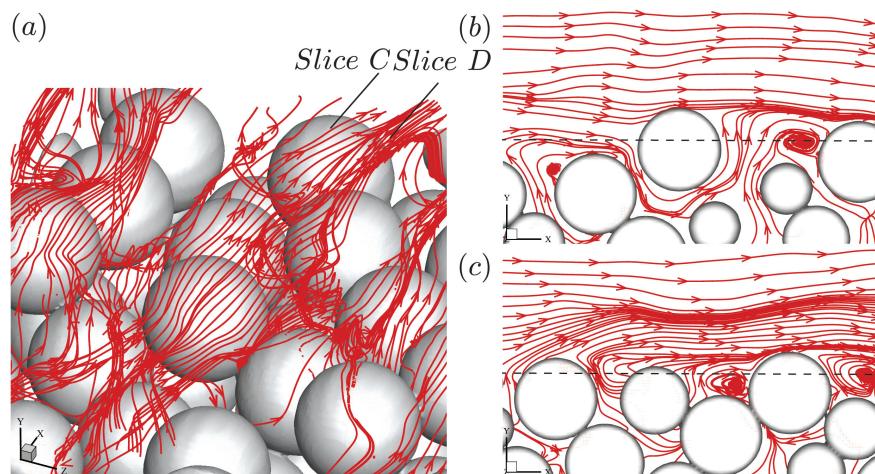


Figure 2.15: (a) Time-averaged streamlines for the random interface. (b) and (c) show streamlines on two $x - y$ planes, Slice C and Slice D. Dash lines indicate $y = -d$.

form-induced stress is present.

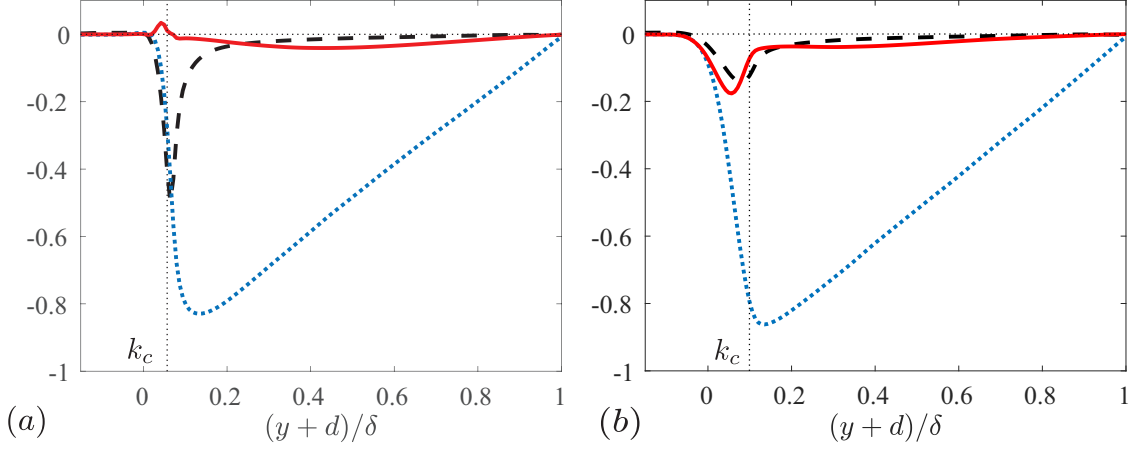


Figure 2.16: Shear stresses for cases with (a) regular and (b) random interfaces: --- Reynolds shear stress, --- viscous shear stress and — (red) form-induced shear stress.

It is important to note that, in the vicinity of the random interface, the form-induced shear stress reaches a similar magnitude of the Reynolds shear stress (Figure 2.16(b)). The fact that the form-induced stress potentially affects the DA velocity near the interface and that it strongly depends on the interface geometry calls for a systematic study of the generation of the form-induced stresses; however, this is beyond the scope of the present work.

2.3.2.4 Reynolds-stress budgets

The budget equations of the normal Reynolds stresses, $\langle u'_\alpha{}^2 \rangle_s$, can be written as (Raupach and Shaw, 1982; Mignot et al., 2009; Yuan and Jouybari, 2018)

$$\begin{aligned}
 0 = & \underbrace{-2\langle \overline{u'_\alpha v'} \rangle_s \frac{\partial \langle \overline{u_\alpha} \rangle}{\partial y}}_{P_s} - \underbrace{2\langle \overline{u'_\alpha u'_j} \rangle_s \left\langle \frac{\partial \overline{u_\alpha}}{\partial x_j} \right\rangle}_{P_m} - \underbrace{2\left\langle \overline{u'_\alpha u'_j} \frac{\partial \overline{u_\alpha}}{\partial x_j} \right\rangle_s}_{P_w} - \underbrace{\left\langle \frac{\partial}{\partial x_j} \overline{u'_\alpha u'_\alpha \overline{u_j}} \right\rangle_s}_{T_w} \\
 & - \underbrace{\left\langle \frac{\partial}{\partial x_j} \overline{u'_\alpha u'_\alpha u'_j} \right\rangle_s}_{T_t} + \underbrace{\nu \left\langle \frac{\partial^2 \overline{u_\alpha{}^2}}{\partial x_j \partial x_j} \right\rangle_s}_{T_v} - \underbrace{2\left\langle \overline{u'_\alpha} \frac{\partial P'}{\partial x_\alpha} \right\rangle_s}_{\Pi} - \underbrace{2\nu \left\langle \frac{\partial u'_\alpha}{\partial x_j} \frac{\partial u'_\alpha}{\partial x_j} \right\rangle_s}_{\epsilon}.
 \end{aligned} \tag{2.13}$$

On the right-hand side, the first three terms are, respectively, shear production (P_s) and additional productions due to the form-induced shear (P_w and P_m). The following three terms are the transport

terms due to the form-induced (wake) fluctuations (T_w), turbulent fluctuations (T_t), and viscous diffusion (T_v). Π is the pressure work and ϵ is the viscous dissipation. Summing over the equations of the three Reynolds-stress components yields the budget equation of the TKE; the sum of the Π terms yields the pressure transport, T_p . The production terms and viscous dissipation of the TKE are shown in Figure 2.17(a), whereas the transport terms are shown in Figure 2.17(b). The residuals are around 3% of P_s peak values.

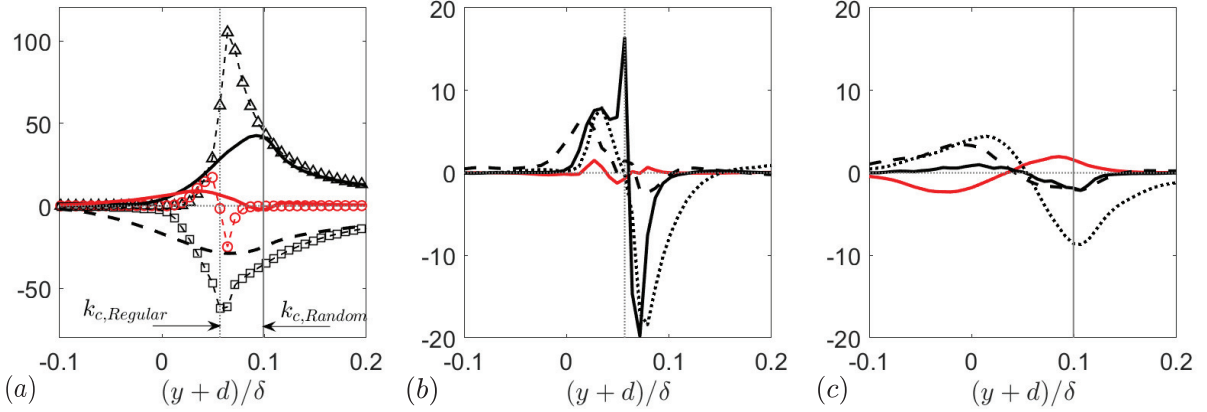


Figure 2.17: Terms in the TKE budget equation. (a) Production and viscous dissipation for regular (symbols and thin lines) and random-interface (thick lines) cases; P_s (—, Δ), $P_m + P_w$ (—, \circ , red) and ϵ (---, \square). Transport terms for (b) regular and (c) random interfaces; T_w (—, red), T_t (---), T_v (—) and T_p (---). All terms are normalized by u_τ^3/δ .

For $(y+d)/\delta \geq 0.2$, the shear production is balanced by the viscous dissipation (not shown). P_s terms reach their maximum values close to the sediment crest. The total amounts of form-induced production ($P_m + P_w$) are significant near the interface, becoming the dominant term a short distance below the crest. Fang et al. (2018) also observed non-negligible form-induced TKE production for regular interface particle distribution with $Re_K = 0 - 27$.

In the vicinity of the regular interface, T_v , T_t and T_p remove TKE from the high-TKE region slightly above the crest and transfer it into the low-TKE region in the bed; T_v dominates other TKE transports due to high $\partial U/\partial y$, while T_w is negligible. In contrast, for the random interface T_v is negligible and the augmented \tilde{v} fluctuations (Figure 2.13) lead to a non-negligible form-induced transport, which works against the other transport processes by moving TKE upward from low-TKE

region in the bed to the crest region corresponding to the TKE peak. Such process contributes to a more equilibrium turbulence (with more energy dissipated at the location where it is generated).

The total form-induced production ($P_w + P_m$) for individual normal Reynolds stresses are compared in Figure 2.18(a). For both cases below the crest, it predominantly contributes to $\langle \overline{u'^2} \rangle$ other than the other two components, more so for the regular interface. P_m can be rewritten as $-2\langle \overline{u'_\alpha v'} \rangle \langle \overline{u_\alpha} \rangle d\theta/dy$. Thus, P_m remains positive for $\langle \overline{u'^2} \rangle$ and is zero for $\langle \overline{v'^2} \rangle$ and $\langle \overline{w'^2} \rangle$. The negative $P_w + P_m$ in both cases in the vicinity of the crest is then due to negative P_w , indicating conversion of TKE to the kinetic energy of form-induced fluctuations, since this term also exists in the form-induced stress budgets with a positive sign (Raupach and Shaw, 1982). Such conversion is probably due to the work of particle drag against the turbulent motions of scales larger than the particles, generating form-induced fluctuations at the scale of the particles. Deeper into the porous bed, the scales of turbulent motions are rapidly reduced and are smaller than that of the particles (as shown by the integral scales in Figure 2.12); here, the particle-scale form-induced shear layers generates turbulence, represented by positive P_w .

The pressure work for a normal Reynolds stress is decomposed into the pressure transport and

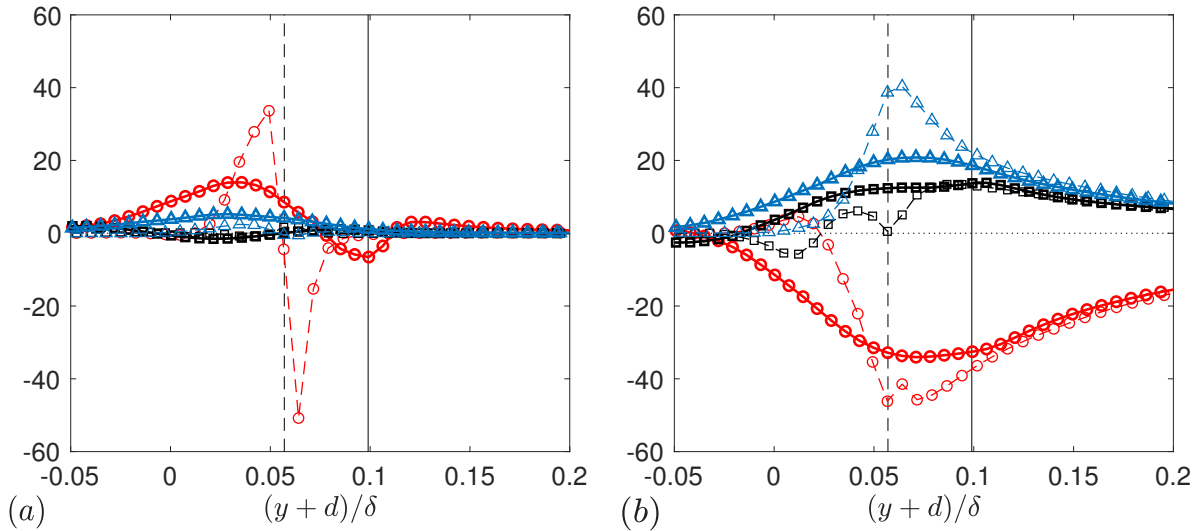


Figure 2.18: (a) Form-induced production and (b) pressure-strain-rate term in regular (---) and random interface (—) cases for the budgets of $\langle \overline{u'^2} \rangle_s$ (\circ , red), $\langle \overline{v'^2} \rangle_s$ (\square) and $\langle \overline{w'^2} \rangle_s$ (\triangle , blue); normalization is done with u_τ and δ .

a pressure-strain-rate term, $\mathcal{R} = 2\langle \overline{P' \partial u'_\alpha / \partial x_\alpha} \rangle_s$. The latter is compared in Figure 2.18(b). \mathcal{R} distributes energy among different normal components of the Reynolds stress tensor; it forms the primary source for v' - and w' - energy budgets that balances the viscous dissipation. The main difference is that, at the crest of the regular interface the u' energy converts mostly to that of w' , with $\mathcal{R}_{22} \approx 0$, while \mathcal{R}_{22} and \mathcal{R}_{33} are of comparable magnitudes at the crest for the random case. Liu and Katz (2018) observed experimentally that, in a shear layer formed over an open cavity, the magnitude of \mathcal{R}_{11} is an order of magnitude higher than \mathcal{R}_{22} . The similar observation herein may also be attributed to the local mean shear layers formed above the topmost-layer particles, shown in Figure 2.19 using time-mean spanwise vorticity in an (x, y) plane. Such shear layers are stronger and aligned in y above the regular interface, while the random distribution of particle for the random interface results in a spread in such effect on energy redistribution.

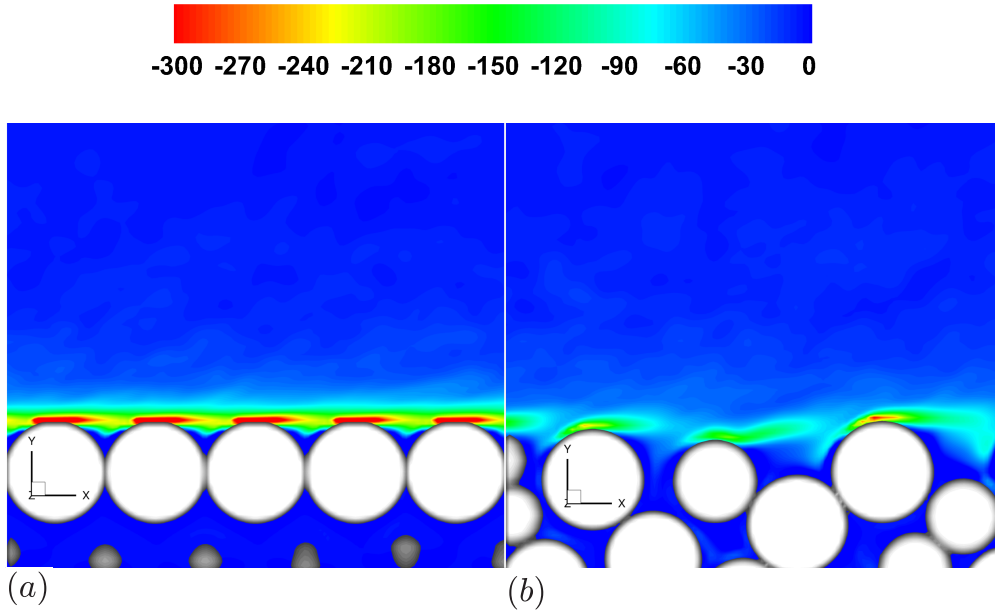


Figure 2.19: Time-averaged spanwise vorticity $\overline{\omega}_z$ normalized by u_τ/δ at (a) Slice B of the regular interface and (b) Slice D of the random interface.

2.3.3 Implications for the mechanism of flat-bed hyporheic exchange

2.3.3.1 Variation of apparent permeability

As a convention of the oil and gas industry (Edwards et al., 1990; Huang et al., 2006; Javadpour et al., 2009), the apparent permeability, K^* , is used to establish a relationship between mean velocity and macroscopic pressure gradient in a finite Reynolds number flow inside a porous medium. Here, the local value of K^* is obtained based on the local volume-averaged velocity and the gradient of the local volume-averaged pressure,

$$\langle \bar{u} \rangle_s(x, y, z) = -\frac{K^*(x, y, z)}{\mu} \frac{\partial \langle \bar{p} \rangle(x, y, z)}{\partial x}, \quad (2.14)$$

where $\langle \cdot \rangle_s$ and $\langle \cdot \rangle$ indicates, respectively, the superficial and intrinsic volume averaging performed locally (within a volume much larger than a grain size). Normalized by u_τ and δ , Equation (2.14) becomes

$$\langle \bar{u} \rangle_s^+ = -Re_\tau \left(\frac{K^*}{\delta^2} \right) \left(\frac{\partial \langle \bar{P} \rangle^+}{\partial x/\delta} \right), \quad (2.15)$$

keeping in mind that $P = p/\rho$. For convenience, from here on write the dimensionless K^*/δ^2 as K^* . Note that K^* is not the Darcy permeability, but a macroscopic descriptor of the complex flow

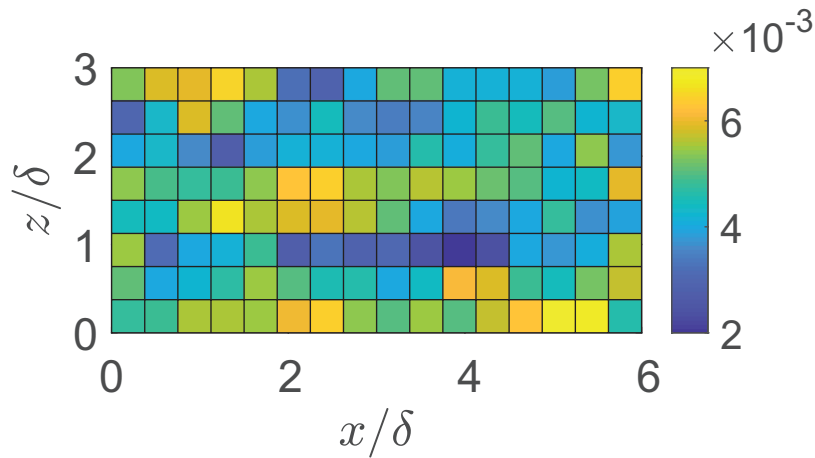


Figure 2.20: Horizontal variation of the apparent permeability K^* in the Brinkman layer in the random-interface case.

at the interface, including the influences of both diffusion of the mean momentum (traditionally modelled using the Brinkman correction (Brinkman, 1949)) and microscopic inertial and drag forces (traditionally modelled using the Forchheimer's correction (Hassanizadeh and Gray, 1987).)

Since the Brinkman layer (measured from crest) has a thickness (δ_b^*) of the order of a sphere diameter, K^* in this layer is considered constant along y , but varying in x and z , in this layer. To calculate such $K^*(x, z)$, we divide the Brinkman layer horizontally into small segments of a size of $2D \times 2D$ in x and z . Enlarging the segment size to $4D \times 4D$ or $8D \times 8D$ does not fundamentally change the observation. The velocity and pressure values in Equation (2.14) are spatially averaged in each small segment respectively; the pressure gradient for each segment is obtained using second-order central difference. The (x, z) distribution of K^* for the random interface is shown in Figure 2.20; the variation for the regular interface is between 1×10^{-3} and 2×10^{-3} , barely visible using the same color bar and is thus not shown. The random interface leads to a much more heterogeneous permeability distribution with a higher mean value. Based on its natural logarithm, the mean, $\mu_{\ln(K^*)}$, and the variance, $\sigma_{\ln(K^*)}^2$, are calculated and summarized in Table 2.2. For the regular and random interfaces, respectively, the $\mu_{\ln(K^*)}$ values are -6.5 and -5.4 (or twice higher in mean apparent permeability for the random case) and the $\sigma_{\ln(K^*)}^2$ values are 0.005 and 0.055 . Since the square root of permeability has a physical meaning of the effective pore size (Breugem et al., 2006), the results here show that the random interface increases the effective pore size at the interface associated with a larger apparent permeability. This is consistent with the larger streamwise integral length scales of u' motions at $y \approx -d$, as shown in Figure 2.12.

The K^* value is also calculated below the Brinkman layer using equation (2.15). Here, K^* becomes the bulk permeability, K , associated with laminar flow inside the porous medium, which is typically predicted using a semi-empirical model such as the Kozeny-Carman equation. The value of $\ln(K^*)$ obtained using the DNS data is almost a constant of -10.9 , regardless of location. Such value indicates a K^* that is almost two order-of-magnitude smaller than the value in the Brinkman layer. In comparison, the Kozeny-Carman equation predicts a $\ln(K)$ value of -10.0

inside the bulk of the sediment, overestimating the bulk permeability by almost 1.5 times.

In the next section, it will be shown that the spatial variation of apparent permeability in the Brinkman layer of the random interface is correlated with the roughness geometry. As K^* in the Brinkman layer incorporates the effect of both macroscopic diffusion and microscopic inertia on the macroscopic (volume-averaged) velocity, we focus on the spatial variation of these two mechanisms as affected by the roughness geometry.

2.3.3.2 Momentum transport mechanisms and dependence on roughness geometry

The double-averaged u -momentum equation can be written as (Raupach and Shaw, 1982)

$$-\frac{\partial \langle \bar{P} \rangle_s}{\partial x} + \underbrace{\left(\nu \frac{\partial^2 \langle \bar{u} \rangle_s}{\partial y^2} - \frac{\partial \langle u'v' \rangle_s}{\partial y} \right)}_{\mathcal{D}} - \underbrace{\left(\frac{\partial \langle \bar{u}\bar{v} \rangle_s}{\partial y} + F_D \right)}_{\mathcal{I}} = 0, \quad (2.16)$$

where F_D is the total drag per unit mass (sum of both pressure drag and viscous drag around the grains). According to Whitaker (1996), the viscous and Reynolds shear stress terms represent the effects due to diffusion of the mean momentum, usually modelled using the Brinkman correction;

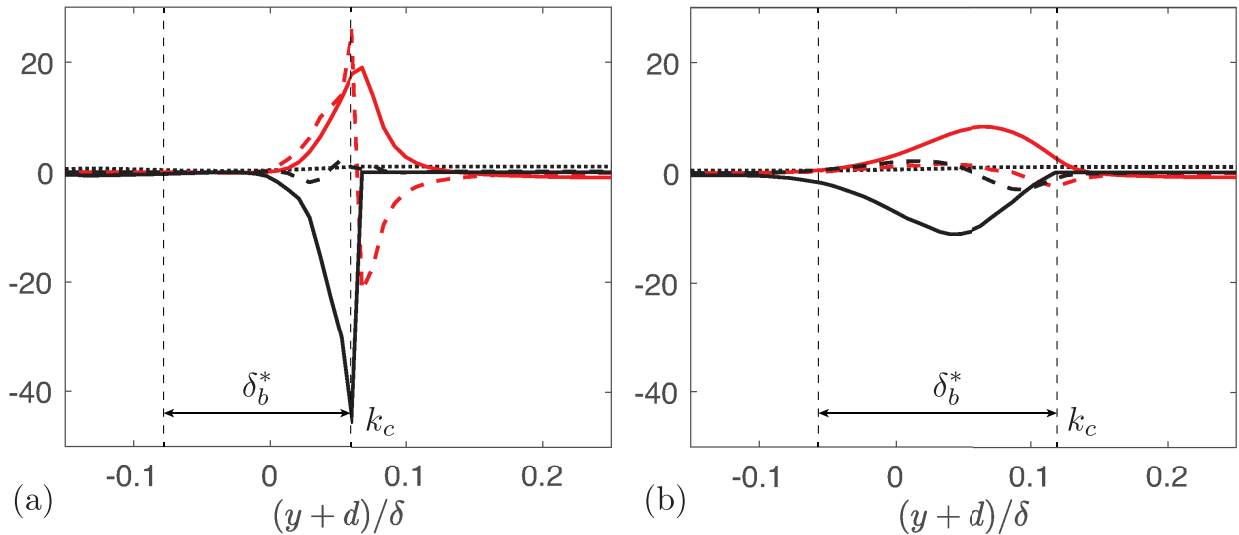


Figure 2.21: Terms in the DA u -momentum equation (equation (2.16)), normalized by u_τ^2/δ for (a) regular and (b) random interfaces: Reynolds-stress term(—, red), viscous stress term(---, red), total drag (—), form-induced stress term(---) and pressure-gradient term(---).

the sum of these two terms is denoted herein as \mathcal{D} , representing ‘diffusion’. The terms related to the form-induced fluctuations (i.e., the form-induced shear stress and the total drag) represent the effects of fluid inertia at the grain scale on the mean momentum, usually modelled by the Forchheimer’s correction. Their sum is denoted as \mathcal{I} , representing (microscopic) ‘inertia’.

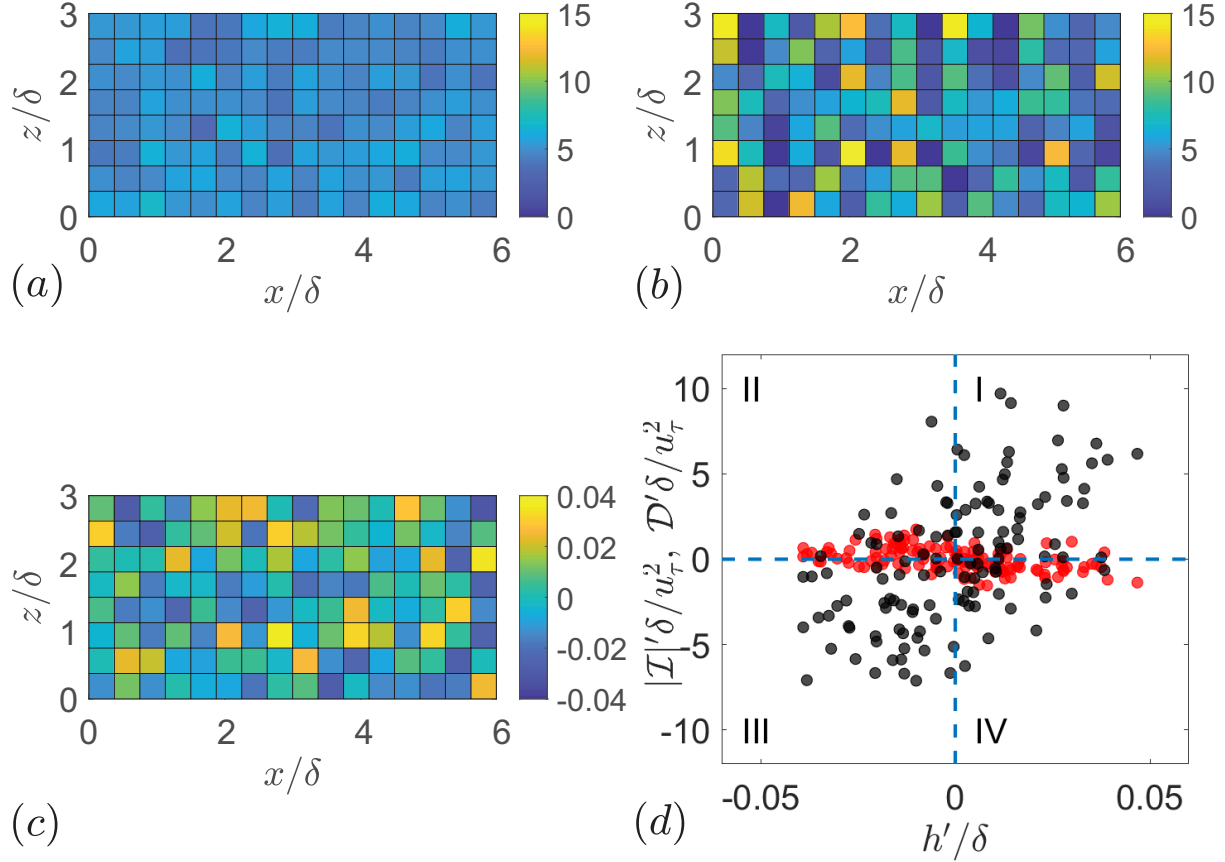


Figure 2.22: Horizontal variation of local volume-averaged \mathcal{D} (a) and $|\mathcal{I}|$ (b), both normalized by u_τ^2/δ . (c) sediment surface height fluctuations h' normalized by δ for the random-interface case. (d) Correlations of \mathcal{D}' (red) and $|\mathcal{I}'|$ (black) with h' .

Figure 2.21 shows the balance of equation (2.16) across the interface, with the spatial averaging performed using area averaging in the x - z plane of the whole domain. The residual is less than 2.3% of the peak magnitude of the total force term for the two cases. For both cases, the spatial-averaged values of \mathcal{D} and \mathcal{I} are both significant inside the Brinkman layer, approximately balancing each

other as the pressure gradient is comparatively weak. The total drag is the main contributor to \mathcal{I} for both cases. For the regular interface, \mathcal{D} is contributed almost equally by both Reynolds and viscous stresses, while it is predominantly due to the Reynolds stress for the random one; this is consistent with the observations made for shear stress distribution (Figure 2.19). The total drag peaks at the crest for the regular interface. This is because the main contributor of F_D —the pressure drag—is caused by recirculation regions, which are distributed uniformly near the crest for this case. For the random interface, recirculation regions of various sizes are formed due to various scales of roughness protuberances, leading to a peak of F_D below the crest.

We now explore potential correlation between the geometry of the random interface and the (x, z) variation of locally-averaged \mathcal{D} and \mathcal{I} magnitudes inside the Brinkman layer. The same local volume-averaging method described in Section 2.3.3.1 is used. The results for the regular interface are not shown, as the variations are barely visible using the same range of contour levels. Figures 2.22(a) and (b) compare the (x, z) distribution of locally averaged \mathcal{D} and $|\mathcal{I}|$, respectively. The spatial average is similar for both contours, a result of relatively weak pressure gradient discussed earlier. The spatial variation is much more intense for $|\mathcal{I}|$ than for \mathcal{D} . This indicates that, though roughness leads to local augmentation of $\overline{u'v'}$ (predominantly through wake-induced production), such spatial variation is rather weak and does not significantly affect the (x, z) pattern of wall-normal $\langle \overline{u} \rangle_s$ transport. In contrast, the pressure drag is generated by the small-scale wake of each grain. Therefore, $|\mathcal{I}|$ is more sensitive to the local roughness height. Visual comparison with the roughness height distribution $h'(x, z)$ in Figure 2.22(c) shows that the distributions of $|\mathcal{I}|$ and h' are somewhat correlated. Indeed, the scatter plot (Figure 2.22(d)) of h' and the spatial fluctuation of $|\mathcal{I}|$ (departure from the x - z mean) displays a positive correlation (with preferred distribution in Quadrants I and III). This is consistent with the expectation that a high roughness protuberance tends to generate a large (in y) recirculation region and, consequently, a higher-than-average value of pressure drag at the corresponding (x, z) location.

As K^* describes the global effect of both \mathcal{I} and \mathcal{D} , the K^* contour in Figure 2.20 also displays correlation with $h'(x, z)$ distribution; the correlation is negative as a higher local drag serves as a

stronger momentum sink.

2.3.3.3 Mechanisms producing vertical mass flux

The hyporheic flux (Q_H) quantifies the magnitude of mass exchange across the interface during a period of time; it is defined as the wall-normal volumetric flow rate at $y = -d$ directed out of the permeable bed (Elliott and Brooks, 1997b),

$$Q_H(T) = \frac{1}{A} \int_{(x,z)} \overline{v(t,x)|_{v>0}}^T dA, \quad (2.17)$$

where $\overline{(\)}^T$ denotes running time averaging within a window size T and A is the fluid area of the x - z plane at $y = -d$. Figure 2.23(a) shows the variation of the vertical flux, Q_H , as a function of T . The error bars quantify the variance of the values obtained from the DNS data for each T ; the variance is zero for T equal to the total simulation time and increases with decreasing T . For T much larger than the large-eddy turn-over time, δ/u_τ , the form-induced wall-normal velocity (\tilde{v}) is the only contributor of Q_H , while for $T < \delta/u_\tau$ the turbulence fluctuation (v') also contributes to the exchange. Evidently, the contribution of \tilde{v} is more significant than that of v' for both interfaces.

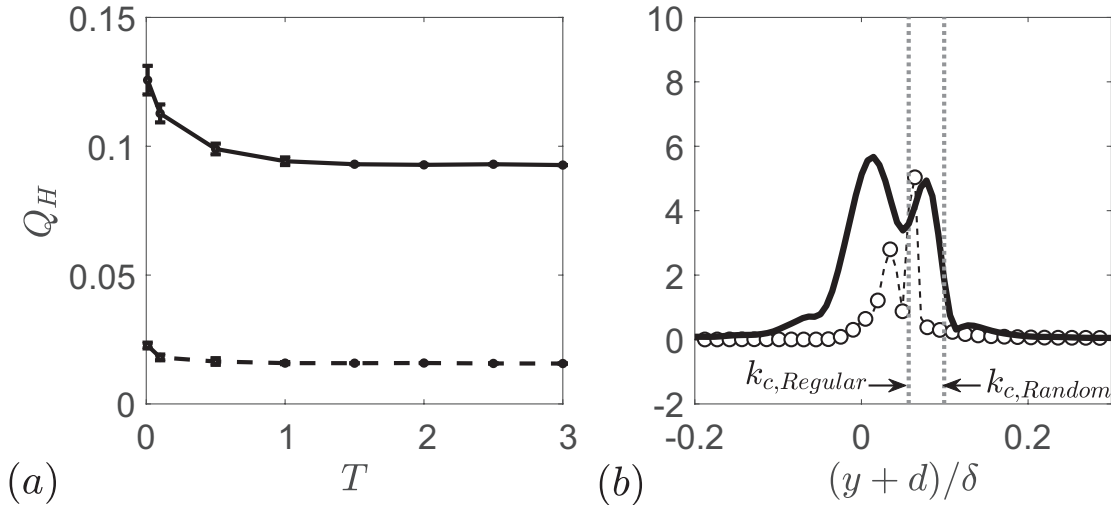


Figure 2.23: (a) Wall-normal flux at $y = -d$ normalized by $u_\tau \delta^2$ with different averaging window sizes $T u_\tau / \delta$ for regular (---) and random (—) interfaces. (b) Pressure-work term of $\langle \tilde{v}^2 \rangle_s$ budget normalized by u_τ^3 / δ for regular (---, O) and random (—) interfaces.

Also, Q_H is around 5 times larger for the random interface compared to the other, consistent with the more intense Reynolds and form-induced stresses near $y = -d$.

The mechanisms governing v' energy transport have been discussed in Section 2.3.2.4 using the stress budget. For the transport of \tilde{v} energy, studies on impermeable flows over rough surfaces (Raupach and Shaw, 1982; Yuan and Piomelli, 2014c) showed that the process is governed by the work done by the form-induced pressure, $\tilde{\Pi} = -2\langle \tilde{v} \partial \tilde{P} / \partial y \rangle_s$, as the main source, the wake production predominantly as a sink. The wall-normal variation of $\tilde{\Pi}$ is compared in Figure 2.23(b); the much higher overall value for the random interface is due to the more intense \tilde{P} fluctuations (shown in Figure 2.24 in a $(x-y)$ slice for each case) leading to significant $\partial \tilde{P} / \partial y$ near the interface.

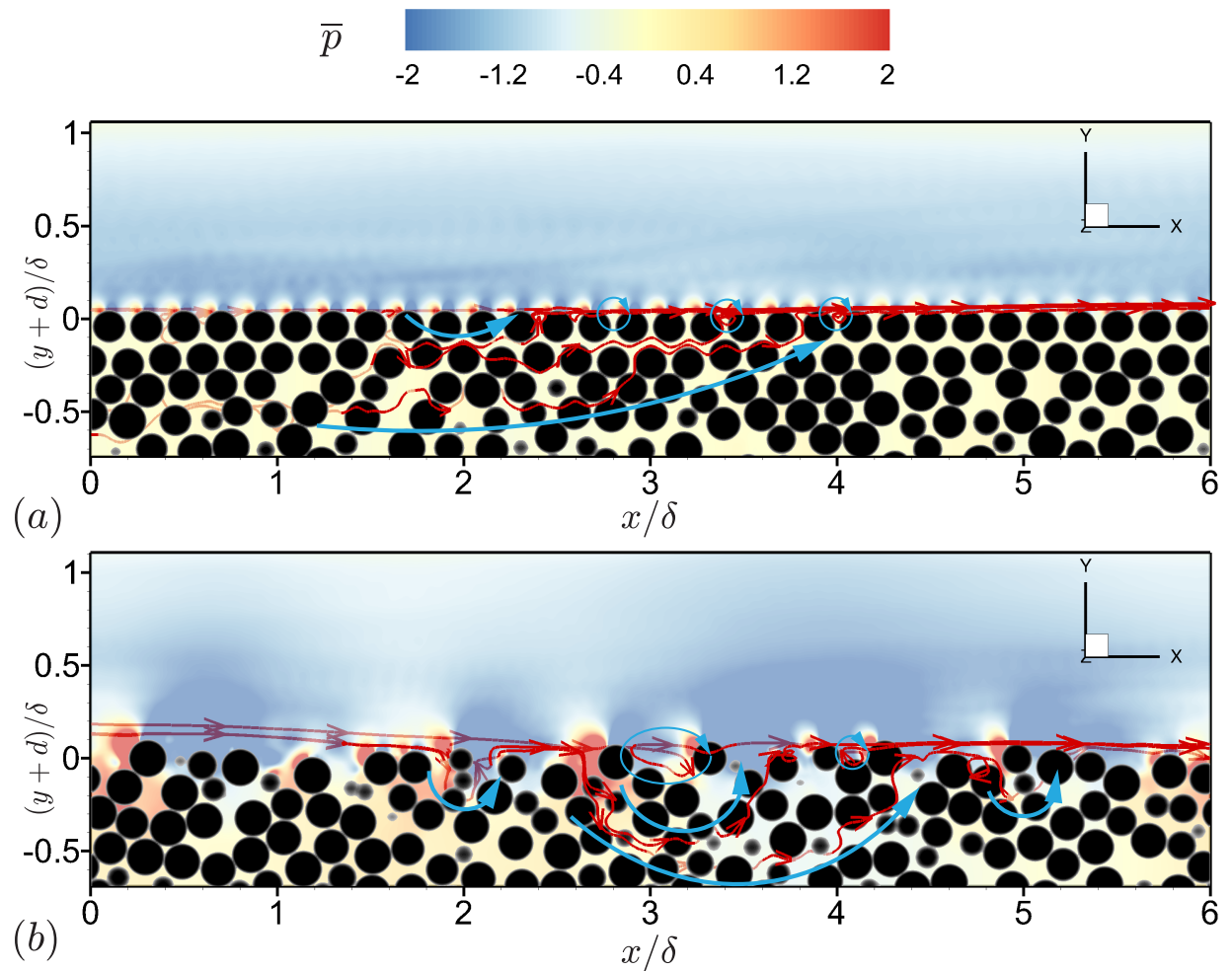


Figure 2.24: Time-averaged pressure variation and 3D mean streamlines for (a) regular and (b) random interfaces. Blue arrows indicate examples of hyperheic flow paths.

Thus, the main difference between the Q_H generation in the two cases is that the random particle arrangement leads to larger-scale and more intense time-mean pressure variations which, by working against the time-mean velocity, generates more intense \tilde{v} near the interface and promotes vertical momentum exchange. Meanwhile, v' is also intensified by the pressure work near the interface, also contributing to Q_H , though with a smaller magnitude.

The hyporheic flow paths are also of interests due to their impact on important macroscopic exchange parameters such as the residence-time distribution and the penetration depth. Below the region of turbulence penetration ($1D$ below the crest), the flow is steady and, consequently, the mean streamlines shown in Figure 2.24 can be interpreted as the hyporheic flow paths of particles released from the upstream.

For the regular interface, the spatial variation of \tilde{P} shows distributions with alternating negative and positive values with a length scale of one sphere diameter, representing organized mean recirculation regions that are shown in Figure 2.14 (b) and (c). The main mechanism of vertical time-mean exchange is due to these organized recirculation regions at the interface. The relatively low K^* at the uppermost layer of the regular interface limits communication between the flows inside the sediment and in the region above; thus, in the sediment, there is little vertical exchange and the lateral flow paths are long.

In contrast, for the random interface, the hyporheic flow paths display a multiscale pattern with short flow paths near the interface and longer flow paths in the shape of circular arcs reaching deeper into the bed. These paths are similar to those visualized through dye transport for a flat bed in the experiments of Packman et al. (2004). Near the bed, the strong \tilde{P} gradients of larger coherence length induce flow infiltration near the bed, reminiscent of bedform-induced advective pumping (Packman et al., 2004). This also results in more intense \tilde{v} , increasing form-induced mixing. The streamwise lengths of the flow paths appear to be reduced as the wall-normal communication is strengthened.

2.4 Conclusions and discussions

We reported DNS results for fully-developed turbulent flows in an open channel on grain-resolved sediment beds with either regular or random grain positioning at the sediment-water interface. The random interface results in a particle roughness with significantly larger root-mean-square height and longer horizontal correlation lengths. These length scales are much smaller compared to those typical of a bedform. Thus, the interface height variation is considered as roughness. A comparison with experimental measurements using randomly poured spheres shows that the case with random interface yields matching flow statistics. It is thus considered as a good approximation of a realistic sediment.

Detailed DNS results obtained with regular and random interfaces with matching $Re_\tau = 395$ and $Re_K = 2.6$ are compared. The differences in the effects on the turbulence and the mass and momentum exchange across the interface are summarized as follows. (1) As a main difference between the two cases, the larger roughness length scales brought by the random interface results in less organized distribution of mean recirculation regions at the interface and more intense \tilde{P} variations at larger scales. The result is a higher \tilde{v} production and, consequently, more isotropic form-induced stress tensor and significant form-induced shear stress (that is comparable to the Reynolds shear stress). It is shown that \tilde{v} , as opposed to v' , is the main contributor to the wall-normal hyporheic flux across the interface for both regular and random interface roughness. Consequently, the hyporheic flux is significantly higher for the random interface than for the regular one. (2) The vertical spread-out of the mean-shear-layer distribution near the random interface leads to a more even TKE redistribution for v' and w' fluctuations and consequently a more isotropic Reynolds stress tensor. The form-induced fluctuations also modulate the total production of Reynolds stress through conversion between TKE and WKE, as well as introducing an additional diffusion process that transports energy from the low-TKE region to the high-TKE region. (3) More intense mixing is observed near the random interface due to augmented Reynolds and form-induced shear stresses; this is reflected by a deeper turbulence penetration (44% higher δ_p^*) and a higher apparent permeability (twice higher K^*) in the Brinkman layer. The local apparent

permeability in this layer is negatively correlated with the local height of roughness. Moreover, the strengthened communication between the surface and subsurface flows for the random interface leads to shortened and deeper-reaching hyporheic flow paths.

Regarding how the type of interface roughness influences the effects of wall permeability, the results show that the penetration depths of mean shear and turbulence are significantly increased by the random roughness. However, the roughness type does not appear to noticeably modify the von Kármán constant (which is lower on a permeable wall than on an impermeable one), as long as the same type of packing is used inside the sediment. Lastly, the Kelvin-Helmholtz (K-H) instability due to wall permeability and the K-H rollers, if present, may also be affected differently by the two roughness types. The K-H instability is, however, expected to be very weak in this work as $Re_K \approx 2.5$. Manes et al. (2011) systematically evaluated the effects of K with Re_K varying from 0 to 17. Within this range, the K-H instability and signature of the rollers were observed for $Re_K \approx 17$ and not for $Re_K \approx 8$, for example. The effects of interface roughness on K-H instability and the resulting coherent motions for flows with high Re_K are interesting questions for future work.

It should be noted that the specific configuration of the regular packing may also affect the drag, turbulent statistics and structure. For example, the hexagonal particle packing is expected to give more drag and higher resistance to the streamwise velocity fluctuations. We have run an additional DNS simulation with hexagonal arrangement at the interface (not shown herein) and compared various flow quantities with the cubic arrangement. It was observed that, though the hexagonal arrangement gave slightly higher C_f and anisotropy of the form-induced stresses, such differences were much smaller compared to the difference between the cubic and the random arrangements. The reason is probably due to the similar roughness length scales among various regular arrangements and the organized mean-velocity pattern (e.g. mean recirculation regions) they generate. For this reason, the cubic arrangement discussed in details herein is considered as a representative example of regular type of packing.

The results demonstrate that subtle details of the particle roughness alone, in the absence of bedform, can affect significantly the dynamics of the turbulence and the form-induced fluctuations.

Such effects translate to large differences in apparent permeability, hyperheic flux, and subsurface flow paths of passive scalars. Future work is needed to fully understand the effects of particle roughness on scalar and momentum transport with systematically varying roughness lengths (σ_h^+ , λ^+), roughness texture, as well as the effect of varying bulk permeability with random interface roughness.

CHAPTER 3

QUANTIFYING THE EFFECTS OF BED ROUGHNESS ON TRANSIT TIME DISTRIBUTIONS VIA DIRECT NUMERICAL SIMULATIONS OF TURBULENT HYPORHEIC EXCHANGE

3.1 Introduction

The pore-resolved direct numerical simulations (DNS) of interface turbulence carried out in Chapter 2 revealed that, even in the absence of bedforms, the grain-scale roughness of a macroscopically flat bed leads to significant fluid volumetric flux into the sediment. Also, statistics and structure of the turbulent flow were shown to depend on the texture of roughness. Similar observations were made for a macroscopically flat bed by Chandler et al. (2016), Grant et al. (2020a) and Kim and Kang (2020).

In this chapter, the work in Chapter 2 is expanded by documenting the effects of grain-scale roughness and its texture on macroscopic exchange quantities including the fluid volumetric flux into the sediment, subsurface flow paths, and transit time characteristics. The primary questions that will be addressed in this chapter include:

1. How does bed roughness on a macroscopically flat bed influence fluid parcel transit times?
2. How do TTDs change with tracer particle entry/exit locations within a three-dimensional flow field and with the inclusion of molecular diffusion?

To this end, turbulent open-channel flows bounded by synthesized sediment beds similar to those studied in Chapter 2 were simulated. Computed flows for two sediment beds that share the same bed permeabilities but have different bed roughness arrangements are compared. A forward particle tracking method is used to calculate the transit times, considering the mechanism of time-mean velocity advection with and without molecular diffusion. The paper is organized as follows. Section 3.2 describes the details of the DNS simulations, the sediment bed synthesis, and the method used to calculate transit times. Section 3.3 compares the transit time results for the

two cases examined and analyzes the effects of molecular diffusion, followed by conclusions in Section 3.4.

3.2 Methodology

3.2.1 Case configuration and parameters

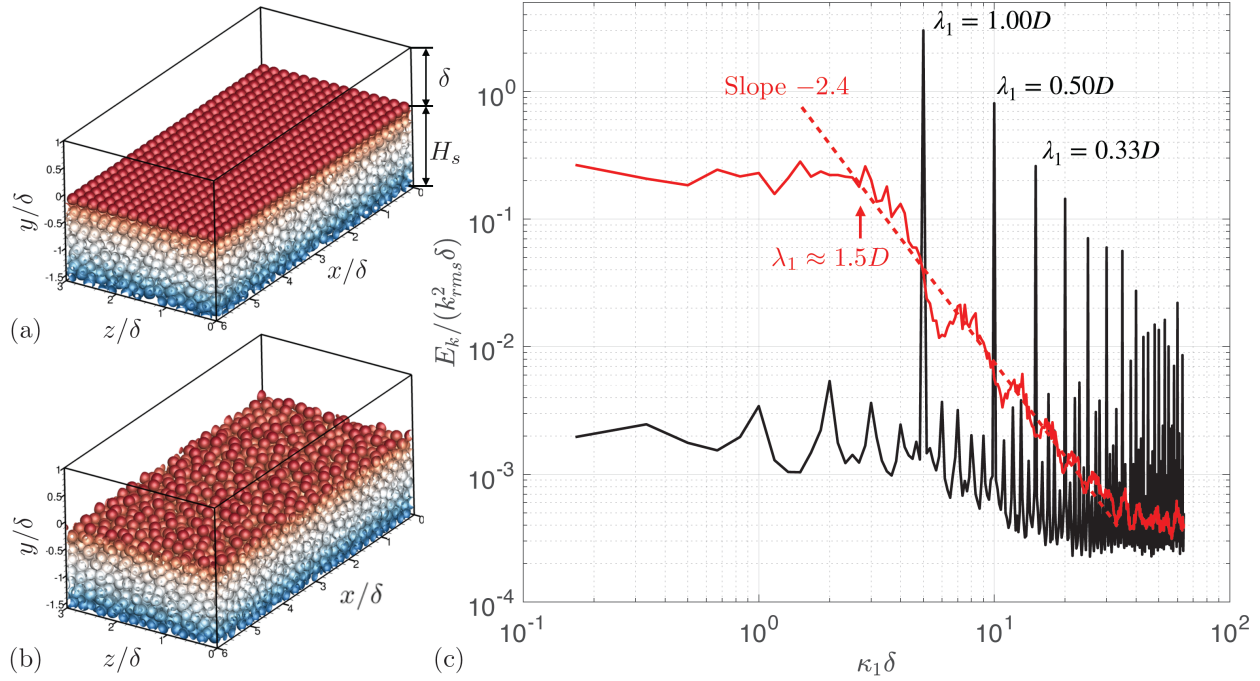


Figure 3.1: Simulation domain and synthesized sediment beds colored by y in (a) the regular and (b) the random cases. (c) One-dimensional power spectral densities E_k of the interface height fluctuations for Case 1 (regular case, —) and Case 2 (random case, —, red). --- (red) Slope of power-law decay for Case 2; k_{rms} is the root-mean-square (rms) of interface height fluctuations.

Fully developed open-channel flows are simulated using the same DNS method mentioned in previous Chapter. The simulation domain includes both the surface and sub-surface flows (Figure 3.1(a,b)). δ is the thickness of the turbulent boundary layer (i.e., open-channel height) measured from the sediment crest; H_s is the sediment depth measured from the crest to the bottom boundary of the simulation domain. Symmetric boundary conditions are applied at both top and bottom boundaries of the domain. Periodic conditions are applied at x and z boundaries. A constant mean pressure gradient is used to drive the flow. The elevation of $y = 0$ is set at the

	Interface	Re_K	Re_τ	D/δ	D^+	H_s/δ	$(L_x, L_z)/\delta$	$(\Delta x^+, \Delta y_{\min}^+, \Delta z^+)$
Case 1	Regular	2.62	395	0.20	79	1.6	(6, 3)	(1.5, 0.19, 1.5)
Case 2	Random	2.62	395	0.20	79	1.6	(6, 3)	(1.5, 0.19, 1.5)

Table 3.1: Summary of simulation parameters. D is the grain diameter; L_{x_i} is the simulation domain size in x_i . Δx^+ , Δy^+ , and Δz^+ are DNS grid sizes in x , y and z , respectively, normalized using the viscous length scale ν/u_τ .

virtual origin—an offset of the y axis such that the mean velocity profile in the overlap region of the turbulent flow recovers its logarithmic form. The elevation of the virtual origin was determined based on a fitting procedure (Breugem et al., 2006; Manes et al., 2011); it falls between $0.3D$ and $0.5D$ below the sediment crest, where D is the grain diameter.

The simulation parameters are listed in Table 3.1. Two cases are considered, one with a regular interface (Case 1) in which the arrangement of grains in the uppermost layer is regular and the other with random arrangement of grains (termed ‘random interface’, Case 2). In both cases, the same porosity of 0.41 is imposed in the sediment sufficiently far from the interface. The permeability Reynolds number and the friction Reynolds number are the same for both cases: $Re_K = \sqrt{K}u_\tau/\nu = 2.62$ (where K is the permeability) and $Re_\tau = \delta u_\tau/\nu = 395$. Following Voermans et al. (2017), u_τ is obtained from the maximum magnitude of the bed-normal profile of the total shear stress, which is the sum of the viscous shear stress, the Reynolds shear stress and the form-induced shear stress. The total numbers of grid points are 1536, 779 and 768 in x , y and z directions, respectively. The present DNS simulations are similar to the simulations reported by Shen et al. (2020). The only difference is that the sediment thickness herein is doubled ($H_s/\delta = 1.6$ versus 0.8 in Shen et al. (2020)), to allow for deeper subsurface flow paths, which are important for calculation of large transit times but less important for interfacial turbulence. The total simulation time used for data collection is around 10 large-eddy turn-over times (LETOTs), defined as δ/u_τ ; a LETOT represents the time scale of the evolution of the largest turbulent eddy in the open channel. Sufficiency of the data sampling in time was validated by comparing both surface and subsurface flow statistics, as well as TTDs, obtained with 10 LETOTs and those obtained with 20 LETOTs. The differences were small (e.g., up to 1% in subsurface dispersive velocities, $\langle \tilde{u}^2 \rangle^{1/2}$, as shown in

the Appendix B Figure B.4).

For both cases, the depths of the channel and the bed (both measured from the virtual origin) are 5 times and 8 times of the grain diameter, respectively. A boundary layer thickness of 5 times the grain size is much smaller than in many streams in reality and, consequently, the turbulence near the interface may not be identical to those in many real streams. However, the present setup is designed to represent streams for the regime with Re_K of $o(1)$ where the form-induced velocity is the main component of the subsurface fluid motion; the interfacial turbulence weakly affects the majority of the parcel transit times in comparison to the form-induced velocities. In addition, D/δ of the same order of magnitude were used in existing numerical and experimental studies that reported grain-scale physics (Manes et al., 2009; Dey and Das, 2012; Fang et al., 2018; Han et al., 2018; Voermans et al., 2017, 2018).

The porous sediment beds are modeled as closely packed monodisperse hard spheres. In the bulk of the sediment, the sphere positioning is determined based on molecular dynamics simulations (Plimpton, 1995) and is random for both cases. For the uppermost-layer spheres, two types of distributions are imposed, representing regular (Case 1) and random (Case 2) bed roughness geometries, respectively. The random case corresponds to significantly larger root-mean-square roughness height and longer horizontal correlation lengths. As these length scales are much smaller compared to δ and the scales typical of a bedform, the bed height variation is considered as roughness. Figures 3.1(a,b) compare the sphere distributions in Cases 1 and 2, showing the difference in grain arrangement at the top of the sediments. The sediment in Case 2 was constructed such that it yields turbulence statistics that match those observed for randomly poured spheres in the experimental studies of Voermans et al. (2017) (case L12 therein). Case 2 is thus considered as a good approximation of a realistic sediment.

To highlight the difference between the two roughness geometries, the one-dimensional (1D) power spectra of height fluctuations of uppermost-layer spheres (E_k) are compared in Figure 3.1(c) as functions of the streamwise wavenumber ($\kappa_1 = 1/\lambda_1$, where λ_1 is the streamwise wavelength). Both cases show a white noise regime at small wavenumbers, characterized by almost constant E_k .

Aubeneau et al. (2015) calculated the power spectra of elevations of sand beds produced in lab flume experiments under various discharges. They also observed a white noise region in the power spectrum for small wavenumbers. For the random case the white noise regime applies to λ_1/D larger than around 1.5. For smaller λ_1 , E_k shows a power-law decay with a slope of around -2.4 . From this power-law decay, a fractal dimension D_f can be identified as $D_f = E + (3 - \beta)/2 = 2.3$, where $\beta = 2.4$ is the fitted slope of the decay and $E = 2$ (for a 3D surface) is the Euclidean topological dimension. Aubeneau et al. (2015) also observed power-law decays at large wavenumbers, though with different slopes of -1.0 to -1.5 . In comparison, for the regular case the white noise region covers wavenumbers up to D . At larger wavenumbers E_k is characterized by higher-frequency harmonics, which is a mathematical consequence of the slight clipping (or flattening) at the top of the sphere surfaces that results from the spatial discretization of the sphere geometry. These observations show that the bed roughness of Case 2 is close to a self-affine fractal (similar to real sediment beds) while Case 1 is characterized by organized grain-wise protuberances.

3.2.2 Transit time calculation based on particle tracking

For an unsteady flow in general, the mass conservation equation for the storage of water of a certain age in the sediment is (Botter et al., 2011; Harman, 2015)

$$\frac{\partial S(t)p_S(\tau, t)}{\partial t} = -Q(t)\overleftarrow{p}_Q(\tau, t) - \frac{\partial S(t)p_S(\tau, t)}{\partial \tau}, \quad (3.1)$$

where $S(t)$ is the instantaneous total water storage in the sediment at time t , $Q(t)$ is the instantaneous flux at the outflow, $p_S(\tau, t)$ is the instantaneous RTD, defined as the probability density function (pdf) of the age (τ) of all the water parcels in the sediment at time t , and $\overleftarrow{p}_Q(\tau, t)$ is the backward TTD, defined as the probability that the age of a water parcel at the outflow at time t is equal to τ (Harman, 2015). The only assumption used in Equation (3.1) is that there is one inlet and one outlet of the system. In this study, the inlet is the collection of regions on the water-sediment interface where the bed-normal velocity (v) is negative, while the collection of regions where v is positive serves as the outlet. The water age is considered zero at the inlet.

Note that different definitions of RTD were used in the literature. For example, the cumulative distribution function of RTD was defined as the fraction of solute entering the sediment bed in a short time near $t = 0$ and exiting the bed by time τ (Grant et al., 2020b). The residence time function of EB97 is trivially different from this definition. In this article, however, the definitions of Harman (2015) are followed.

We consider fluid parcels advected by the three-dimensional, time-averaged velocity, \bar{u}_i . The advection by instantaneous turbulent fluctuations u'_i is not accounted for. This is because, at the present $Re_K = 2.6$, the magnitudes of normal Reynolds stress components are significantly smaller than those of the form-induced stresses in the sediment below the Brinkman layer, as shown by the DNS data of Shen et al. (2020) for the present cases. At a higher Re_K range, however, the effect of u'_i on the transit times is likely to be more important inside the sediment (Voermans et al., 2017). Kim et al. (2020) showed that at $Re_K = 50$ and $Re_\tau \approx 2,000$ significant turbulent motions in the bed—including downwelling and upwelling flows—occur and are modulated by large-scale turbulent motions in the surface flow. The present analyses, therefore, are relevant for the regime of $Re_K = o(1)$ only, where the interfacial turbulence is present but weak compared to dispersive velocities.

The consideration of the water parcels advected by the time mean velocity implies a steady state assumption for Equation (3.1), which becomes

$$Q \overleftarrow{P}_Q(\tau) + S \frac{\partial p_S(\tau)}{\partial \tau} = 0. \quad (3.2)$$

Equation (3.2) shows that the backward TTD and the RTD are related; one can be calculated from the other given known values of the outflow flux and water storage. In this work, we calculate $\overleftarrow{P}_Q(\tau)$ based on its definition. The discussion is focused on $\overleftarrow{P}_Q(\tau)$ and the corresponding cumulative distribution function, $\overleftarrow{P}_Q(\tau)$. The RTD can be calculated based on Equation 3.2; details are presented in the Appendix B.

In the present particle tracking approach, a fluid parcel is considered as a tracked particle. To calculate the transit time (or the maximum water age achieved by an individual parcel in the sediment), fluid parcels are traced starting from a y elevation near the interface throughout the

(x, z) plane. Only the fluid parcels entering the sediment (i.e., those released at locations where $\bar{v} < 0$) are tracked. The tracked paths are in general three-dimensional. The parcel position $x_i(t)$ at a time t (with $t = 0$ at the parcel release time) is tracked based on

$$\frac{dx_i}{dt} = \bar{u}_i[x_i(t)], \quad (3.3)$$

where t is a fictitious time used for particle tracking, not to be confused with the simulation time in DNS. Equation (3.3) is discretized and solved using the explicit Euler scheme. Once a subsurface travel path is determined, the transit time for the corresponding fluid parcel is calculated as the total time it spends along the subsurface path.

All tracked fluid parcels share the same release elevation (y_1) and the same ‘exit’ elevation (y_2). If $y_1 \leq y_2$, a parcel is considered to have left the sediment once it passes y_2 . If $y_1 > y_2$, the tracked parcel first goes downward, passing the y_2 elevation, and then upward toward the y_2 elevation; in this case, the exit is considered to occur when the parcel passes y_2 the second time. The periodic boundary conditions in x and z are used: parcels leaving the domain at boundary $x/\delta = 6$ reenters the domain at boundary $x/\delta = 0$, and vice versa, for up to twice of the domain lengths. Longer tracking lengths up to 4 times of the domain lengths in x and z were also tested, yielding similar transit time distributions. One particle is released at each computational grid point in the fluid domain at $y = y_1$. In total, around $o(10^6)$ particles are released. To test the result convergence, we used twice the number of released particles, which led to differences of less than 1% in the fitted TTD slope and the median transit time value. The cumulative backward TTD, $\overleftarrow{P}_Q(\tau)$, is calculated as the fraction of the number of tracked subsurface paths that correspond to transit times shorter than τ . $\overleftarrow{P}_Q(\tau)$ is then obtained as $d\overleftarrow{P}_Q/d\tau$. The calculated $\overleftarrow{P}_Q(\tau)$ is smoothed based on a moving averaging procedure. The size of the averaging window widens with the transit time value as approximately 0.1τ .

To validate the implementation of the particle tracking method, the computed residence time function as defined in EB97 is compared to the analytical solution for a subsurface flow induced by a 2D sinusoidal interface pressure distribution. Details of the validation are included in the Appendix B. The comparison shows that the particle-tracked residence time function matches

well with the analytical solution given a sufficiently fine spatial resolution and a sufficiently deep sediment domain (Figure B.2).

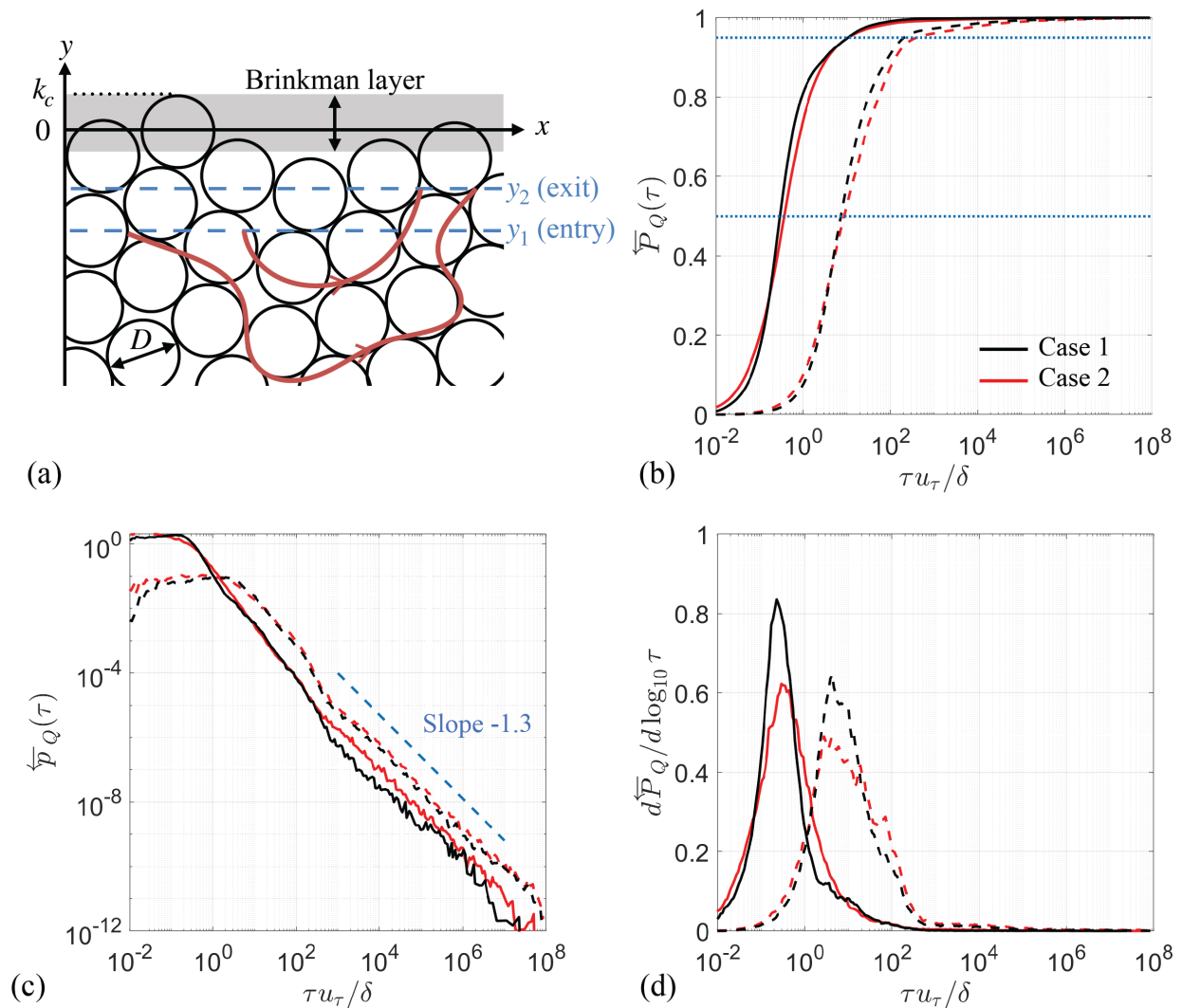


Figure 3.2: (a) Sketch of typical tracked flow paths for the random interface (Case 2). The cumulative backward transit time distribution (b) and its pdf (c) are shown for two sets of entry and exit locations: $y_1 = y_2 = 0$ (—) and $y_1 = y_2 = -3D$ (---) for the regular interface (black lines) and the random interface (red lines). (d) Modified pdf showing the probability density in evenly spaced logarithmic increments. In (b), the horizontal dashed lines (---, blue) mark the 50th (median) and 95th percentiles. In (c), the dashed blue lines (---, blue) show the fitted power law with slopes indicated.

In the analyses of EB97, detailed flow information around sediment grains is not available. The water column and the subsurface flow were delineated by a zero-thickness interface separating the surface flow and the subsurface flow where the Darcy model applies. In that context, a particle

tracking method for residence time calculation assumes that the release elevation (y_1) and exit elevation (y_2) of the tracked fluid parcels are both at the exact water-sediment interface. In the present DNS, there is a transition layer between the surface flow and the Darcy-flow region. This layer includes the roughness sublayer (Raupach et al., 1991)—a near-bed layer where form-induced stresses are important—and the Brinkman layer—the region of mean shear layer penetration, $\partial\langle\bar{u}\rangle/\partial y > 0$. Varying entry and exit elevations parcels are tested. Examples of tracked flow paths are sketched in Figure 3.2(a).

3.3 Results

3.3.1 Effect of bed roughness geometry on transit times

Figures 3.2(b) and 3.2(c) compare $\overleftarrow{P}_Q(\tau)$ and $\overleftarrow{p}_Q(\tau)$ with the same entry and exit elevations for two sets of values: $y_1 = y_2 = 0$ (near the sediment crest) and $y_1 = y_2 = -3D$ (a sufficiently deep elevation beyond which the median τ of the $\overleftarrow{p}_Q(\tau)$ distribution becomes largely independent of the entry and exit elevations for both cases, as shown later in Figure 3.5). The elevation $-3D$ is equivalent to -0.6δ . The transit times are normalized by the LETOT (δ/u_τ) of the open-channel turbulence, representative of the time scale of largest turbulent coherent motions in the water column. For large transit times stronger fluctuations of the TTD curves are seen in Figure 3.2(c), since the sampling of these long paths available from the DNS domain is extremely limited. The $\overleftarrow{p}_Q(\tau)$ distributions display power-law decays with a slope of around -1.3 at large transit times for both cases. The existence of a power-law tail indicates that the sediment domain in the DNS simulations is sufficiently large (in both x and y) to capture deeper flow paths, and is consistent with experimental observations by Aubeneau et al. (2015) and results of numerical simulations obtained by Lee et al. (2020) of exchanges induced by multiscale bed geometries. Note that, according to Equation (3.2), a power-law decay of the TTD (\overleftarrow{p}_Q) is associated with a power-law decay of the RTD (p_S), which is shown in Figure B.1 in the Appendix B. For both cases, a deeper entry elevation excludes shorter flow paths close to the surface and, consequently, increases the probability of longer paths. This is reflected by the shifting of the TTDs toward larger times in

(y_1, y_2)	Characteristic	Case 1 (A)	Case 2 (A)	Case 1 (MD)	Case 2 (MD)
(0, 0)	τ_{50}	0.294	0.368	0.467	0.574
(0, 0)	τ_{95}	10.6	10.6	110	80.0
$(-3D, -3D)$	τ_{50}	7.33	8.67	13.6	13.8
$(-3D, -3D)$	τ_{95}	205	393	8.35×10^5	2.17×10^6

Table 3.2: Various characteristics of transit times calculated based on mean advection only and both mean advection and molecular diffusion, at two elevations of particle entry (y_1) and exit (y_2). Transit times are normalized by δ/u_τ . Note. ‘A’ denotes calculation based on time-mean advection alone; ‘MD’ denotes calculation accounting for both time-mean advection and molecular diffusion (discussed in Section 3.3.3).

Figure 3.2(c) as y_1 and y_2 change from 0 to $-3D$. The change of entry and exit elevations does not significantly modify the slope of the power-law tail.

When the particle release location at 0 was used, the \overleftarrow{p}_Q distribution in the case with regular roughness displays a relatively sharp drop of probability for dimensionless τ at around 400. This is thought to be related to the organized fluid motions around the regularly arranged grains at the surface, leading to preferential values of τ associated with these short paths. A similar drop in probability is also evident at dimensionless τ of around 200 to 400 in both cases, when a particle release elevation of $-3D$ was used. This is because the algorithm tracks undulating segments of the large number of paths that reach not far beyond $y = -3D$ (visualized in Figures 3.3(e,f)). Lee et al. (2020) studied bed geometries synthesized with systematically varying spectral characteristics. They also observed variations in the slope of the RTD and suggested that they are connected to the flow recirculation regions induced by bed morphology.

An alternative approach to plot the transit time distribution, different from $\overleftarrow{p}_Q(\tau)$, is to divide the unit area under the curve into evenly spaced logarithmic increments of τ . This allows the actual probability density to be shown in a plot with a logarithmic τ axis. This distribution, shown in Figure 3.2(d), is defined as $d\overleftarrow{P}_Q/d \log_{10} \tau$ and is equivalent to $2.303\tau \overleftarrow{p}_Q$ (Grant et al., 2020b).

To quantitatively compare the TTDs, the 50th and 95th percentiles (denoted as τ_{50} and τ_{95} , respectively) of the \overleftarrow{p}_Q distributions are calculated. Specifically, τ_{50} represents the central tendency of the distribution, while τ_{95} is considered as a characteristic τ associated with the rare, long-transit-

time subsurface paths. Their values are tabulated in Table 3.2 under columns “Case 1 (A)” and “Case 2 (A)”. The comparison shows that the two cases give rather similar τ_{50} values (up to 10-20% different) for both elevations. For $y_1 = y_2 = -3D$, τ_{95} is significantly higher in Case 2 than in Case 1 (393 versus 205), due to longer and deeper reaching paths, which will be shown in Figure 3.3(g,h). An important conclusion that follows from this result is that the difference in bed roughness texture extends deep into the sediment and significantly modifies the transit time values.

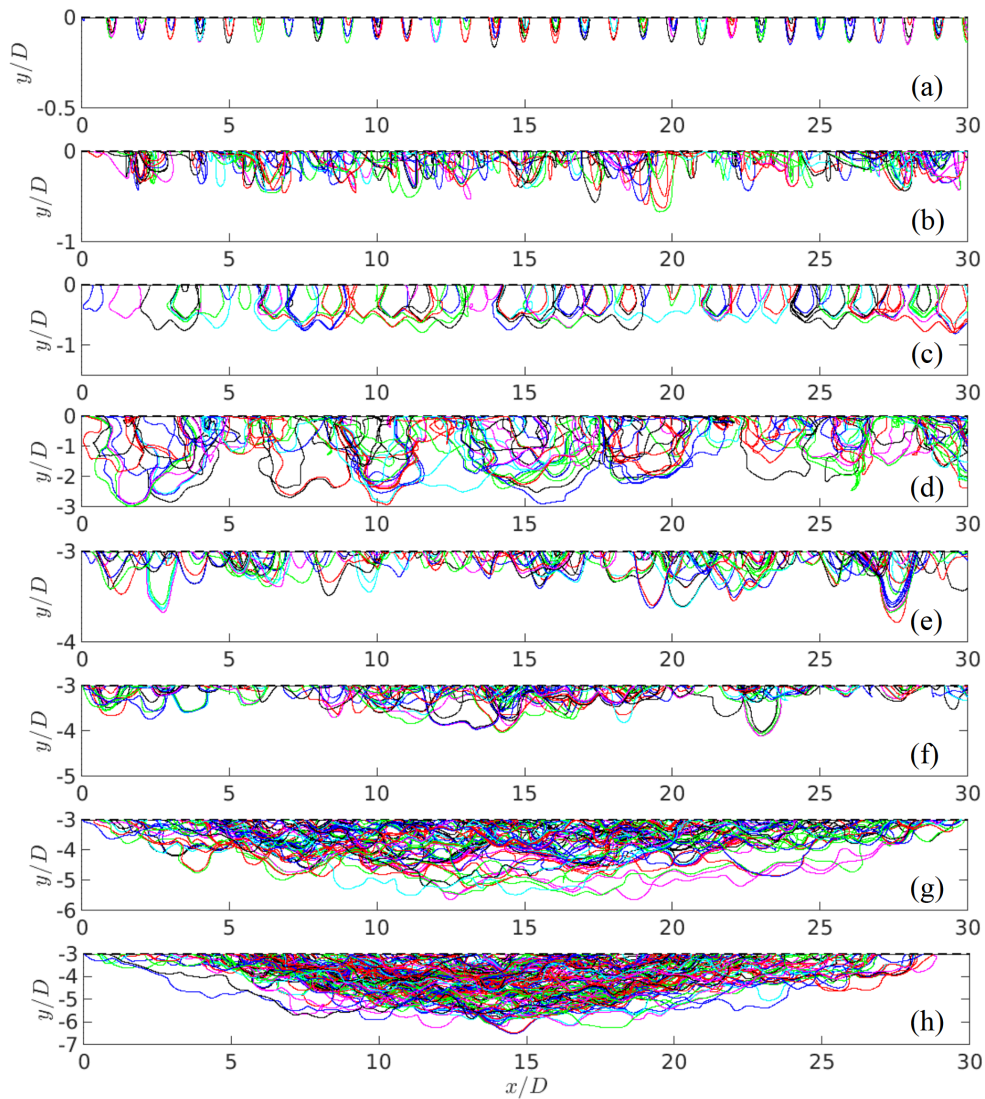


Figure 3.3: Time-mean subsurface flow paths corresponding to the median (50th-percentile) transit time (a,b,e,f) and the 95th-percentile transit time (c,d,g,h) for entry/exit elevations at $y_1 = y_2 = 0$ (a,b,c,d) and $y_1 = y_2 = -3D$ (e,f,g,h), for the regular (a,c,e,g) and random (b,d,f,h) interfaces.

To explain the differences in the TTD characteristics, Figure 3.3 shows tracked subsurface flow paths for $y_1 = y_2 = 0$ (a-d) and for $y_1 = y_2 = -3D$ (e-h) for both cases. Only the paths with travel times equal to τ_{50} and τ_{95} are plotted. In each subplot, around 200 pathlines are visualized. For both cases the paths associated with τ_{50} are short and do not reach beyond one grain diameter below y_1 . Those associated with τ_{95} , however, reach far deeper and are described as follows. For the regular interface, relatively uniform small-scale arc-shaped paths are observed (due to flows around regularly packed grains at the bed surface). For the random case the tracked paths are more complex, with short paths near the interface and also longer, deeper paths. As the transit time of a water parcel depends on the depth and the length of the flow path, τ_{95} in Case 2 is longer than that in Case 1. For paths at $y_1 = y_2 = -3D$, Case 1 also yields multiscale flow paths similar to those for Case 2, as the short paths near the interface for Case 1 are now excluded by the deeper entry elevation. The paths in Case 2 reach deeper into the sediment than for Case 1, leading to longer transit times. These observations indicate that the flow pattern throughout the bed is dependent on the roughness characteristics.

In Figure 3.3, nearly all of the flow paths are oriented downstream in x . Exceptions are the flow paths located in the lower portion of the recirculation regions near the interface, where the flow is directed upstream. The very high fraction of subsurface flow paths oriented downstream is a major difference from flow paths induced by bedforms, such as those induced by triangular bedforms in the experimental study of Elliott and Brooks (1997a), where a significant fraction of large-scale upstream-oriented subsurface flow paths were found. This difference is probably due to the negligible hydrostatic pressure variations along the interface in the present cases as the roughness height is much lower than the open-channel height.

To characterize the velocity along the subsurface flow paths, Figure 3.4 compares the wall-normal velocity magnitudes ($|\bar{v}|$) that are conditionally averaged along the down- and up-going portions of the flow paths, respectively. The result is a function of y and the bed-normal flow path direction. Flow paths tracked with $y_1 = y_2 = 0$ are used. At a given y near the interface, $|\bar{v}|$ for the random case is much larger than the value for the regular case. This is consistent with the deeper

flow paths for the former (Figure 3.3(d)) than for the latter (Figure 3.3(c)). In addition, for both cases the speed of downward flow is higher compared to that of upward flow. This difference has an impact on the transit time values when the entry elevation differs from the exit one.

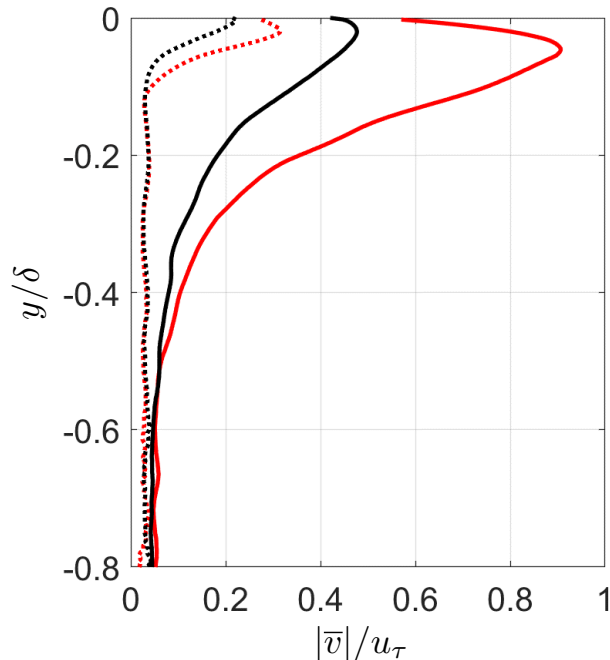


Figure 3.4: Wall-normal variation of \bar{v} magnitude conditionally averaged along downward (red) or upward (black) flow paths tracked at $y_1 = y_2 = 0$, for regular (---) and random (—) cases.

Next, independent variations of entry (y_1) and exit (y_2) elevations are studied. Both y_1 and y_2 are varied between the sediment crest and $y/\delta = -0.9$. An ensemble of particle-tracking simulations based on 42 values each of y_1 and y_2 (total 1764) was carried out. For each (y_1, y_2) pair, τ_{50} is calculated and plotted in a map shown in Figure 3.5. The variation of τ_{95} was also evaluated and a similar comparison was observed; the τ_{95} plots are shown in the Appendix B Figure B.5.

First, focus on the diagonal line represented by $y_1 = y_2$. The short transit times of $o(1)\delta/u_\tau$ at $y_1 = y_2 \approx 0$ are mostly due to mild undulations of subsurface paths (Figure 3.3a,b). For sufficiently deep entry/exit elevations, τ_{50} plateaus to values of $o(10)\delta/u_\tau$. The dependence of transit times on the entry and exit elevations of particles is not restricted to elevation variation within the Brinkman layer, which corresponds approximately to $y/\delta \in (-0.1, 0.1)$. Beyond this layer, deeper entry or exit elevations will still result in progressively longer transit times due to progressive exclusion of

shorter flow paths, until only long flow paths remain.

Next, small values of $|y_1 - y_2|$ produce short transit times due to a large fraction of tracked paths being associated with short flow paths that do not extend far beyond the elevation of y_1 , while with large $|y_1 - y_2|$ differences a larger fraction of the tracked paths are longer and deep-reaching ones, which yields much longer transit times. The regions above the diagonal line (i.e., $y_1 > y_2$) and below the line (i.e., $y_1 < y_2$) are not symmetric. The median transit times with y_1 below y_2 are larger than those with y_1 above y_2 at the same $|y_1 - y_2|$ difference. This is because the downward motion of a fluid parcel in the bed is, on average, faster than the upward motion, as shown in Figure 3.4. One also observes that the median transit times with $y_1 > y_2$ are less well-converged statistically than those with $y_1 < y_2$, as shown by the more fluctuating contour lines. This is due to the fewer flow paths used for averaging when $y_1 > y_2$ in the current computation procedure (see Appendix B Figure B.3). At large y_1 - y_2 separations, much longer transit times are observed for the regular case compared to the random one. This difference is probably a result of the significantly smaller magnitude of bed-normal velocity along flow paths in the regular case for $y/\delta > -0.5$

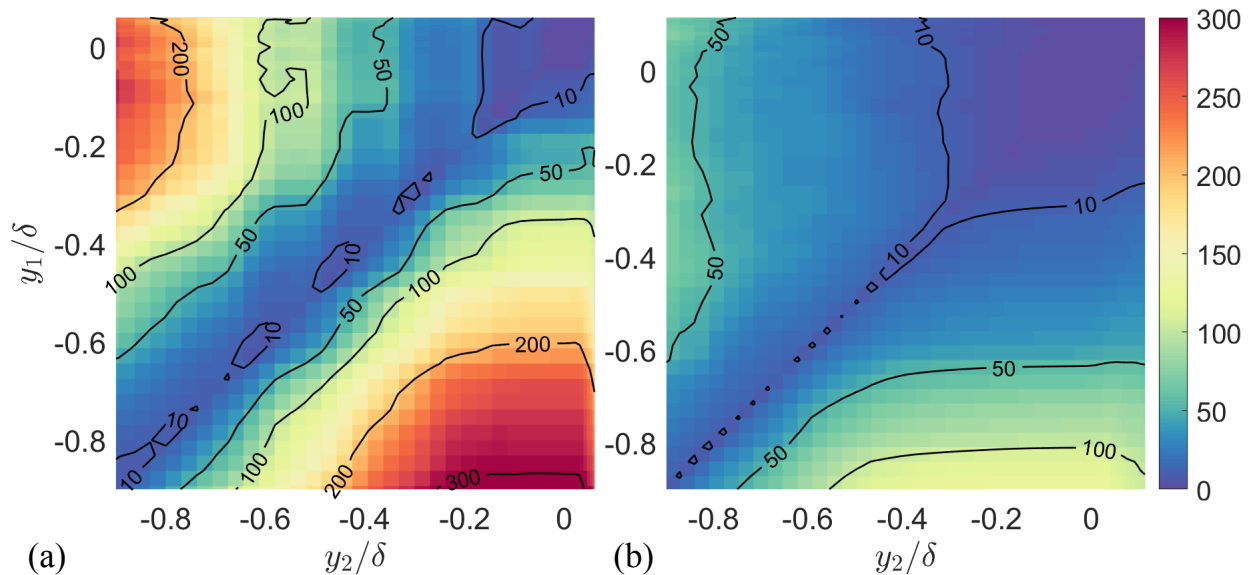


Figure 3.5: Median transit time normalized by δ/u_τ with independent variations of y_1 (entry) and y_2 (exit) elevations, for regular (a) and random (b) cases. Similar variations of τ_{95} are shown in the Appendix B Figure B.5.

(Figure 3.4).

These results highlight the fact that subsurface flow paths are multiscale in nature and typically extend deeper beyond the Brinkman layer. They also show that both the entry and exit elevations are important parameters in measuring and reporting transit times in the presence of bed roughness; however, these details are not often presented in the literature. The roughness geometry affects not only the transit time when y_1 is set equal to y_2 , but also the dependence of transit time on y_1 and y_2 when $y_1 \neq y_2$.

In the next two sections we address the following questions: (1) What factors determine the (x, z) locations of the entries and exits of subsurface flow paths (and consequently TTD characteristics)? (2) How important is the molecular diffusion for solute transit time?

3.3.2 Interfacial \bar{v} distribution

Figure 3.6 shows the typical flow pattern around a roughness protuberance formed as a grain cluster. A stagnation point appears upstream of the protuberance, leading to a region with local \bar{P} higher than the spatial average (indicated by $\tilde{P} > 0$). In addition, a recirculation region appears downstream, leading to a local low- \bar{P} region (indicated by $\tilde{P} < 0$). Such interfacial pressure

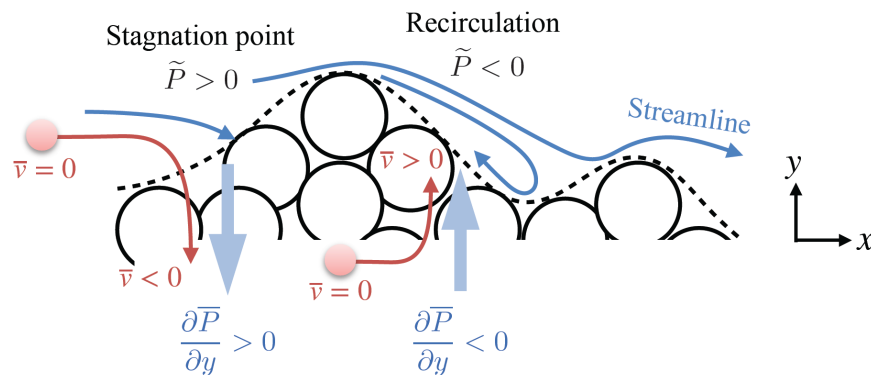


Figure 3.6: Sketch showing how local high-pressure (stagnation point) and low-pressure (recirculation) regions lead to entry and exit of fluid parcels (red spheres and red lines), specifically, in Case 2. --- Roughness geometry. $\bar{P}(x, y, z)$ and $\bar{v}(x, y, z)$ are the time-averaged values of pressure and wall-normal velocity; $\tilde{P}(x, y, z) = \bar{P}(x, y, z) - \langle \bar{P} \rangle(y)$ is the form-induced pressure, i.e., deviations from the plane-averaged value.

variation is in line with the description of local pressure variation on a bedform (triangular dune) by Savant et al. (1987). These local pressure maxima and minima lead to bed-normal pressure gradients at the bed surface: $\partial\bar{P}/\partial y > 0$ upstream and $\partial\bar{P}/\partial y < 0$ downstream.

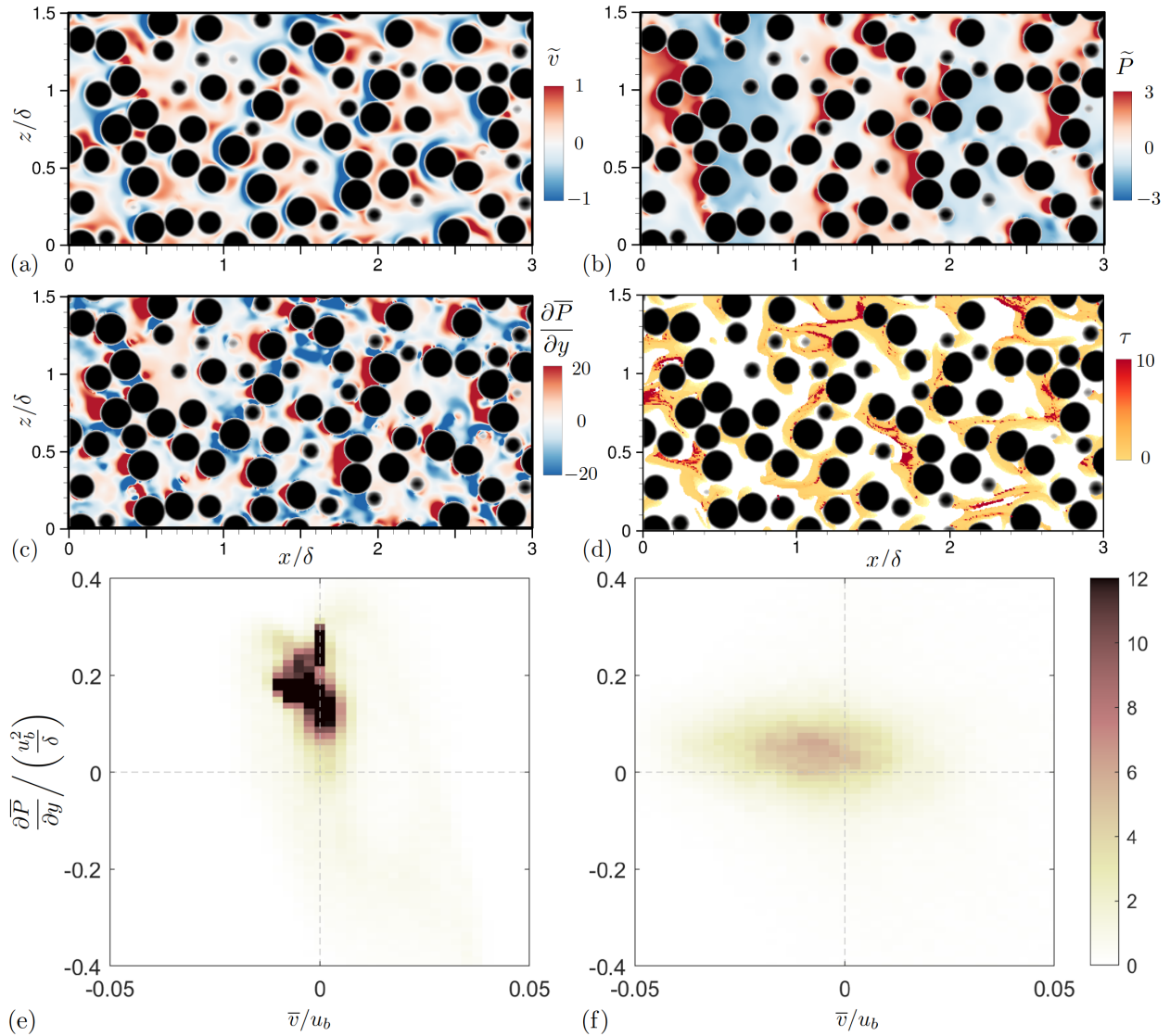


Figure 3.7: Bed-parallel contours for the random interface (Case 2) at $y = 0$: (a) bed-normal mean velocity, (b) form-induced pressure, (c) bed-normal gradient of mean pressure, and (d) transit time of flow paths entering at each location. Only 1/4 of the domain is shown. All quantities in (a-d) are normalized by δ and u_τ . Joint probability density functions of $\partial\bar{P}/\partial y$ and \bar{v} in the interface region, for Case 1 (e) and Case 2 (f).

The bed-normal mean momentum equation near the interface connects the pressure gradients

to the entry and exit of subsurface flow paths:

$$\frac{\overline{D\bar{v}}}{\overline{Dt}} \equiv \frac{\partial \bar{v}}{\partial t} + \bar{u}_i \frac{\partial \bar{v}}{\partial x_i} = -\frac{1}{\rho} \frac{\partial \bar{P}}{\partial y} - \frac{\partial \overline{u'_i v'}}{\partial x_i} + \nu \frac{\partial^2 \bar{v}}{\partial x_i \partial x_i}, \quad (3.4)$$

where $\overline{D\bar{v}}/\overline{Dt}$ is the material derivative of \bar{v} advected by the time-mean flow, and the three terms on the right-hand-side represent forces due to, respectively, time-mean pressure, Reynolds stress and viscous stress. Equation (3.4) describes how various factors (on the right-hand-side) affect the time-mean v velocity of a fluid parcel. It is hypothesized that the local pressure gradient (the first term on the right-hand-side of (3.4)) is the main factor in determining the entry ($\bar{v} < 0$) and exit ($\bar{v} > 0$) locations of subsurface flow paths. Specifically, a positive $\partial \bar{P}/\partial y$ upstream of the obstacle would lead to negative \bar{v} values (entries of flow paths) for a fluid parcel initially with $\bar{v} = 0$, while a negative $\partial \bar{P}/\partial y$ downstream would lead to exits of flow paths. Such mechanism is sketched in Figure 3.6. This hypothesis is to be validated next.

Figures 3.7(a-d) compare contours of \bar{v} , \bar{P} , and $\partial \bar{P}/\partial y$ in a bed-parallel plane at $y = 0$ for the random case. The correlation between positive- \bar{P} regions, positive y -gradients of pressure, and negative \bar{v} values (entries), is apparent. These regions are typically seen upstream of clusters of grains serving as roughness protuberances. Similarly, downstream of these protuberances, one typically observes low pressure values, negative pressure gradients, and positive \bar{v} (exits). Figure 3.7(d) shows the contour of transit time of flow paths entering the subsurface from this plane. Regions with the highest pressure values are seen to generate the longest transit times.

The local correlation between \bar{v} and the bed-normal pressure gradients is better demonstrated using contours of their joint probability density function (jpdf) in Figures 3.7(e,f) for the two cases, respectively. Since the local y -gradient of \bar{P} varies significantly in y between the crest elevation and the bottom of the Brinkman layer, here the jpdf value for each $\partial \bar{P}/\partial y$ and \bar{v} combination is calculated at every y grid point in the region bounded by these two elevations and then averaged. The jpdf values shown in Figure 3.7(e,f) are normalized such that the area integral in each of these two plots is one. Both quantities are normalized by δ and the bulk velocity (u_b) in the water column; u_b is calculated as $1/\delta \int_0^\delta \langle \bar{u} \rangle dy$. Here u_b instead of u_τ is used for normalization to highlight the effect of roughness geometry. For both cases, the vertical pressure gradients are

indeed negatively correlated with the vertical flux. Comparing the two cases, the random case displays much wider distribution of \bar{v} and narrower distribution of y -gradient of pressure. This means that \bar{v} is more sensitive in this case to changes in $\partial\bar{P}/\partial y$, probably because of the higher effective permeability near the interface than for the regular case (Shen et al., 2020). Notice also that in both cases the magnitude of $\bar{v} < 0$ reaches much higher values than the magnitude of $\bar{v} > 0$, again indicating faster fluid parcel entry into the bed than exit from the bed.

Figure 3.7 indicates that, for both cases, the interfacial pressure distribution is closely correlated with local \bar{v} and therefore is probably the driving force of \bar{v} transport near the interface. Forces of the Reynolds and viscous stresses play secondary roles. In other words, the differences in transit time characteristics between Cases 1 and 2 are probably due to the different interfacial pressure distributions caused by the roughness geometries obstructing the surface flow in different ways.

3.3.3 Effect of molecular diffusion on TTD

The transit time calculation using Equation (3.3) considers the movement of a fluid parcel. On the other hand, the transit time of a solute is affected also by molecular diffusion. An exact estimation of the solute transit time would require tracking either the instantaneous location of a tracer particle (during the DNS simulation) or the concentration variation which yields a breakthrough curve. These tasks are beyond the scope of the present work. An alternative approach is to use the random walk method (Kinzelbach, 1988) to incorporate the effect of molecular diffusion into Equation (3.3) and this approach is used here.

The random walk particle tracking is based on a set of stochastic differential equations. Following Sun et al. (2015) who carried out pore-scale random walk particle tracking for a 3D domain, we solve

$$x_i(t + \Delta t) = x_i(t) + \bar{u}_i(x_i, t)\Delta t + r_i\sqrt{2D_m\Delta t}, \quad (3.5)$$

where Δt is a small time differential, r_i is a random number of standard Gaussian distribution with unit variance and zero mean, and D_m is the molecular diffusion coefficient. Equation (3.5) is a generalization of Equation (3.3). Compared to the approach of Kinzelbach (1988), here the

dispersion terms are ignored by setting the longitudinal and transverse dispersivity lengths to zeros. This is because the DNS resolves the time-mean flow details. Note also that the diffusion due to the turbulent velocities u'_i is assumed to be much smaller than that due to \tilde{u}_i because of much weaker Reynolds stresses compared to the dispersive stresses below the interface. The smoothness of the results of Equation (3.5) requires the step of particle advection to be a fraction of the grid cell size; Kinzelbach (1988) recommended five to ten steps per cell. Here, the Δt value corresponds to five steps per grid cell at a convection velocity of $\langle \bar{u} \rangle$ below the Brinkman layer. $D_m/u_\tau \delta$ takes a value of 2.5×10^{-6} to achieve a Schmidt number ($Sc = \nu/D_m$) of around 1000, representative of dissolved oxygen in water.

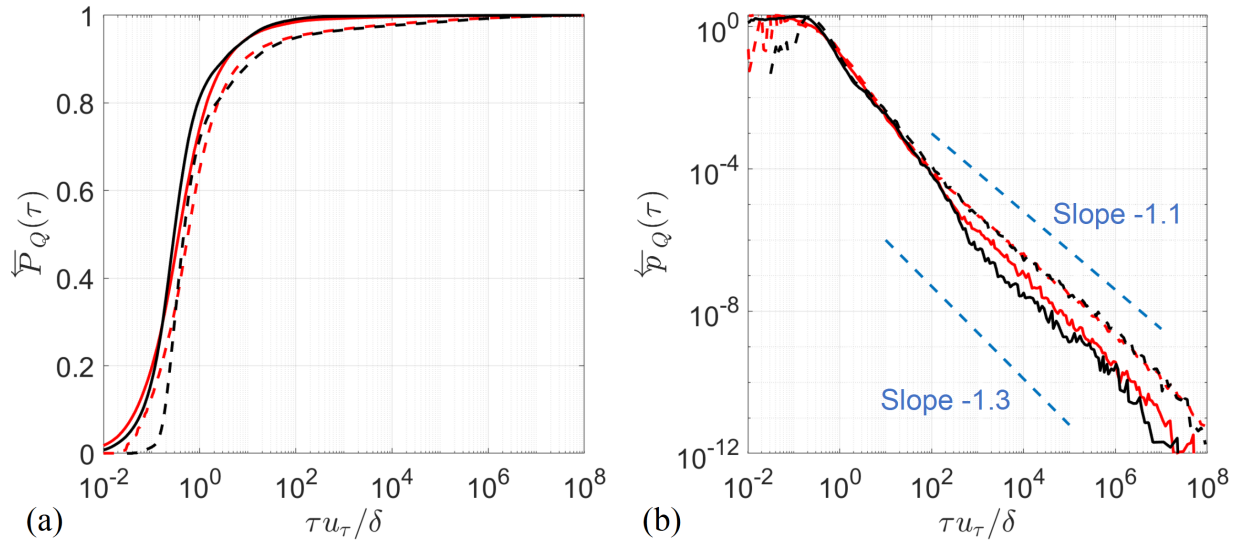


Figure 3.8: Cumulative backward transit time distribution (a) and its pdf (b) based on mean advection only (—) and based on both mean advection and molecular diffusion (---), for Case 1 (black) and Case 2 (red) at $y_1 = y_2 = 0$. In (b), --- (blue) shows the fitted power law with slope indicated.

The backward TTD and its cumulative distribution are shown in Figure 3.8 for $y_1 = y_2 = 0$. Various TTD characteristics are tabulated in Table 3.2 under columns “Case 1 (MD)” and “Case 2 (MD)”. The TTD power-law decay slope is milder for both cases, with the slope of around -1.1 , compared to -1.3 considering advection only. Changing to a deeper elevation, such as $y_1 = y_2 = -3D$, does not affect the power-law slope. For both cases, the addition of molecular

diffusion increases significantly the probability of transit times being longer than $o(10^2)\delta/u_\tau$, while early time values are only slightly affected. This increase in transit times is attributed to the fact that solute particles are displaced from the time-mean paths by molecular diffusion, resulting in paths with greater lengths. The addition of molecular diffusion does not remove the difference brought by a change in the roughness geometry. For a particle release elevation below the interface region (i.e. $y_1 = y_2 = -3D$) which tracks a large fraction of deep subsurface paths, τ_{95} normalized by δ/u_τ is significantly longer in Case 2 (2.17×10^6) than in Case 1 (8.35×10^5).

For a 2D sinusoidal bedform analyzed using an advection-dispersion model, Bottacin-Busolin and Marion (2010) also observed a milder slope (-0.5) of the residence time function when both mean advection and mechanical dispersion were accounted for, compared to the slope with advection only (-1.0). According to Equation (3.2) and the as shown in the Appendix B, the present slopes of \overleftarrow{p}_Q shown in Figure 3.8(b) indicate power-law decay slopes of -0.1 and -0.3 of the same residence time function, with or without molecular diffusion, respectively. The difference between the slopes observed herein and those in the study of Bottacin-Busolin and Marion (2010) is possibly due to the three-dimensionality of the present flow and the capability of DNS in capturing the actual velocities near the interface and within the bed.

3.4 Conclusions

Results of transit times are reported for turbulent open-channel flows over flat sediment beds at $Re_K = 2.6$ with two different bed roughnesses consisting of either regularly (Case 1) or randomly (Case 2) positioned sediment grains at the bed surface. The transit time calculations are based on DNS simulations similar to the ones reported in Shen et al. (2020). The transit times are calculated using the particle tracking method, considering (i) advection by time-mean velocity only and (ii) both time-mean advection and molecular diffusion.

Despite the absence of bedforms, both bed roughnesses generated a large spectrum of transit times, whose characteristics are similar to those generated by bedforms. The TTDs show power-law tails at late times for both cases; the time range and slope of the tail vary only weakly with the

roughness geometry. For both cases, the power-law slopes range from -1.3 considering the mean advection only, and around -1.1 considering both the mean advection and the molecular diffusion. We also show that, with pore-resolved data, the definition of a surface-subsurface interface becomes obscure; the calculated transit times vary with the elevations chosen to mark the ‘entry’ or ‘exit’ of particles.

Near the interface, roughness leads to regions with local pressure maxima or minima due to its effect on the near-bed turbulence. These regions are found to correlate closely with the distribution of interfacial bed-normal velocity. This suggests that locations of subsurface flow path entries and exits are mainly determined by the interfacial pressure, while being less sensitive to forces due to the Reynolds and viscous stresses. In other words, the advective pumping mechanism may be used to describe the subsurface flow induced by roughness on a macroscopically flat bed, similar to those induced by bedforms.

Compared to the regular roughness, the random roughness leads to longer transit times in the TTD power-law tail associated with deep subsurface pathlines. Specifically, the pure-advection particle tracking in Case 2 yields 18% and 91% larger transit times of the 50th and the 95th percentiles, respectively, than in Case 1 when $y_1 = y_2 = -3D$. This difference occurs because the random roughness induces more intense interfacial pressure variation (due to grain clusters forming protuberances larger than a single grain), with a wider range of horizontal length scales. Consequently, the subsurface flow paths in Case 2 can reach farther and deeper than in Case 1. With the addition of molecular diffusion in the transit time calculation, the transit time increases (especially at late times) for both cases, as expected. The differences between the two cases remain significant.

This work demonstrates that grain-scale roughness and its geometry are important for hyporheic exchange, as shown by the subsurface flow characteristics and transit times. The effect appears to be fundamentally similar to how a larger-scale bedform affects the exchange. These findings would not have been possible if a pore-unresolved simulation model (such as the Darcy flow model) was used instead. In addition, DNS data similar to the present data can be used for closure developments,

such as the parameterization of advection due to \tilde{u}_i and u'_i in TTD or RTD prediction based on a Darcy flow. Additional factors that are likely to affect the overall transit time of solutes include (i) grain-scale solute concentration variation near the bed surface and (ii) turbulent diffusion, which is strong in the Brinkman layer and is likely to affect τ values calculated with y_1 or y_2 close to 0. The importance of these factors and their dependence on roughness details need to be addressed in future work. In addition, scenarios that include both roughness and bedforms need to be explored for possible interactions between the effects of the two.

CHAPTER 4

PORE-RESOLVED DIRECT NUMERICAL SIMULATIONS OF HYPORHEIC EXCHANGE INDUCED BY BEDFORMS AND BED ROUGHNESS

4.1 Introduction

Bedforms are the most important source of flow resistance at the local scale in river channels. The word “Bedform” are used herein refers to ripples or dunes as described by Vanoni (2006). In sand-bedded rivers, form resistance is primarily generated by bedforms. The turbulent motions and flow separation generated by bedforms are responsible for transfer of mean flow energy to turbulent kinetic energy (Venditti, 2013).

The objective of this Chapter is to identify to what extent the grain-scale bed roughness affects the hyporheic exchange with the presence of bedform. To this end, pore-resolved DNS simulations of turbulent half-channel flows bounded by the same permeable dune-shape bedform with two different bed roughnesses are carried out and compared. The effects of grain-scale roughness and its texture on macroscopic exchange quantities including the subsurface flow paths and transit time characteristics are documented. A forward particle tracking method is used to calculate the transit times, considering the advection by time-mean velocity only, same as in Chapter 3.

The chapter is organized as follows. Section 4.2 describes the numerical techniques used for DNS and transit time calculation, the problem set-up, and the syntheses of bedforms with two different roughnesses superimposed on them. Section 4.3 compares the effects of bed roughness geometry on velocities, pressure field and transit times for the two cases examined and analyzes the effects of roughness with the presence of bedform, followed by conclusions in Section 4.4.

4.2 Methodology

4.2.1 Configurations and parameters

Fully developed open-channel flows are simulated using the same DNS method mentioned in previous chapters. The simulation domain includes both the surface and sub-surface flows (Figure 4.1(a,b)). δ is the thickness of the turbulent boundary layer (i.e., open-channel height) measured from the trough of the bedform; H_s is the sediment depth measured from the bedform trough to the bottom boundary of the simulation domain. H is the bedform height measured from its trough to its crest. The bedform wavelength is denoted by λ . The x location of the crest is $L_c = \lambda/2$. Symmetric boundary conditions are applied at both top and bottom boundaries of the simulation domain. Periodic conditions are applied at x and z boundaries. A constant mean pressure gradient is used to drive the flow. The elevation of $y = 0$ is set at the bedform trough elevation. The same double-averaging (DA) decomposition of an instantaneous flow variable as that used in previous

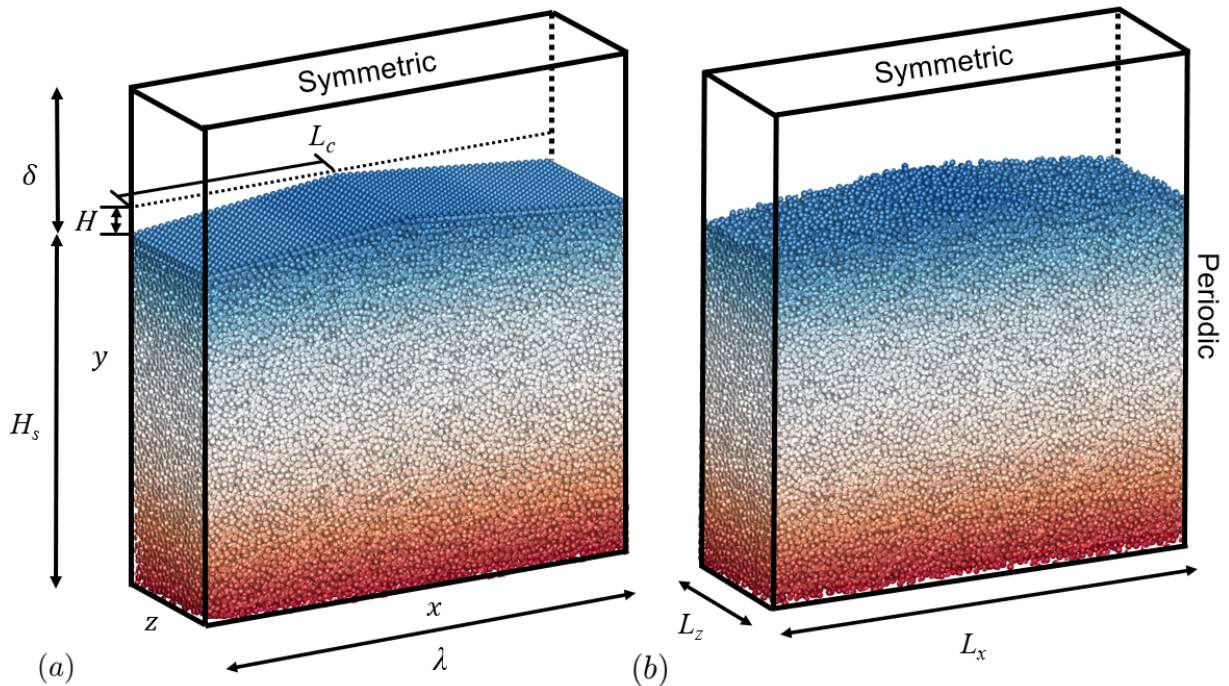


Figure 4.1: Simulation domain and synthesized bedforms with (a) regular and (b) random roughnesses, colored by y .

	Roughness	D/δ	H_s/δ	H/δ	λ/δ	L_c/λ	$(L_x, L_z)/\delta$	$(\Delta x^+, \Delta y_{\min}^+, \Delta z^+)$
Case 1	Regular	0.05	2	0.15	3	0.5	(3, 1)	(3.7, 0.3, 4.1)
Case 2	Random	0.05	2	0.15	3	0.5	(3, 1)	(3.7, 0.3, 4.1)

Table 4.1: Summary of parameters. D is the grain diameter; L_{x_i} is the simulation domain size in x_i ; $Re_K = 2.5$, $Re_\tau = 1580$, $D^+ = 79$. Δx^+ , Δy^+ , and Δz^+ are DNS grid sizes in x , y and z , respectively, normalized using the viscous length scale ν/u_τ .

chapters are applied. Given the streamwise dependence of this flow, a modified double-averaging decomposition is used, with the spatial averaging performed in z only, instead of averaging in both x and z as in the previous chapters.

The simulation and case parameters are listed in Table 4.1. Two cases are considered, one with regular roughness (Case 1) in which the arrangement of grains in the uppermost layer is regular and the other with random arrangements of uppermost-layer grains (Case 2). In both cases, the same porosity of 0.4 is imposed in the bulk of the sediment. The friction Reynolds number and permeability Reynolds number are the same for both cases: $Re_\tau = \delta u_\tau/\nu = 1580$ and $Re_K = \sqrt{K}u_\tau/\nu = 2.5$, where K is the permeability. The Re_K is the same as that used in previous chapters. The grain diameter in wall units is $D^+ = 79$. u_τ is obtained as the average of the local u_τ , calculated from the maximum magnitude of the local y profile of the total shear stress, which is the sum of the viscous shear stress, the Reynolds shear stress and the form-induced shear stress. The number of grid points are 1280, 1147 and 384 in x , y and z , respectively. The total simulation time used for data collection is around 10 large-eddy turn-over times (LETOTs), defined as δ/u_τ .

The porous bedforms are immobile and modeled as closely packed mono-disperse hard spheres. The locations of the grains are determined based on molecular dynamics simulations (Plimpton, 1995; Shen et al., 2020). Two bedforms with the same macroscopic dune geometry but different roughnesses at the uppermost layer are synthesized and shown in Figure 4.1. One is the “regular” case (Case 1) formed by regular distribution in (x, z) of grains and the other is the “random” case (Case 2) formed by random grain distribution of grains in both (x, z) and y . Both roughnesses are statistically similar to those imposed on a flat bed in the previous chapters. Below the bed surface, the grain distribution is random in both cases.

Figures 4.2 compares the bed surfaces in Cases 1 and 2, showing the difference in grain arrangement at the top of the bedform.

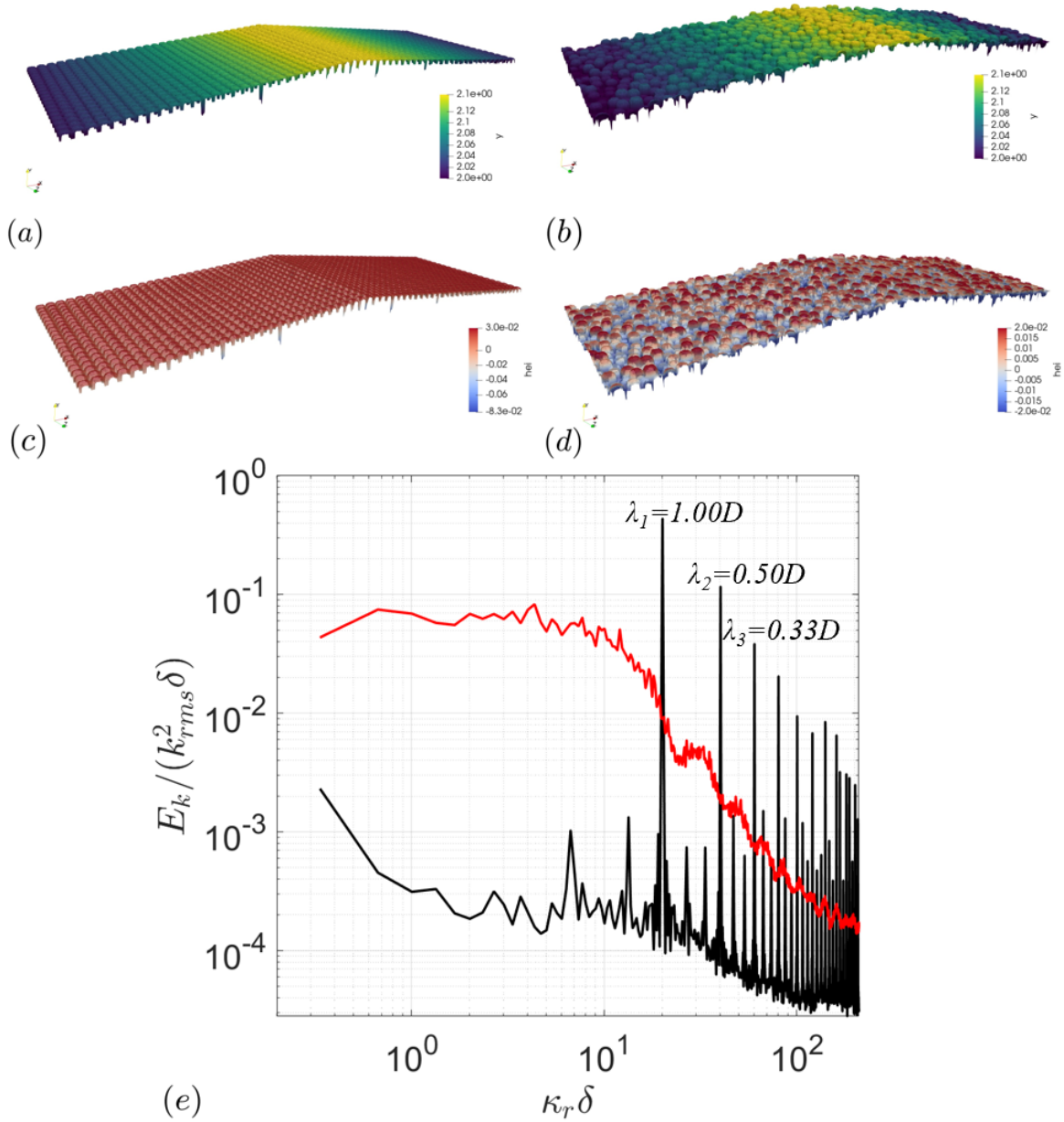


Figure 4.2: Roughness surfaces colored by y (a,b) and local height fluctuations measured from the bedform surface (c,d) in Cases 1 (a,c) and Case 2 (b,d). (e) One-dimensional power spectral densities E_k of the local height fluctuations for Case 1 (regular roughness, —) and Case 2 (random roughness, —, red). k_{rms} is the root-mean-square (rms) of interface height fluctuations.

To quantify the difference between the two roughness geometries, the one dimensional (1D)

power spectra (E_k) of local height fluctuations measured from the bedform surface are compared in Figure 4.2(e) as functions of the streamwise wavenumber ($\kappa_1 = 1/\lambda_1$, where λ_1 is the streamwise wavelength). Similar spectral distributions as those seen in Chapter 3 are observed here, expectedly. For the random case the white noise regime applies to λ_1/D larger than around 2.0. For smaller λ_1 , E_k shows a power-law decay with a slope of around -2.4 , which is the same as shown in Chapter 2. In comparison, for the regular roughness the white noise region covers wavenumbers up to D .

4.2.2 Transit time calculation based on particle tracking

The same definition and calculation of transit times are used as in Chapter 3 and are not repeated here. The only difference is the particle release and exit locations. Different from a constant height elevation for particle enter and exit used in Chapter 3, here we release particles on the streamwise-varying bedform interface and track particles until they exit from the interface, as shown in Fig. 4.3. Particles residing in the sediment without exiting or particles exiting the sediment elsewhere other than the interface are not accounted for in the transit time calculation. The particles are seeded uniformly on the bedform surface. In total, around $o(10^6)$ particles are released. To test the result

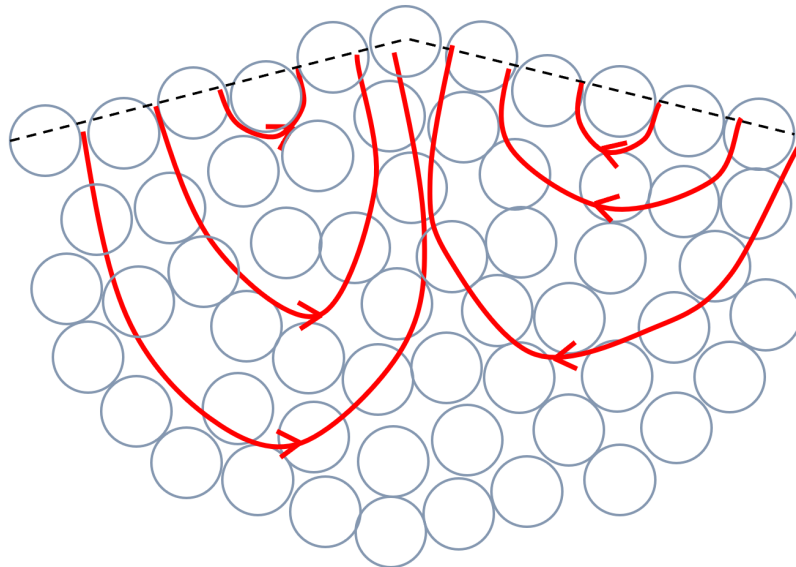


Figure 4.3: Conceptual sketch to show the enter and exit locations of tracked particles.

convergence, we used twice the number of released particles, which led to less than 1% difference in the fitted TTD slope or the median transit time value.

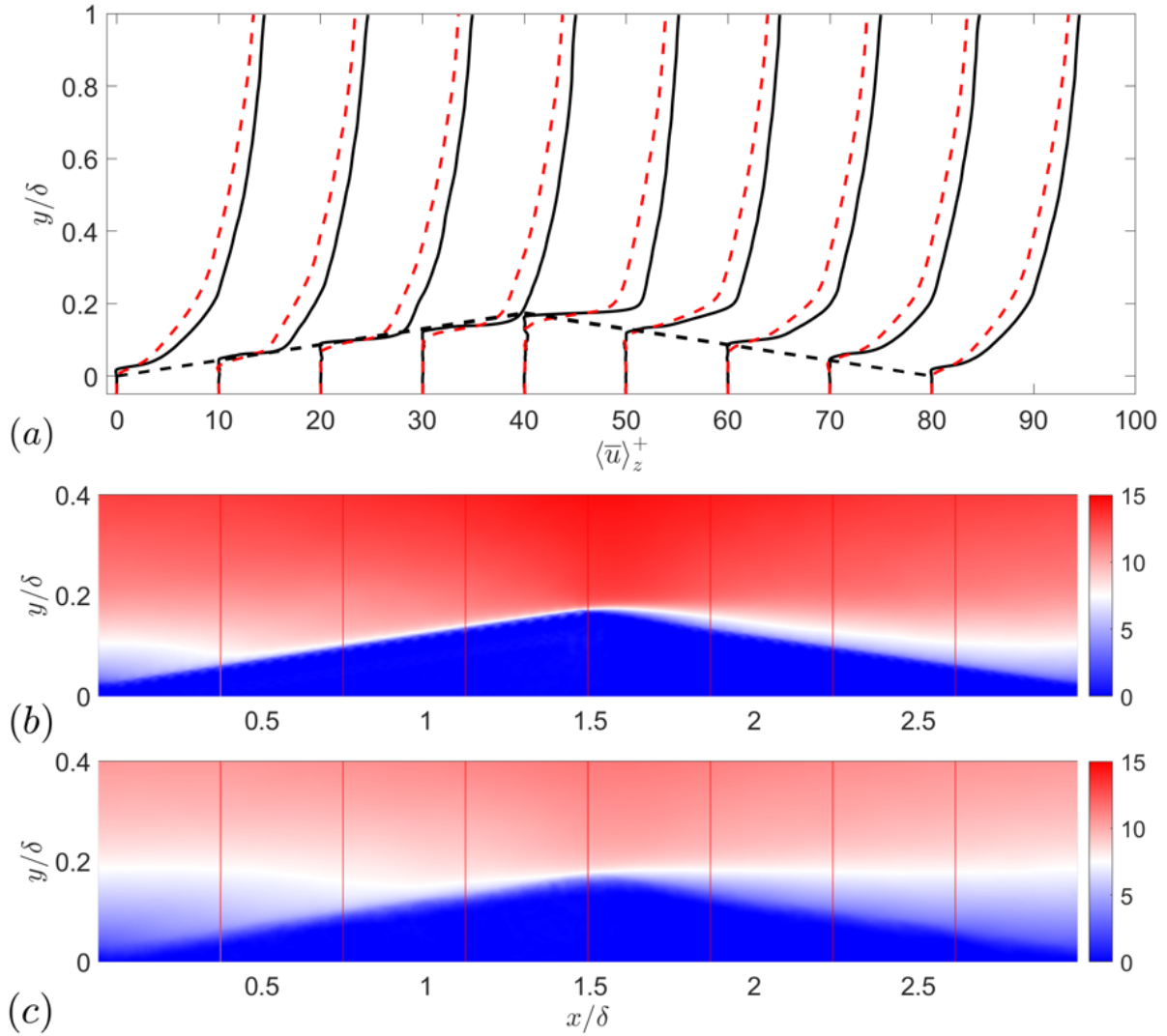


Figure 4.4: (a) Time- and spanwise-averaged streamwise velocity $\langle \bar{u} \rangle_z^+$ for cases with regular (—) and random (---, red) roughnesses. $\langle \bar{u} \rangle_z^+$ contours for (b) regular and (c) random roughness.

4.3 Results

In this section, Cases 1 and 2 are compared to understand the effects of roughness on the hyporheic exchange with the presence of bedform, specifically the effects on turbulent flow and pressure distributions along the SWI and how they influence the mass transport in the sediment.

4.3.1 Effects of roughness geometry on velocity

The y profiles of the time- and spanwise-averaged streamwise velocity normalized by average u_τ are compared in Fig. 4.4 (a). These profiles are qualitatively similar with previous observations of Chen et al. (2015) and Kirca et al. (2020), which show that the flow is accelerated towards the bedform crest, due to the streamline convergence, and decelerated after the crest. The random roughness leads to a lower bulk velocity compared to the regular one and, consequently, results in a 17% higher friction coefficient,

$$C_f = 2 \left(\frac{u_\tau}{U_\delta} \right)^2, \quad (4.1)$$

of 0.0109 compared to 0.0093 in the regular-roughness case. Here, U_δ is the DA velocity at half channel height. The higher C_f is due to the larger effective length scale of the random roughness enhancing the local wall friction on the bedform surface, consistent with the observations made on a macroscopically flat bed for the same roughnesses in Chapter 2.

Profiles of the viscous shear stress normalized by local wall units are shown in Fig. 4.5(a). Despite the adverse-pressure-gradient (APG) region on the lee side and a sharp edge of the bedform at its crest, no mean flow separation (or change of sign of the y -gradient of streamwise mean velocity) is observed. More interestingly, the inflection point of the mean velocity profile stays at the permeable wall, as opposed to the presence of an inflection point inside an APG boundary layer bounded by an impermeable wall (as shown by the similarity solution of the Falkner-Skan equation or by extensive experimental and numerical evidences in turbulence boundary layers). This indicates that a permeable wall promotes inner-outer interaction in a turbulent boundary layer and, consequently, reduces the likelihood of APG-induced flow separation.

The Reynolds shear stress profiles (Fig. 4.5(b)) show deeper penetration of turbulence into the bed in the random case, which indicates stronger wall-normal mean momentum transfer at the interface. Different from the viscous shear stress reaching the maximum values on the bed surface, the maximum magnitudes of the Reynolds shear stress are reached above the wall, farther from the wall in the APG region, consistent with observations made for impermeable-wall APG flows. In addition, the streamwise maximum of the Reynolds shear stress occurs on the lee side, not

corresponding to the x location of the maximum of the y -gradient of the streamwise mean velocity. This indicates that the turbulence are not generated by the mean shear alone; other mechanisms, such as the shear production due to mean strain rate at the roughness scale (i.e. wake production (Raupach and Shaw, 1982; Yuan and Piomelli, 2014c; Yuan and Jouybari, 2018; Mangavelli et al., 2021)), may be important.

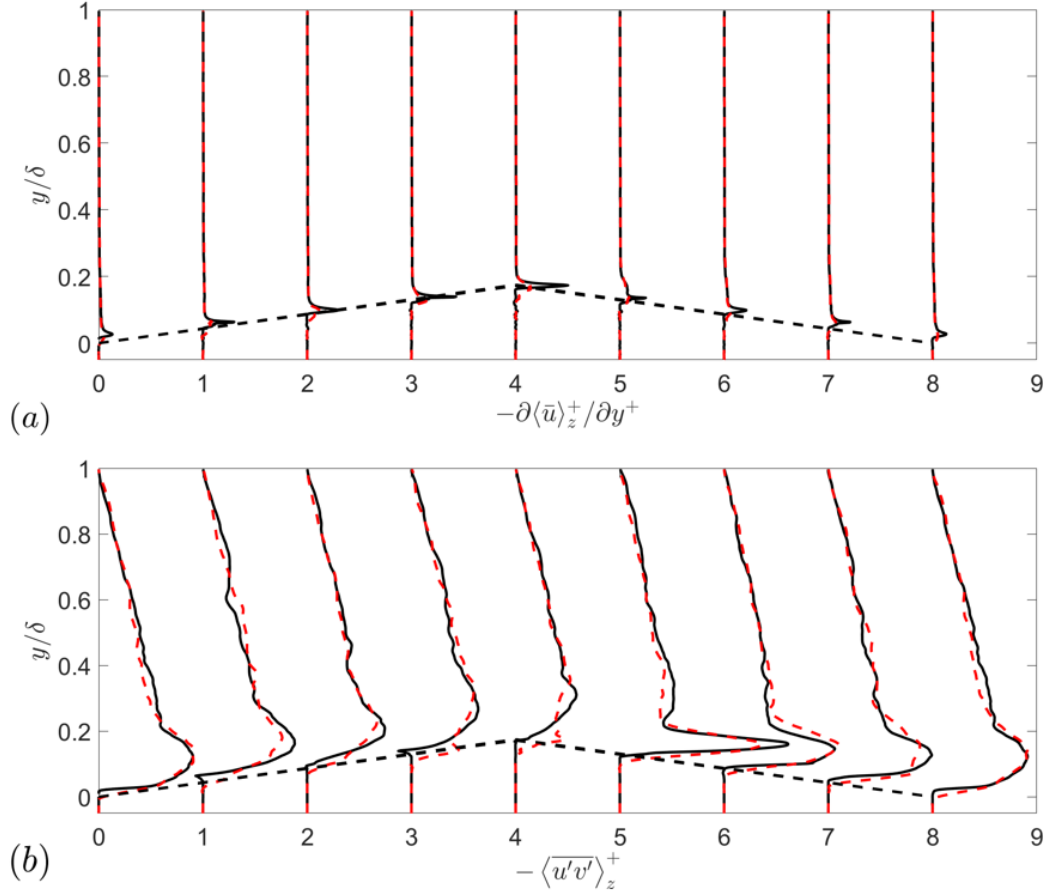


Figure 4.5: Profiles of (a) viscous shear stresses $-\partial\langle\bar{u}\rangle_z^+/\partial y^+$ and (b) Reynolds shear stresses $-\langle\bar{u}'v'\rangle_z^+$ for cases with regular (—) and random (---, red) roughnesses.

4.3.2 Effects of roughness geometry on pressure field

The distribution of the time- and spanwise-averaged pressure across the half channel and the permeable bed is compared in Fig. 4.6 (a,b). In both cases the bedform introduces favorable streamwise pressure gradients on the stoss side and adverse gradients on the lee side. Similar to

what was observed by Cardenas and Wilson (2007) using RANS simulation of surface flows, the minimum pressure is located at the crest of bedform. The pressure distribution along the SWI drives the flow in the sediment and controls the surface-subsurface dynamics exchange and mass transport.

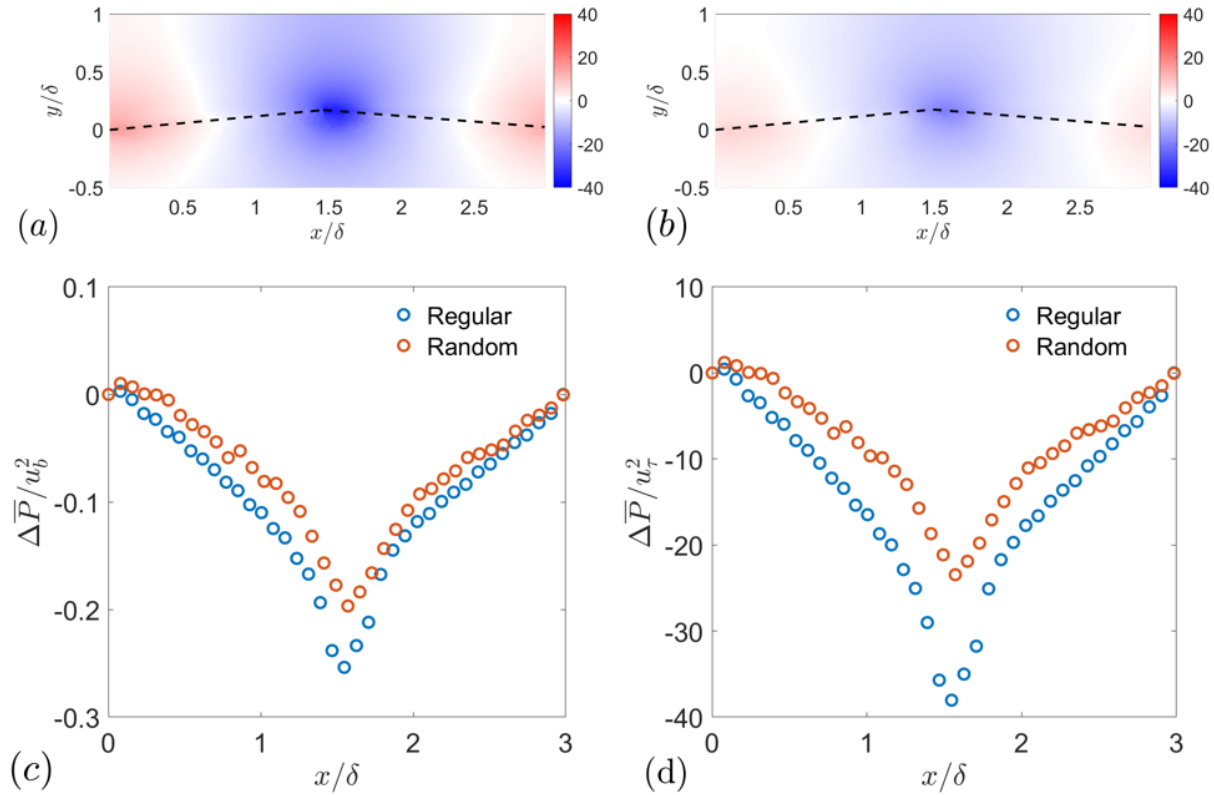


Figure 4.6: Time- and spanwise-averaged pressure field for cases with (a) regular and (b) random roughnesses. Pressure distributions along the SWI normalized using bulk velocity (c) or friction velocity (d) for both cases.

The interfacial pressure non-dimensionalized using either u_b or average u_τ is shown in Fig. 4.6 (c) and (d). When normalized using u_τ (Fig. 4.6 (d)) the pressure variation induced by the random roughness is significantly weaker (by almost a half in magnitude) than that generated by the regular one. However, the profiles almost collapse when the pressure is non-dimensionalized using u_b instead (Fig. 4.6 (c)). This implies that the difference of pressure variations at the SWI between the two cases is mostly due to the higher C_f in the random case. The interfacial pressure variation reflects the pressure drag induced by the dune, which is a quadratic function of the speed of flow

passing it. As the random roughness provides stronger flow resistance than the regular one, it reduces the speed of flow passing the dune and thus reduces the pressure variation. Although the size of roughness is much smaller compared to the size of bedform, it significantly influences the pressure distribution along the interface.

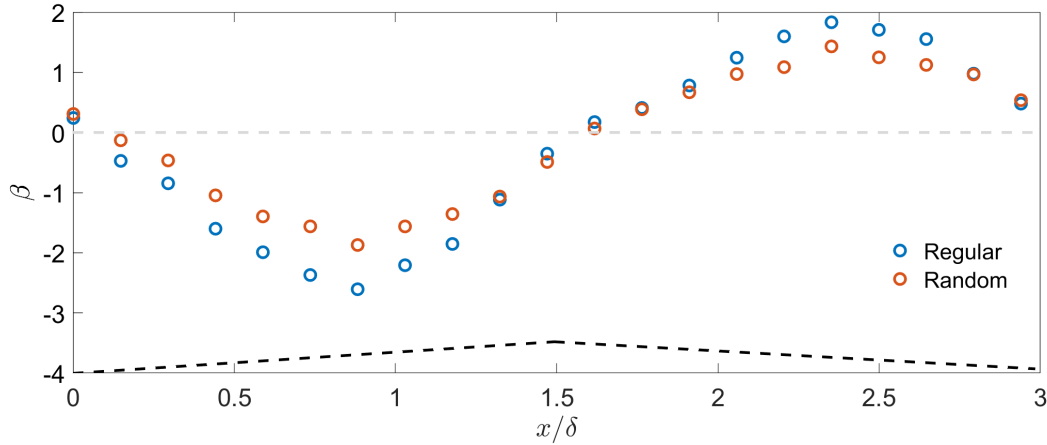


Figure 4.7: Distribution of the Clauser parameter β in the two cases. The black dash line shows the bedform interface geometry.

The strength of pressure gradient can be quantified by the Clauser parameter (Clauser, 1956), $\beta(x) = (\delta^*/\tau_w) (dP_\infty/dx)$, where dP_∞/dx is the streamwise pressure gradient at the free-surface (or half channel height), δ^* is the displacement thickness, and τ_w is the wall shear stress. Here, τ_w is set to the maximum value of local total shear stress $\tau = \nu \frac{\partial \langle \tilde{u} \rangle_z}{\partial y} - \langle \tilde{u}' \tilde{v}' \rangle_z - \langle \tilde{u} \tilde{v} \rangle_z$. The distributions of β in both cases are shown in Figure 4.7, which shows a sinusoidal variation with negative values (i.e. favorable pressure gradients (FPG) and flow acceleration) on the stoss side and positive ones (i.e. APG and flow deceleration) on the lee side. The regular roughness case yields larger β magnitudes with both signs than does the random case, consistent with the discussions above. The β values on the lee side indicates that the turbulence is subjected to mild APGs (Aubertine and Eaton, 2005). A different bedform shape that induces stronger APG is needed to test the effect of wall permeability on flow separation.

Compared to that on a flat bed, the effect of roughness geometry on the pressure distribution on a bedform is significantly different. On a flat bed, the roughness protuberance creates local stagnation

	Interface	τ_{50}	τ_{95}	Slope
Case 1	Regular	3.00	385	-1.52
Case 2	Random	0.0854	7.47	-1.54

Table 4.2: Various characteristics of transit times calculated based on mean advection only. Transit times are normalized by δ/u_τ . Note. τ_{50} and τ_{95} represent 50th (median) and 95th percentiles of the TTD distributions.

point upstream of the protuberance and low pressure region downstream, inducing roughness-scale pressure heterogeneity at the interface. As shown earlier in Figure 2.24, the more intense pressure variations are observed at the random interface of flat bed due to larger roughness scales. However, with the presence of bedform, the higher wall friction due to the random roughness reduces the bulk velocity and the macroscopic pressure variation on the bedform. Meanwhile, the macroscopic pressure variation induced by bedform masks the roughness-scale pressure variation induced by the roughness. In other words, the effect of roughness on the pressure field appears global when a bedform is present, while, on a flat bed, the roughness effect is local.

4.3.3 Effects of roughness geometry on transit times

The effect of bed roughness on modulating the interfacial pressure has significant implications in the exchange of mass (e.g. water and solutes) across the interface, which can be quantified, for examples, using transit time distribution. Table 4.2 compares characteristics of transit times calculated based on mean advection only. Particles are released at the bedform interface and tracked until they exit from the interface, as shown in Figure 4.3. Here, τ_{50} represents the central tendency of the distribution, while τ_{95} is considered as a characteristic τ associated with the rare, long-transit-time subsurface paths. The comparison shows that the τ_{50} and τ_{95} of the transit time distribution in the regular case are significantly higher than in the random case. However, a constant slope of the power-law tail of around -1.5 is observed for both cases. This is similar with the observations of Sawyer and Cardenas (2009) that the tails of residence time distributions follow a power law regardless of permeability structure near the SWI. An important conclusion that follows is that the

difference in grain-scale roughness texture on top of a bedform extends deep into the sediment and significantly modifies the transit time distributions.

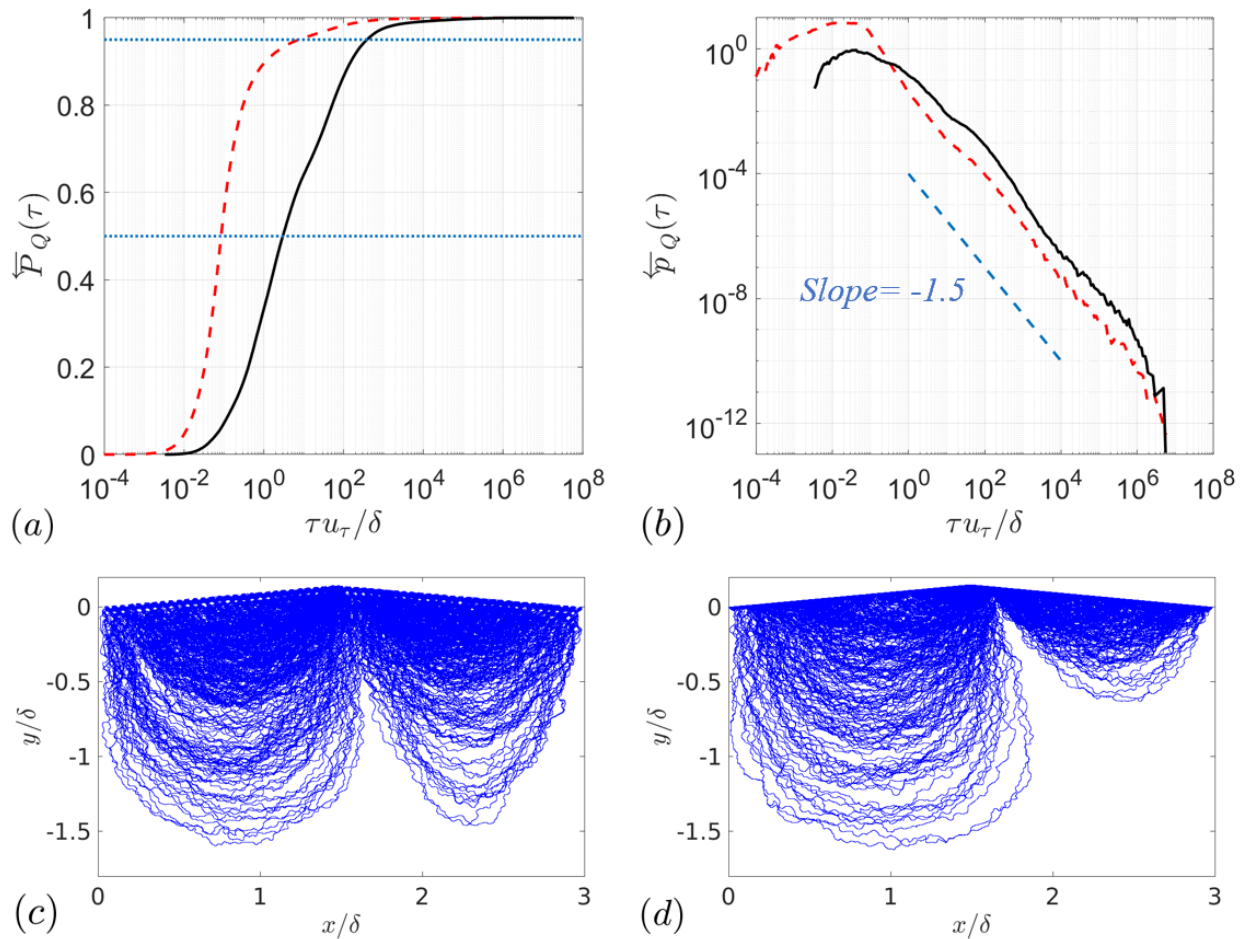


Figure 4.8: Cumulative backward transit time distributions (a) and their pdf distributions (b) for regular (—) and random (---, red) cases. In (a), the horizontal dashed lines (---, blue) mark the 50th (median) and 95th percentiles. In (b), the dashed blue lines (---, blue) show the fitted power law with slopes indicated. Subsurface flow paths in the (c) regular and (d) random cases.

To explain such difference in the TTD characteristics, Figure 4.8(c,d) compares the subsurface paths obtained using the particle tracking approach. For both cases, multiscale subsurface flow paths are induced, with the longest ones characterized by roughly a half of the bedform length scale λ . The general pattern is consistent with observations in existing numerical and experimental studies of subsurface flows induced by bedforms based on advective pumping (Cardenas and Wilson, 2007; Elliott and Brooks, 1997b). Here, the regular roughness is shown to induce a larger fraction of

deep-reaching paths and, consequently, overall longer transit times. This is probably due to the higher-magnitude interfacial pressure variation observed in Fig. 4.6 for this case. Figure 4.9 shows the histogram of the number of pathlines that reaches a depth of each given y value. The area of the integral equals one. It is evident that a larger fraction of pathlines in the regular case reaches deep in the bed than in the random case.

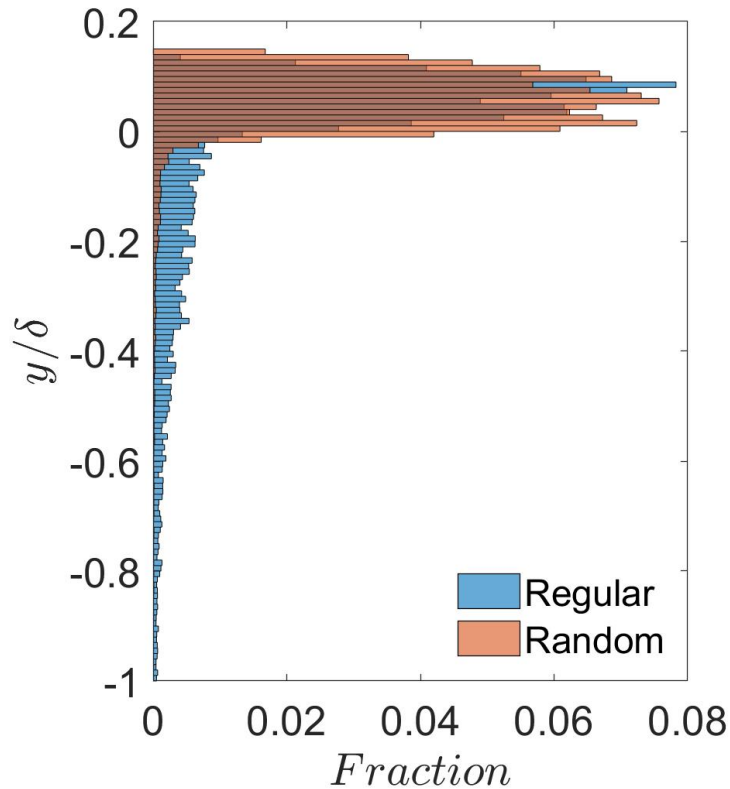


Figure 4.9: Histogram of the number of flow paths reaching a depth of a given y value for the two cases. Values are normalized such that the area integral is one.

The comparison with TTD results calculated for flat beds (Table 3.2) shows that the roughness influences the mass exchange differently depending on whether a bedform is present. On a flat bed, the random roughness induces slightly larger τ_{50} measured at the interface than the regular roughness. However, with the presence of bedform, the regular roughness case induces a much longer transit times. This is due to the different roles played by roughness. The pressure difference here is much larger than on a flat bed. The results show that grain-scale roughness on top of a

bedform modulates the pumping effects of bedform in a way that significantly modifies the transit times.

4.4 Conclusions

Pore resolved DNSs are carried out over immobile bedforms at $Re_K = 2.5$ and $Re_\tau = 1580$ in order to investigate the effects of two roughnesses, regular and random, on the flow and transit times with the presence of bedforms. The time-averaged velocity profiles show that the roughness affects the flow velocity near the SWI, resulting in different wall friction depending on the roughness texture (similar to what happens in impermeable-bed flows), viscous shear stress and shear penetration depth.

The two roughness textures also induces different pressure variation along the bedform surface. On the bedform with regular roughness case, a larger pressure variation is observed than in the random roughness case. This is contrary to what has been observed on a flat bed (in Chapter 3) where the random roughness induces more intense pressure variation of the roughness scale. This discrepancy between flat-bed and bedform cases occurs because of the different roles played by roughness. On flat bed, roughness protuberance creates roughness-scale pressure heterogeneity, while on a bedform, the roughness also modulates the pressure variation of the bedform scale.

In addition, contrary to the flat-bed flows where the random roughness augments mass storage in the bed by inducing longer and deeper flow paths and longer transit times, with the presence of bedform the opposite is observed: the random roughness damps the pumping effect of the bedform and reduces storage. The observations show that grain-scale roughness superimposed on a bedform does not simply act as a smaller-scale “bedform” with a lesser effect on pumping. Instead, roughness modulates significantly the bedform-induced pumping exchange, by changing the macroscopic pressure distribution along SWI. This work demonstrates that grain-scale roughness on top of a bedform should not be ignored when studying hyporheic exchange, as shown by its influence on the pressure variation and transit times.

CHAPTER 5

CONCLUSIONS

5.1 Summary

In this dissertation, three-dimensional pore-resolved direct numerical simulation are carried out to elucidate multiscale flow physics regarding mass and momentum transport across water-sediment interfaces. River-bed sediments representative of realistic ones are synthesized based on molecular dynamics simulations. An immersed boundary method is used to impose the boundary conditions of fluid regime in a complex sediment geometry. The methods are validated by comparing with experimental results. A particle tracking method is implemented to calculate the transit time distributions in the sediment, with or without the contribution of molecular diffusion. These numerical methods have been applied to understand the effects of roughness on flows bounded by flat beds and bedforms. The most important findings and their implications are summarized below.

Bed roughness plays a key role in inducing hyporheic exchange on both flat beds and bedforms. On a flat bed, small bed morphological features on hyporheic exchange should not be ignored, as they significantly affect the dynamics of turbulence, time-mean flow, subsurface pathlines and transit time distributions. Specifically, the larger roughness length scales brought by the random interface results in more intense mixing, pressure variations, more isotropic form-induced stress tensor, significantly higher wall-normal hyporheic flux across SWI and deeper-reaching hyporheic flow paths. These differences explain the dependence of transit times on the roughness geometry. The results also demonstrate that the grain roughness on a flat bed induces hyporheic exchange predominantly through the pumping mechanism, similar to the effect of a bedform.

With the presence of bedform, grain roughness still plays an important role in modifying the wall friction, interfacial pressure distribution and velocity profiles, as well as penetration depth. The large-scale variation of the interfacial pressure is induced by the bedform geometry, while the magnitude of its variation is significantly modulated by the texture of roughness superimposed on

the bedform. Roughness still leads to local pumping of interfacial flow; but a more significant part of its effect is the augmentation of hydrodynamic drag, which slows down the core flow and consequently reduces the pressure variation on the bedform. As a result, the transit times are more sensitive to the roughness texture when a bedform is present than when it is not. These results demonstrate that the effect of bed roughnesses interacts nonlinearly with that of larger bed scales such as bedforms.

5.2 Future work

Pore-resolved simulations such as the DNS herein offer an unprecedented amount of information useful in direct characterization of pore-scale drivers of the flow. In future work, other contributing factors of hyporheic exchange can be further studied with the present methodologies. These factors include Reynolds numbers, bulk permeability, spatial heterogeneity of bed permeability, grain-diameter distributions, bedform configurations such as asymmetric dunes or those with high slope, and moving or deformable beds. DNS data of surface-subsurface exchange within this parameter space are needed to fully understand the hyporheic exchange and validate pore-unresolved models of the exchange. In addition, direct simulations of reactions and microbial biomass grow/decay may be used to understand pore-scale physics in an array of increasingly important topics, such as transport of nutrients/pollutants and greenhouse-gas production in river beds.

APPENDICES

APPENDIX A

DETAILS OF POROUS-BED SYNTHESIS

Both the porous beds with random and regular interface are generated by simulating the pouring of hard spheres of the same diameter, D , into the MD simulation domain. The particles are subject to the gravitational force in the y direction and the forces between particles determined by the Hookean-style granular potential with history effects. The top and bottom boundaries are fixed, where the repulsive boundary condition is imposed; the periodic boundary condition is imposed on the x and z boundaries.

For the bed with the random interface packing, the particles are released at each time step from the top boundary and move towards the bottom boundary due to imposed gravity (Figure A.1). The simulation ends as the sediment-bed domain is filled with randomly packed spheres. For the bed with the regular interface, special treatment is required at the bottom boundary. Specifically, a layer of regularly packed spheres are initially positioned on the bottom boundary (Figure A.2a); a second

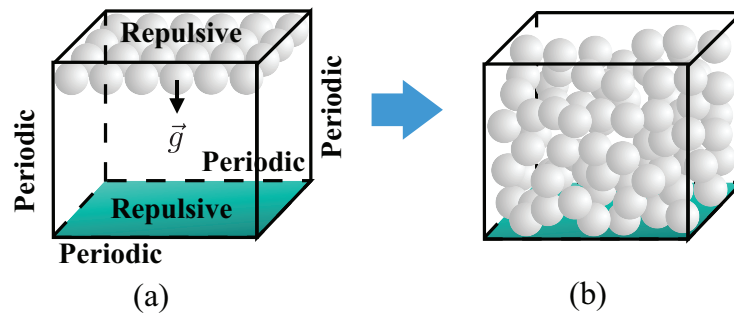


Figure A.1: Bed synthesis with random interface packing.

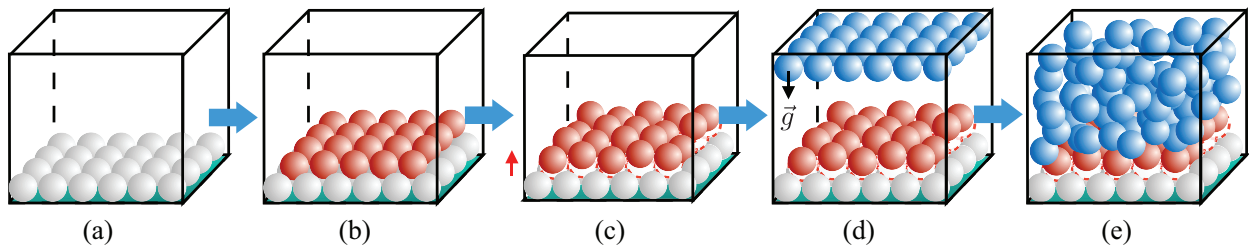


Figure A.2: Bed synthesis with regular interface packing.

layer of spheres are also manually positioned following hexagonal close packing (Figure A.2b). However, as is, the first two layers of spheres lead to locally low value of θ at such elevation. To maintain the running average of $\theta(y)$ (with an averaging window size of D) as almost a constant value of θ_{avg} , the second layer of spheres are shifted away from the wall by a small amount determined by the targeted θ_{avg} value (of an order of $o(0.1D)$ with 3% fluctuations added, Figure A.2(c)). Then, the similar procedure as in Figure A.1 is employed to fill the rest of the porous bed with randomly packed spheres. In the end, the MD simulation domain is flipped upside-down to yield a regularly-packed uppermost layer. Once the particle positions are determined using the aforementioned procedure, the particles are overlaid with the DNS grid and the volume of fluid for each grid cell is determined for the immersed boundary method of the fluid solver.

APPENDIX B

SUPPORT INFORMATION FOR CHAPTER 3

Calculation of the residence time distribution

Integrating the master equation (Equation (3.2)) for a steady system with the boundary condition of zero age for water parcels entering via inflow, i.e.,

$$p_S(0) = \frac{J}{S}, \quad (\text{B.1})$$

and noting that S and $J = Q$ are constants for a steady flow, one obtains

$$\int_0^\tau dp_S(\tau) = -\frac{Q}{S} \int_0^\tau \overleftarrow{p}_Q(\tau) d\tau. \quad (\text{B.2})$$

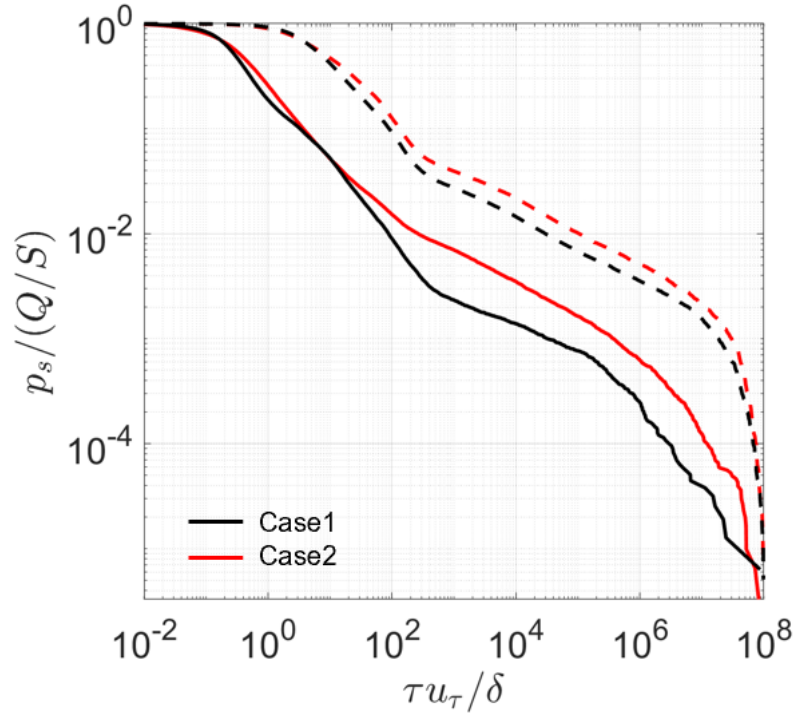


Figure B.1: Residence time distributions (RTD) normalized by Q/S for $y_1 = y_2 = 0$ (—) and $-3D$ (---). For $\tau u_\tau / \delta > o(10^6)$ when $y_1 = y_2 = 0$ or $o(10^7)$ when $y_1 = y_2 = -3D$, the RTD rapidly decreases; this is not physical but an artifact associated with the finite domain size in x (limited to $2L_x$) imposed for particle tracking as the tracking procedure cannot be indefinitely long.

Since $d\overleftarrow{P}_Q = \overleftarrow{p}_Q d\tau$ and $\overleftarrow{P}_Q(0) = 0$ (as the minimal age is 0), this yields

$$p_S(\tau) = \frac{Q}{S} \left[1 - \overleftarrow{P}_Q(\tau) \right]. \quad (\text{B.3})$$

Equation (B.3) states that the total volume of water storage with age τ , which equal to the sum of the volume of stored water that is aging to $\tau + d\tau$ and the volume of water leaving the bed at age τ , is the same as the total water volume leaving the bed at age τ or higher (i.e., $Q(1 - \overleftarrow{P}_Q)$). This is a result of the time-invariant water age distribution in a steady system. The calculated p_S distributions for the regular and random cases, with $y_1 = y_2 = 0$ or $-3D$, are shown in Figure B.1.

Validation of particle tracking method

To verify the implementation of the particle tracking method, the subsurface flow induced by a 2D sinusoidal pressure field applied at the interface is considered, which corresponds to the stationary bedform case studied in EB97. Note that we do not discuss the results of the residence time function from the DNS data. This quantity is used for validation purpose in this section only. An analytical solution of the Darcy velocity was derived by EB97 as

$$u^* = -\cos x^* e^{y^*}, \quad \text{and} \quad v^* = -\sin x^* e^{y^*}, \quad (\text{B.4})$$

where λ is the wavelength of the imposed interface pressure distribution and $*$ denotes normalization using the maximum velocity amplitude at the interface and $\lambda/(2\pi)$. Following EB97, consider a pulse of solute entering the bed at a location \vec{x} . Assume that the flow is steady. Denote the fraction of solute molecules that remains in the bed after an elapsed time τ as $R(\vec{x}, \tau)$. $R(\vec{x}, \tau) = 1$ before the pulse of solute leaves the bed and $R(\vec{x}, \tau) = 0$ after it leaves the bed. The overall residence time function averaged across the bed surface, $\overline{R}(\tau)$, is obtained by averaging R at all surface locations, weighted by the local bed-normal fluid volumetric flux at the bed surface, $q(\vec{x})$,

$$\overline{R}(\tau) = \frac{\int_{(x,z)} q(x, z) R(x, z, \tau) dx dz}{\int_{(x,z)} q(x, z) dx dz}, \quad (\text{B.5})$$

where $\int_{(x,z)} dx dz$ denotes integration throughout the fluid area at the bed surface. According to EB97, the analytical solution of \overline{R} , given in implicit form, is

$$\tau^* = \frac{2 \cos^{-1} \overline{R}}{\overline{R}}. \quad (\text{B.6})$$

Equation (B.4) is used as the advection velocity for particle tracking. The x^* domain size covers two wavelengths, $x^* \in [-\pi/2, 3\pi/2]$, while the y^* domain size is varied from $[-\lambda/2, 0]$ to $[-2\lambda, 0]$ to study the convergence of the particle tracking method. Uniform grids in x and y are used to discretize the velocity fields in Equation (B.4). The spatial resolution is also varied, from 10 points to 50 points per wavelength. The particle-tracked \bar{R} is compared with the analytical solution provided by Equation (B.6) in Figure B.2.

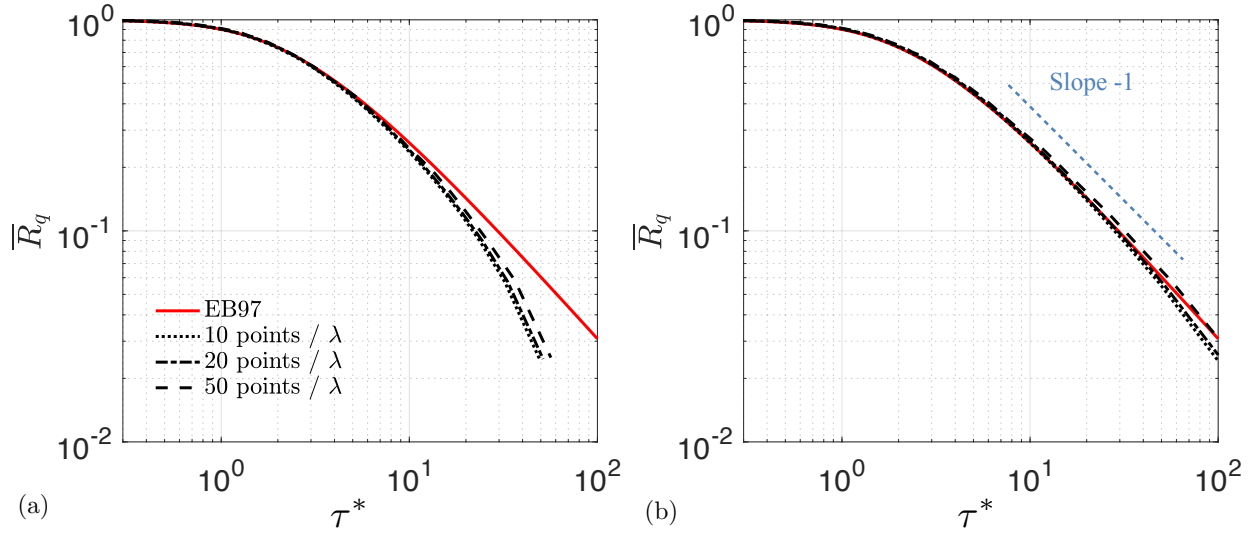


Figure B.2: Validation of particle tracking against EB97, with various spatial resolution and a sediment domain of $y \in [-\lambda/2, 0]$ (a) or $y \in [-\lambda, 0]$ (b).

For sufficiently deep sediment (with depth of at least one bedform wavelength) and sufficiently fine spatial resolution (at least around 50 grid points per wavelength), the particle-tracked residence time distribution matches well with the analytical solution. Figure B.2(a) shows that the values of \bar{R} at large times are significantly underestimated with a small sediment depth due to the absence of deeper flow paths, while Figure B.2(b) shows that the large-time slope is slightly different at a coarse resolution.

Some details of the particle tracking implementation

The following provides explanation as to why a better statistical convergence is obtained for the mean residence times calculated with $y_1 < y_2$ than those calculated with $y_1 > y_2$, with the same $|y_1 - y_2|$. To calculate μ_1 at each (y_1, y_2) combination, the same number of particles are released

in the fluid domain of the bed-parallel plane at y_1 . As illustrated in Figure B.5, among the particles that are released at a y_1 higher than y_2 and eventually leaving the sediment (e.g., released at y'_1 , exiting at y'_2), only a fraction of them reach a depth of y''_2 , leading to fewer averaging samples and more undulatory μ_1 contour lines in Figure 5. On the other hand, for particles released at a y_1 lower than y_2 (e.g., released at y''_1 , exiting at y'_2), all of them pass y'_2 to exit the sediment.

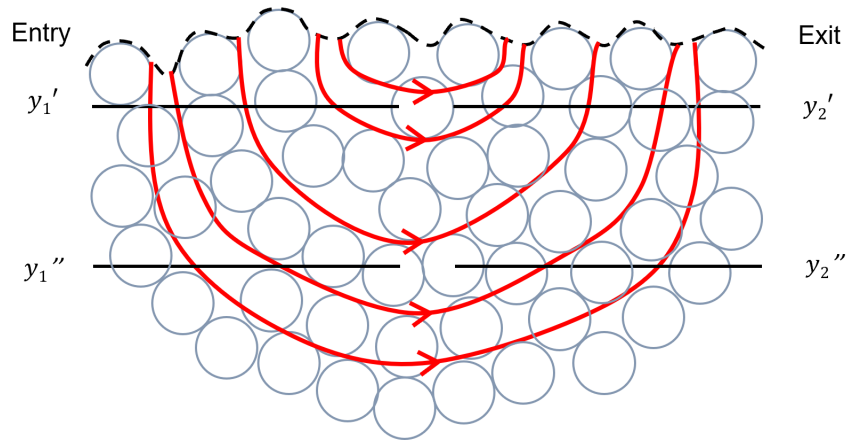


Figure B.3: Sketch to demonstrate that a particle entry elevation (y_1) lower than the exit elevation (y_2) tracks a larger fraction of subsurface flow paths than in the case with $y_1 > y_2$, considering the same $|y_1 - y_2|$. Here, (y'_1, y''_2) tracks 2 out of the 4 paths (50%) entering from y'_1 , while (y''_1, y'_2) tracks 2 out of the 2 paths (100%) entering from y''_1 .

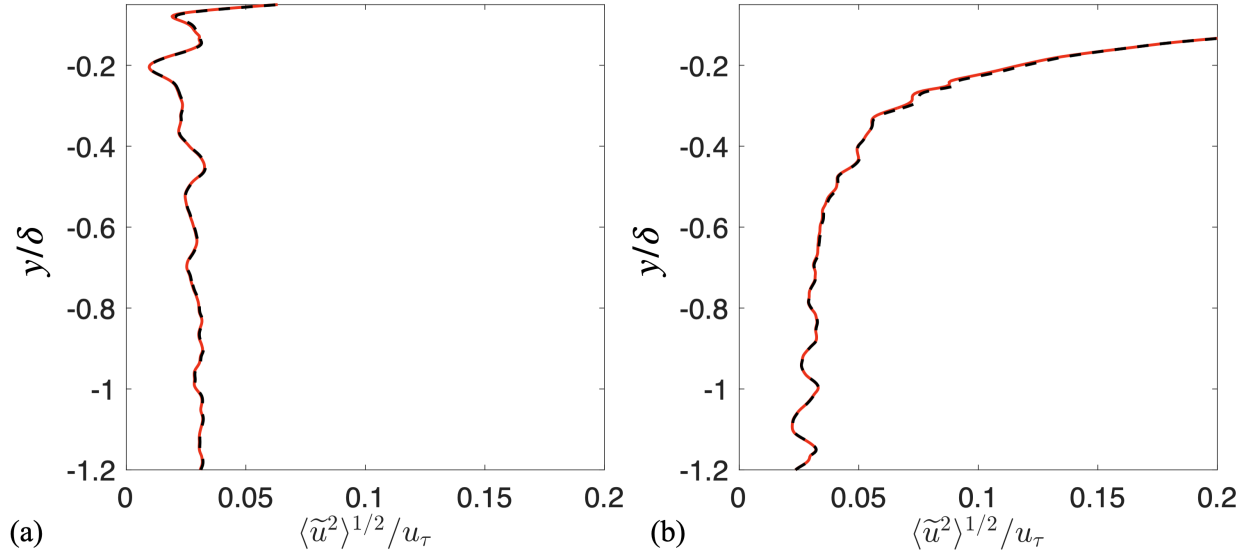


Figure B.4: Streamwise dispersive velocity intensities in the sediment bed: comparison between results obtained from DNS data taken for simulation times of 10 (—, red) and 20 (---) large-eddy turn-over times, for the regular- (a) and random-interface (b) cases.

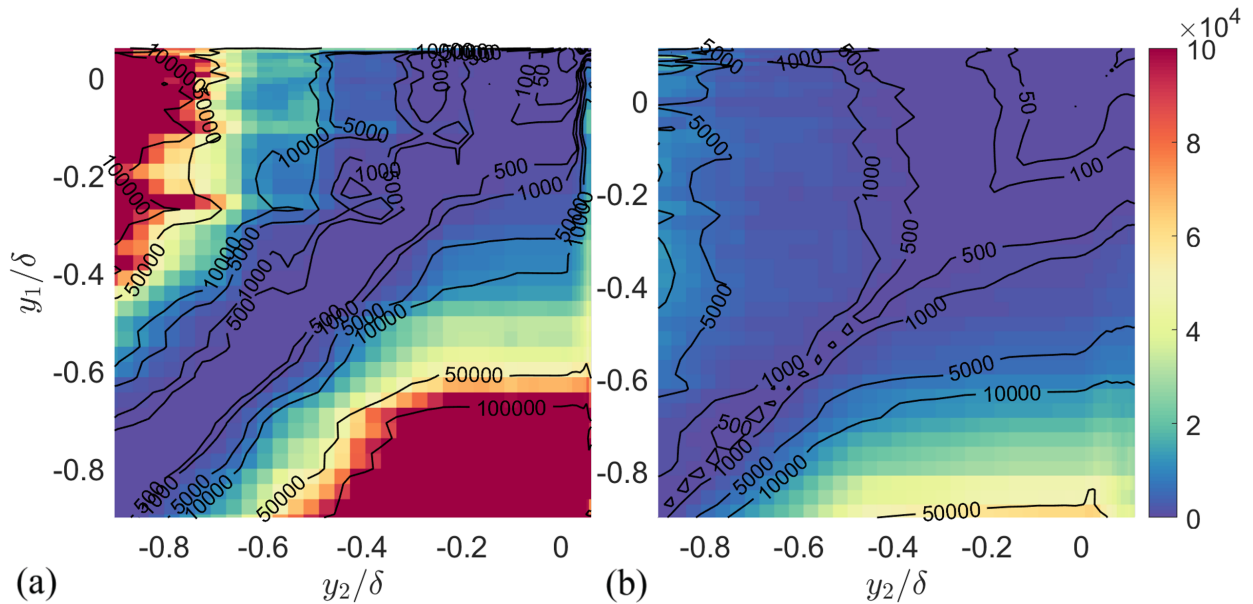


Figure B.5: Transit time of the 95th percentile (τ_{95}) normalized by δ/u_τ with independent variations of y_1 (entry) and y_2 (exit) elevations, for the regular- (a) and random-interface (b) cases.

BIBLIOGRAPHY

BIBLIOGRAPHY

- Amadio, G. (2014). *Particle packings and microstructure modeling of energetic materials*. University of Illinois at Urbana-Champaign.
- Aubeneau, A. F., Martin, R. L., Bolster, D., Schumer, R., Jerolmack, D., and Packman, A. (2015). Fractal patterns in riverbed morphology produce fractal scaling of water storage times. *Geophysical Research Letters*, 42(13):5309–5315.
- Aubertine, C. D. and Eaton, J. K. (2005). Turbulence development in a non-equilibrium turbulent boundary layer with mild adverse pressure gradient. *Journal of Fluid Mechanics*, 532:345–364.
- Baranov, V., Lewandowski, J., and Krause, S. (2016). Bioturbation enhances the aerobic respiration of lake sediments in warming lakes. *Biology Letters*, 12:20160448.
- Battin, T. J., Kaplan, L. A., Findlay, S., Hopkinson, C. S., Marti, E., Packman, A. I., Newbold, J. D., and Sabater, F. (2008). Biophysical controls on organic carbon fluxes in fluvial networks. *Nature Geoscience*, 1:95–100.
- Bencala, K. E. (2000). Hyporheic zone hydrological processes. *Hydrological Processes*, 14(15):2797–2798.
- Benettin, P., Kirchner, J. W., Rinaldo, A., and Botter, G. (2015). Modeling chloride transport using travel time distributions at Plynlimon, Wales. *Water Resources Research*, 51(5):3259–3276.
- Benettin, P., Rinaldo, A., and Botter, G. (2013). Kinematics of age mixing in advection-dispersion models. *Water Resources Research*, 49(12):8539–8551.
- Boano, F., Harvey, J. W., Marion, A., Packman, A. I., Revelli, R., Ridolfi, L., and Wörman, A. (2014). Hyporheic flow and transport processes: Mechanisms, models, and biogeochemical implications. *Reviews of Geophysics*, 52(4):603–679.
- Bottacin-Busolin, A. and Marion, A. (2010). Combined role of advective pumping and mechanical dispersion on time scales of bed form–induced hyporheic exchange. *Water resources research*, 46(8).
- Botter, G., Bertuzzo, E., and Rinaldo, A. (2011). Catchment residence and travel time distributions: The master equation. *Geophysical Research Letters*, 38(11).
- Breugem, W. and Boersma, B. (2005). Direct numerical simulations of turbulent flow over a permeable wall using a direct and a continuum approach. *Physics of fluids*, 17(2):025103.
- Breugem, W., Boersma, B., and Uittenbogaard, R. (2006). The influence of wall permeability on

- turbulent channel flow. *Journal of Fluid Mechanics*, 562:35–72.
- Brinkman, H. (1949). A calculation of the viscous force exerted by a flowing fluid on a dense swarm of particles. *Flow, Turbulence and Combustion*, 1(1):27.
- C. Carman, P. (1937). Fluid flow through granular beds. *Chemical Engineering Research & Design - CHEM ENG RES DES*, 75.
- Cardenas, M. B. (2015). Hyporheic zone hydrologic science: A historical account of its emergence and a prospectus. *Water Resources Research*, 51(5):3601–3616.
- Cardenas, M. B. and Wilson, J. L. (2007). Dunes, turbulent eddies, and interfacial exchange with permeable sediments. *Water Resources Research*, 43(8).
- Cardenas, M. B., Wilson, J. L., and Haggerty, R. (2008). Residence time of bedform-driven hyporheic exchange. *Advances in Water Resources*, 31(10):1382–1386.
- Chandler, I., Guymier, I., Pearson, J., and Van Egmond, R. (2016). Vertical variation of mixing within porous sediment beds below turbulent flows. *Water resources research*, 52(5):3493–3509.
- Chen, X., Cardenas, M. B., and Chen, L. (2015). Three-dimensional versus two-dimensional bed form-induced hyporheic exchange. *Water Resources Research*, 51(4):2923–2936.
- Christensen, K. T. and Wu, Y. (2005). Characteristics of vortex organization in the outer layer of wall turbulence. In *TSFP DIGITAL LIBRARY ONLINE*. Begel House Inc.
- Clauser, F. H. (1956). The turbulent boundary layer. In *Advances in applied mechanics*, volume 4, pages 1–51. Elsevier.
- Cossu, C. and Hwang, Y. (2017). Self-sustaining processes at all scales in wall-bounded turbulent shear flows. *Philosophical Transactions of the Royal Society A: Mathematical, Physical and Engineering Sciences*, 375(2089):20160088.
- Dairain, A., Maire, O., Meynard, G., Richard, A., Rodolfo-Damiano, T., and Orvain, F. (2020). Sediment stability: can we disentangle the effect of bioturbating species on sediment erodibility from their impact on sediment roughness? *Marine Environmental Research*, 162:105147.
- Danesh-Yazdi, M., Foufoula-Georgiou, E., Karwan, D. L., and Botter, G. (2016). Inferring changes in water cycle dynamics of intensively managed landscapes via the theory of time-variant travel time distributions. *Water Resources Research*, 52(10):7593–7614.
- Dey, S. and Das, R. (2012). Gravel-bed hydrodynamics: double-averaging approach. *Journal of Hydraulic Engineering*, 138(8):707–725.
- Dutta, R., Nicolle, J., Giroux, A., and Piomelli, U. (2016). Evaluation of turbulence models

- on roughened turbine blades. In *IOP Conference Series: Earth and Environmental Science*, volume 49, page 062007. IOP Publishing.
- Edwards, D., Shapiro, M., Bar-Yoseph, P., and Shapira, M. (1990). The influence of reynolds number upon the apparent permeability of spatially periodic arrays of cylinders. *Physics of Fluids A: Fluid Dynamics*, 2(1):45–55.
- Elliott, A. (1991). *Transfer of solutes into and out of streambeds*. PhD thesis, California Institute of Technology.
- Elliott, A. and Brooks, N. (1997a). Transfer of nonsorbing solutes to a streambed with bed forms: Laboratory experiments. *Water Resources Research*, 33(1):137–151.
- Elliott, A. and Brooks, N. (1997b). Transfer of nonsorbing solutes to a streambed with bed forms: Theory. *Water Resources Research*, 33(1):123–136.
- Fang, H., Han, X., He, G., and Dey, S. (2018). Influence of permeable beds on hydraulically macro-rough flow. *Journal of Fluid Mechanics*, 847:552–590.
- Flack, K. A. and Schultz, M. P. (2014). Roughness effects on wall-bounded turbulent flows. *Phys. Fluids*, 26:101305.
- Ghodke, C. D. and Apte, S. V. (2016). Dns study of particle-bed–turbulence interactions in an oscillatory wall-bounded flow. *Journal of Fluid Mechanics*, 792:232–251.
- Goharzadeh, A., Khalili, A., and Jørgensen, B. B. (2005). Transition layer thickness at a fluid-porous interface. *Physics of Fluids*, 17(5):057102.
- Grant, S. B., Gomez-Velez, J. D., Ghisalberti, M., Guymer, I., Boano, F., Roche, K., and Harvey, J. (2020a). A one-dimensional model for turbulent mixing in the benthic biolayer of stream and coastal sediments. *Water Resources Research*, 56(12):e2019WR026822.
- Grant, S. B., Monofy, A., Boano, F., Gomez-Velez, J. D., Guymer, I., Harvey, J., and Ghisalberti, M. (2020b). Unifying advective and diffusive descriptions of bedform pumping in the benthic biolayer of streams. *Water Resources Research*, 56(11):e2020WR027967.
- Han, X., Fang, H., He, G., and Reible, D. (2018). Effects of roughness and permeability on solute transfer at the sediment water interface. *Water research*, 129:39–50.
- Harman, C. J. (2015). Time-variable transit time distributions and transport: Theory and application to storage-dependent transport of chloride in a watershed. *Water Resources Research*, 51(1):1–30.
- Harvey, J. W., Böhlke, J. K., Voytek, M. A., Scott, D., and Tobias, C. R. (2013). Hyporheic zone denitrification: Controls on effective reaction depth and contribution to whole-stream mass balance. *Water Resources Research*, 49(10):6298–6316.

- Hassanizadeh, S. M. and Gray, W. G. (1987). High velocity flow in porous media. *Transport in porous media*, 2(6):521–531.
- He, G., Han, X., Fang, H., Reible, D., and Huang, L. (2019). Effects of roughness Reynolds number on scalar transfer mechanisms at the sediment-water interface. *Water Resources Research*, 55(8):6811–6824.
- Huang, H., Ayoub, J. A., et al. (2006). Applicability of the Forchheimer equation for non-Darcy flow in porous media. In *SPE Annual Technical Conference and Exhibition*. Society of Petroleum Engineers.
- Javadpour, F. et al. (2009). Nanopores and apparent permeability of gas flow in mudrocks (shales and siltstone). *Journal of Canadian Petroleum Technology*, 48(08):16–21.
- Jiménez, J. (2004). Turbulent flows over rough walls. *Annu. Rev. Fluid Mech.*, 36:173–196.
- Kalbus, E., Schmidt, C., Molson, J., Reinstorf, F., and Schirmer, M. (2009). Influence of aquifer and streambed heterogeneity on the distribution of groundwater discharge. *Hydrology and Earth System Sciences*, 13(1):69–77.
- Keating, A., Piomelli, U., Bremhorst, K., and Nesic, S. (2004). Large-eddy simulation of heat transfer downstream of a backward-facing step. *Journal of Turbulence*, 5(20):1–3.
- Khirevich, S. (2011). High-performance computing of flow, diffusion, and hydrodynamic dispersion in random sphere packings.
- Kim, J. S. and Kang, P. K. (2020). Anomalous transport through free-flow-porous media interface: Pore-scale simulation and predictive modeling. *Advances in Water Resources*, 135:103467.
- Kim, T., Blois, G., Best, J., and Christensen, K. T. (2017). Experimental study of turbulent structure over permeable walls with a refractive-index-matching technique. In *TSFP DIGITAL LIBRARY ONLINE*. Begel House Inc.
- Kim, T., Blois, G., Best, J. L., and Christensen, K. T. (2018). Experimental study of turbulent flow over and within cubically packed walls of spheres: Effects of topography, permeability and wall thickness. *International Journal of Heat and Fluid Flow*, 73:16–29.
- Kim, T., Blois, G., Best, J. L., and Christensen, K. T. (2020). Experimental evidence of amplitude modulation in permeable-wall turbulence. *Journal of Fluid Mechanics*, 887.
- Kinzelbach, W. (1988). The random walk method in pollutant transport simulation. In *Groundwater flow and quality modelling*, pages 227–245. Springer.
- Kirca, V. S. O., Saghebian, S. M., Roushangar, K., and Yagci, O. (2020). Influence of surface roughness of dune bedforms on flow and turbulence characteristics. *International Journal of*

Sediment Research, 35(6):666–678.

- Knapp, J. L. A., Gonzalez-Pinzon, R., Drummond, J. D., Larsen, L. G., Cirpka, O. A., and Harvey, J. W. (2017). Tracer-based characterization of hyporheic exchange and benthic biolayers in streams. *Water Resour. Res.*, 53:1575–1594.
- Kong, F. and Schetz, J. (1982). Turbulent boundary layer over porous surfaces with different surface geometries. In *20th Aerospace Sciences Meeting*, page 30.
- Kozeny, J. (1927). On capillary movement of water in soil. *German, Sitzber Akad. Wiss. Wien*, 136.
- Krogstad, P.-Å. and Antonia, R. (1994). Structure of turbulent boundary layers on smooth and rough walls. *Journal of Fluid Mechanics*, 277:1–21.
- Krogstad, P.-Å. and Efros, V. (2012). About turbulence statistics in the outer part of a boundary layer developing over two-dimensional surface roughness. *Physics of Fluids*, 24(7):075112.
- Kuwata, Y. and Suga, K. (2016a). Lattice boltzmann direct numerical simulation of interface turbulence over porous and rough walls. *International Journal of Heat and Fluid Flow*, 61:145–157.
- Kuwata, Y. and Suga, K. (2016b). Transport mechanism of interface turbulence over porous and rough walls. *Flow, Turbulence and Combustion*, 97(4):1071–1093.
- Laube, G., Schmidt, C., and Fleckenstein, J. H. (2018). The systematic effect of streambed conductivity heterogeneity on hyporheic flux and residence time. *Advances in Water Resources*, 122:60 – 69.
- Lee, A., Aubeneau, A. F., and Cardenas, M. B. (2020). The sensitivity of hyporheic exchange to fractal properties of riverbeds. *Water Resources Research*.
- Liu, X. and Katz, J. (2018). Pressure rate of strain, pressure diffusion, and velocity pressure gradient tensor measurements in a cavity flow. *AIAA Journal*, 56(10):3897–3914.
- Malard, F., Tockner, K., Dole Oliver, M. J., and Ward, J. (2002). A landscape perspective of surface–subsurface hydrological exchanges in river corridors. *Freshwater Biology*, 47(4):621–640.
- Manes, C., Poggi, D., and Ridolfi, L. (2011). Turbulent boundary layers over permeable walls: scaling and near-wall structure. *Journal of Fluid Mechanics*, 687:141–170.
- Manes, C., Pokrajac, D., McEwan, I., and Nikora, V. (2009). Turbulence structure of open channel flows over permeable and impermeable beds: A comparative study. *Physics of Fluids*, 21(12):125109.

- Mangavelli, S. C., Yuan, J., and Brereton, G. J. (2021). Effects of surface roughness topography in transient channel flows. *J. Turbul.*, 22:434–460.
- Mignot, E., Barthélemy, E., and Hurther, D. (2009). Double-averaging analysis and local flow characterization of near-bed turbulence in gravel-bed channel flows. *Journal of Fluid Mechanics*, 618:279–303.
- Mittal, R., Dong, H., Bozkurttas, M., Najjar, F., Vargas, A., and Von Loebbecke, A. (2008). A versatile sharp interface immersed boundary method for incompressible flows with complex boundaries. *Journal of computational physics*, 227(10):4825–4852.
- Nikora, V., Goring, D., McEwan, I., and Griffiths, G. (2001). Spatially averaged open-channel flow over rough bed. *Journal of Hydraulic Engineering*, 127(2):123–133.
- Nikora, V. I., Goring, D. G., and Biggs, B. J. (1998). On gravel-bed roughness characterization. *Water Resources Research*, 34(3):517–527.
- Packman, A. I., Brooks, N. H., and Morgan, J. J. (2000). A physicochemical model for colloid exchange between a stream and a sand streambed with bed forms. *Water Resources Research*, 36(8):2351–2361.
- Packman, A. I., Salehin, M., and Zaramella, M. (2004). Hyporheic exchange with gravel beds: basic hydrodynamic interactions and bedform-induced advective flows. *Journal of Hydraulic Engineering*, 130(7):647–656.
- Padhi, E., Penna, N., Dey, S., and Gaudio, R. (2018a). Hydrodynamics of water-worked and screeded gravel beds: A comparative study. *Physics of Fluids*, 30(8):085105.
- Padhi, E., Penna, N., Dey, S., and Gaudio, R. (2018b). Spatially averaged dissipation rate in flows over water-worked and screeded gravel beds. *Physics of Fluids*, 30(12):125106.
- Persson, N. J., Albohr, O., Tartaglino, U., Volokitin, A. I., and Tosatti, E. (2005). On the nature of surface roughness with application to contact mechanics, sealing, rubber friction and adhesion. *J. Phys.: Condens. Matter*, 17:R1–R62.
- Plimpton, S. (1995). Fast parallel algorithms for short-range molecular dynamics. *Journal of computational physics*, 117(1):1–19.
- Pokrajac, D. and Manes, C. (2009). Velocity measurements of a free-surface turbulent flow penetrating a porous medium composed of uniform-size spheres. *Transport in porous media*, 78(3):367.
- Raupach, M., Antonia, R., and Rajagopalan, S. (1991). Rough-wall turbulent boundary layers. *Applied mechanics reviews*, 44(1):1–25.

- Raupach, M. R. and Shaw, R. (1982). Averaging procedures for flow within vegetation canopies. *Boundary-layer meteorology*, 22(1):79–90.
- Roche, K., Blois, G., Best, J., Christensen, K., Aubeneau, A., and Packman, A. (2018). Turbulence links momentum and solute exchange in coarse-grained streambeds. *Water Resources Research*.
- Salehin, M., Packman, A. I., and Paradis, M. (2004). Hyporheic exchange with heterogeneous streambeds: Laboratory experiments and modeling. *Water Resources Research*, 40(11).
- Savant, A. S., Reible, D. O., and Thibodeaux, L. (1987). Convective transport within stable river sediments. *Water Resour. Res.*, 23:1763–1768.
- Sawyer, A. H. and Cardenas, M. B. (2009). Hyporheic flow and residence time distributions in heterogeneous cross-bedded sediment. *Water Resources Research*, 45(8).
- Scotti, A. (2006). Direct numerical simulation of turbulent channel flows with boundary roughened with virtual sandpaper. *Physics of Fluids*, 18(3):031701.
- Shen, G., Yuan, J., and Phanikumar, M. S. (2020). Direct numerical simulations of turbulence and hyporheic mixing near sediment–water interfaces. *Journal of Fluid Mechanics*, 892:A20.
- Song, X., Chen, X., Zachara, J. M., Gomez-Velez, J. D., Shuai, P., Ren, H., and Hammond, G. E. (2020). River dynamics control transit time distributions and biogeochemical reactions in a dam-regulated river corridor. *Water Resources Research*, 56(9):e2019WR026470.
- Stoesser, T., Frohlich, J., and Rodi, W. (2007). Turbulent open-channel flow over a permeable bed. In *Proceedings of the Congress-International Association for Hydraulic Research*, volume 32, page 189.
- Stonedahl, S. H., Harvey, J. W., Wörman, A., Salehin, M., and Packman, A. I. (2010). A multiscale model for integrating hyporheic exchange from ripples to meanders. *Water Resources Research*, 46(12).
- Stubbs, A., Stoesser, T., and Bockelmann-Evans, B. (2018). Developing an approximation of a natural, rough gravel riverbed both physically and numerically. *Geosciences*, 8(12):449.
- Suga, K., Matsumura, Y., Ashitaka, Y., Tominaga, S., and Kaneda, M. (2010). Effects of wall permeability on turbulence. *International Journal of Heat and Fluid Flow*, 31(6):974–984.
- Suga, K., Mori, M., and Kaneda, M. (2011). Vortex structure of turbulence over permeable walls. *International Journal of Heat and Fluid Flow*, 32(3):586–595.
- Sun, Y., Park, C.-H., Pichot, G., and Taron, J. (2015). Random walk particle tracking. In *Thermo-Hydro-Mechanical-Chemical Processes in Fractured Porous Media: Modelling and Benchmarking*, pages 153–184. Springer.

- Taneda, S. (1956). Experimental investigation of the wake behind a sphere at low reynolds numbers. *Journal of the Physical Society of Japan*, 11(10):1104–1108.
- Vanoni, V. A. (2006). Sedimentation engineering. American Society of Civil Engineers.
- Venditti, J. (2013). 9.10 *Bedforms in Sand-Bedded Rivers*, pages 137–162.
- Voermans, J., Ghisalberti, M., and Ivey, G. (2017). The variation of flow and turbulence across the sediment–water interface. *Journal of Fluid Mechanics*, 824:413–437.
- Voermans, J. J., Ghisalberti, M., and Ivey, G. N. (2018). A model for mass transport across the sediment-water interface. *Water Resources Research*, 54(4):2799–2812.
- Volino, R. J., Schultz, M. P., and Flack, K. A. (2011). Turbulence structure in boundary layers over periodic two-and three-dimensional roughness. *Journal of Fluid Mechanics*, 676:172–190.
- Whitaker, S. (1996). The forchheimer equation: a theoretical development. *Transport in Porous media*, 25(1):27–61.
- Wondzell, S. M. (2006). Effect of morphology and discharge on hyporheic exchange flows in two small streams in the Cascade Mountains of Oregon, USA. *Hydrological Processes: An International Journal*, 20(2):267–287.
- Wörman, A., Packman, A. I., Johansson, H., and Jonsson, K. (2002). Effect of flow-induced exchange in hyporheic zones on longitudinal transport of solutes in streams and rivers. *Water Resources Research*, 38(1):2–1.
- Wörman, A., Packman, A. I., Marklund, L., Harvey, J. W., and Stone, S. H. (2006). Exact three-dimensional spectral solution to surface-groundwater interactions with arbitrary surface topography. *Geophysical research letters*, 33(7).
- Yuan, J. and Jouybari, M. A. (2018). Topographical effects of roughness on turbulence statistics in roughness sublayer. *Physical Review Fluids*, 3(11):114603.
- Yuan, J., Nicolle, J., Piomelli, U., and Giroux, A. (2014). Modelling roughness and acceleration effects with application to the flow in a hydraulic turbine. In *IOP Conference Series: Earth and Environmental Science*, volume 22, page 022016. IOP Publishing.
- Yuan, J. and Piomelli, U. (2014a). Estimation and prediction of the roughness function on realistic surfaces. *Journal of Turbulence*, 15(6):350–365.
- Yuan, J. and Piomelli, U. (2014b). Numerical simulations of sink-flow boundary layers over rough surfaces. *Physics of Fluids*, 26(1):015113.
- Yuan, J. and Piomelli, U. (2014c). Roughness effects on the reynolds stress budgets in near-wall

turbulence. *Journal of Fluid Mechanics*, 760.

Yuan, J. and Piomelli, U. (2015). Numerical simulation of a spatially developing accelerating boundary layer over roughness. *Journal of Fluid Mechanics*, 780:192–214.

Zagni, A. F. and Smith, K. V. (1976). Channel flow over permeable beds of graded spheres. *Journal of the hydraulics division*, 102(2):207–222.

Zippe, H. J. and Graf, W. H. (1983). Turbulent boundary-layer flow over permeable and non-permeable rough surfaces. *Journal of Hydraulic research*, 21(1):51–65.